博士論文

Integration of excitatory and inhibitory synaptic inputs in the *Drosophila* mushroom body

(ショウジョウバエのキノコ体における興奮性・抑制性シナプス入力の統合)

東京大学大学院総合文化研究科
広域科学専攻生命環境科学系

稲田　健吾

To Satsuki and Yoshiteru Kawabe, Hatsue and Yoshinori Inada.

There are many highly respected motives which may lead men to prosecute research, but three which are much more important than the rest. The first (without which the rest must come to nothing) is intellectual curiosity, desire to know the truth.

Godfrey H. Hardy

Abstract

How cell-type-specific physiological properties shape neuronal functions in a circuit remains poorly understood. I addressed this issue in the *Drosophila* mushroom body, a higher olfactory circuit, where neurons belonging to distinct glomeruli in the antennal lobe feed excitation to three types of intrinsic neurons, α/β, α'/β', and γ Kenyon cells (KCs). Two-photon optogenetics and intracellular recording revealed that whereas glomerular inputs add similarly in all KCs, spikes were generated most readily in α'/β' KCs. This cell type was also the most competent in recruiting GABAergic inhibition fed back by anterior paired lateral neuron, which responded to odors either locally within a lobe or globally across all lobes depending on the strength of stimuli. Notably, as predicted from these physiological properties, α'/β' KCs had the highest odor detection speed, sensitivity, and discriminability. This enhanced discrimination required proper GABAergic inhibition. These results link cell-type-specific mechanisms and functions in the mushroom body circuit.

Contents

List of Figures

List of Tables

Attributions

Chapters 1, 2, 4, and 5 contain modified versions of texts, figures, or tables presented in an article:

Inada, K. Tsuchimoto, Y. and Kazama, H.

Origins of cell-type-specific olfactory processing in the *Drosophila* mushroom body circuit.

Neuron, 2017, vol. 95, pp.357-367.

DOI: http://dx.doi.org/10.1016/j.neuron.2017.06.039

Chapter 3 and Appendix contain unpublished or preliminary observations obtained during the Ph. D. program. I collected and analyzed all the data presented in this dissertation. Experiments with archaerhodopsin, ChR2AR, and C1V1$_{\mathrm{T}}$ were performed with the transgenic fly lines newly generated by my colleague, Yoshiko Tsuchimoto. The text was written with the feedback from my advisor, Hokto Kazama.

Abbreviations

ACh, acetylcholine;

AFM, atomic force microscope;

APL neuron, anterior paired lateral neuron;

Arch, archaerhodopsin;

ATP, adenosine triphosphate;

ATR, all-*trans* retinal;

CGP, CGP54626;

ChR1, channelrhodopsin-1;

ChR2, channelrhodopsin-2;

CW laser, continuous wave laser;

DMNPE, 1-(4,5-dimethoxy-2-nitrophenyl)-ethyl;

DPM neuron, dorsal paired medial neuron;

IR, infrared;

KC, Kenyon cell;

LN, local neuron (in the antennal lobe);

NPE, 1-(*ortho*-nitrophenyl)-ethyl;

ORN, olfactory receptor neuron;

PN, projection neuron;

PSF, point spread function;

PTX, picrotoxin;

PVA, polyvinyl alcohol;

TTX, tetrodotoxin;

VChR1, *Volvox carteri* channelrhodopsin-1;

Chapter 1

Introduction

1.1 Significance of brain research

Brain activity determines what we are. Our sensation, behavior, or even self-recognition is a reflection of neural activity in our brain. Therefore, studying how the brain works is, consequently, studying ourselves. A major challenge in neuroscience today is to understand how information is processed in the brain. The brain is a complex system: it consists of more than one hundred billion neurons interconnected with each other forming circuits. Various kinds of processing that take place in these neural circuits are considered to give rise to brain functions. However, our understanding of mechanisms underlying such processing is still limited.

1.2 The *Drosophila* olfactory circuit as a model to study the function and the mechanisms of neural circuit processing

Invertebrates have been used to investigate this issue because they have simpler neural circuits despite expressing rich behaviors. Among invertebrates, I used *Drosophila melanogaster* as a model organism in this study (Figure 1A), because they provide two major advantages. First, the *Drosophila* brain provides even simpler substrates compared with other invertebrates, enabling detailed characterization of circuit connectivity. For example, the number of projection neurons (PNs) in the antennal lobe is ∼150 in *Drosophila* (Jefferis et al., 2001) and ∼830 in locust (Leitch and Laurent, 1996); the number of Kenyon cells (KCs) in the mushroom body is ∼2000 in *Drosophila* (Aso et al., 2009), ∼50,000 in locusts (Leitch and Laurent, 1996) and ∼170,000 in honeybees (Farris et al., 1999). Another advantage is that *Drosophila* provides sophisticated genetic techniques such as the Gal4/UAS binary expression system (Brand and Perrimon, 1993; see Materials and Methods),

which reliably labels and manipulates genetically identified neurons.

The *Drosophila* olfactory circuit involved in memory-guided behavior consists of three distinct structures: the antenna, the antennal lobe, and the mushroom body (Figure 1B). Odors are detected by the olfactory receptor neurons (ORNs) housed in the antennae. ORNs send their axons to a specific structure called glomerulus in the antennal lobe. Local neurons (LNs) in the antennal lobe mediate lateral interaction. PNs in the antennal lobe contact with ORNs in the glomerulus and convey the information to the mushroom body. The mushroom body is a circuit critical for olfactory association (Dubnau et al., 2001; McGuire et al., 2001; Heisenberg, 2003).

1.3 Contribution of each cell type to neural circuit processing

Neural circuits organize diverse types of cells to exert specific functions. Examining how each type of cells behaves in a circuit is therefore central to understanding the basis of neural processing. In the cerebral cortex, comprised of highly heterogeneous cells, neurons have been typically characterized and classified based on their morphological, molecular, and physiological features (Ascoli et al., 2008), an effort that continues at an increasingly comprehensive scale (Markram et al., 2015; Tasic et al., 2016). The major challenge following the characterization of cell-intrinsic properties is twofold. First is to examine synaptic interactions between these cells. Second is to examine how intrinsic and synaptic properties together determine the function of a cell type in the context of specific information processing such as sensory processing.

To address these challenges, here I focused on the *Drosophila* mushroom body circuit. Olfactory information conveyed to the mushroom body is represented by the activity of $\sim$2000 KCs, which can be classified into α/β, α'/β', and γ types from morphological and developmental characteristics (Figure 1C; Aso et al., 2009; Crittenden et al., 1998; Lee et al., 1999). The axons of these three types of KCs form α/β, α'/β', and γ lobes of the mushroom body, respectively. Different types of KCs show spontaneous and odor-evoked spikes with distinct characteristics (Turner et al., 2008). Moreover, genetic manipulations of KCs have suggested that olfactory memory is embedded in multiple lobes and specific sets of them are necessary for retrieving recent and remote memories (Blum et al., 2009; Cervantes-Sandoval et al., 2013; Krashes et al., 2007; Krashes and Waddell,

2008; Trannoy et al., 2011; Xie et al., 2013). Although these functional differences between lobes indicate that the activity of each KC type must arise through cell-type-specific mechanisms, this has not been physiologically investigated.

KCs receive excitatory drive from PNs (Caron et al., 2013; Gruntman and Turner, 2013), each of which belongs to one of $\sim$51 glomeruli in the antennal lobe, the primary olfactory processing center (Figure 1B; Stocker et al., 1990; Tanaka et al., 2012). An individual KC is connected, on average, to seven PNs randomly (Caron et al., 2013) with some biases (Gruntman and Turner, 2013). KCs are also under recurrent inhibitory control of GABAergic anterior paired lateral (APL) neurons (Figure 1D; Lin et al., 2014; Liu and Davis, 2009; Tanaka et al., 2008). A single APL neuron in a hemisphere extends processes throughout the mushroom body. How these excitatory and inhibitory synaptic inputs, as well as cell's intrinsic properties, interact to shape the output of each KC remains elusive.

In this study, I investigated this question by stimulating individual presynaptic neurons with single- and two-photon optogenetics while monitoring postsynaptic activity in KCs with intracellular recording. Our approach revealed that whereas three types of KCs integrate excitatory inputs similarly, they generate spikes and recruit APL neuron-mediated inhibition in a cell-type-specific manner. Furthermore, recording of KC odor responses found previously uncharacterized functions of α'/β' KCs in olfactory processing that were predicted from these cell-type-specific properties: more rapid detection and enhanced discrimination between different odor concentrations.

1.4 Artificial manipulation of neural activity

To study the physiological mechanisms underlying the generation of sensory response in KCs, it is essential to artificially manipulate the activity of presynaptic PNs. In this study, I tested two different techniques: uncaging and optogenetics.

1.4.1 Uncaging

The uncaging technique uses caged compounds, which are biologically active molecules that are made inactive by the addition of light-sensitive "caging" chemicals. In the absence of an optical

stimulation, caging chemicals prevent biological molecules from interacting with their receptor. Optical stimulation (or "uncaging light") evokes photolysis that removes the caging chemicals (or "uncages" the caged compound), exposing an active form of the molecules (Figure 2A). For example, NPE-caged ATP does not have an influence on ATP receptors until the uncaging light is applied. Uncaging-light-evoked photolysis breaks the chemical bond between NPE and ATP, leading to the releasing of uncaged ATP (Figure 2B; Ellis-Davies, 2007). An important advantage of the uncaging method is the wide variety of available compounds, because, in principle, any biological molecules can be used for uncaging experiments as long as the molecule is properly caged. Indeed, a number of caged compounds such as caged glutamate (Fino et al., 2009; Lutz et al., 2008; Matsuzaki et al., 2004; Olson et al., 2013), ATP (Engels and Schlaeger, 1977; Kaplan et al., 1978), EGTA (Brown et al., 1999; Ellis-Davies and Kaplan, 1994), calcium (Momotake et al., 2006), or GABA (Wieboldt et al., 1994) have been developed and made commercially available, enabling both artificial excitation and inhibition of neurons.

1.4.2 Optogenetics

Although uncaging is a powerful method to manipulate neural activity, the method has three major problems. First, although the experimenter can control the illuminated area and duration of uncaging light, it is difficult to control the diffusion of released chemical as it spreads in accordance with the flow in the bath solution. This limits both spatial and temporal resolution of stimulation. Second, uncaging can mimic chemical synaptic transmission, but not electrical transmission. Electrical transmission through gap-junctions relies only on the electrical activity of pre- and postsynaptic neurons without releasing neurotransmitters from presynaptic terminals. Third, uncaging chemicals are generally expensive, making it hard to conduct long-term experiments.

Optogenetics, named after the interdisciplinary contributions of optics, genetics and bioengineering (Deisseroth et al., 2006), employ a different approach to manipulate neural activity. Contrary to the uncaging method, optogenetic probes expressed in the genetically targeted cells utilize optical stimulation to manipulate the neural activity directly. Optogenetic probes are microbial opsins (or type Ⅰ superfamily opsins), which have a seven-transmembrane structure (Kato et al., 2012; Nagel et al., 2003). An opsin protein bound to retinal, a vitamin A-related organic cofactor, is

termed rhodopsin. Upon absorption of a photon, retinal photoisomerizes from all-trans to the 13-cis configuration, a sequence of conformational changes that takes place within the opsin (Hegemann et al., 2005; Nikolic et al., 2009). Several distinct subfamilies of microbial opsins allow ions to flow through plasma membranes (Figures 3A and 3B). Among these opsins, blue-light-sensitive channelrhodopsin-2 (ChR2) was first introduced to the field of neuroscience, because it can depolarize neurons by transporting cations across the membrane under the blue light stimulation (Nagel et al., 2003). The influx could be controlled at millisecond precision, conferring neuroscientists to manipulate the neural activity at high temporal resolution (Boyden et al., 2005). Through a decade of studies, dozens of variants fulfilling various experimental requirements have been developed (Boyden, 2015; Deisseroth, 2015); probes that excite neurons with high temporal precision (Gunaydin et al., 2010; Klapoetke et al., 2014; Lin et al., 2009; performance of variants was compared in Mattis et al., 2012), that transport selective ions (Kleinlogel et al., 2011), or that inhibit neurons (Berndt et al., 2014; Chow et al., 2010; Chuong et al., 2014; Govorunova et al., 2015; Zhang et al., 2007). Recently, optogenetic probes have been combined with two-photon excitation (see below) to increase spatial resolution. Probes are also being optimized for two-photon excitation-mediated activation (Prakash et al., 2012).

As in rodents, optogenetic probes can function in *Drosophila.* In general, fly lines carrying a DNA sequence coding an optogenetic probe downstream of *UAS* (see Materials and Methods) are used to express optogenetic probes ectopically. Both probes that depolarize or hyperpolarize neurons (Figures 3) are available. For example, ChR2 expressed in a PN excites it by evoking an inward current through the plasma membrane (Figures 3A-3C), whereas archaerhodopsin, optogenetic silencer, inhibits the neural activity by evoking an outward current (Figures 3D-3F).

1.5 Calcium imaging

Uncaging and optogenetics enable researchers to manipulate neural activity artificially. Such artificial manipulations are often accompanied with measuring postsynaptic neural activity. One commonly used method to measure neural activity is to detect the light emitted from fluorescent indicators with microscopy. Direct imaging of membrane potential has been achieved with voltage-

sensitive dyes (Peterka et al., 2011). However, because of the relatively low signal-to-noise ratio, accurate imaging of neural activity by voltage-sensitive dyes has not been widely used except for the pioneering studies in rodents (Baker et al., 2005; Briggman et al., 2005) and flies (Cao et al., 2013; Yang et al., 2016).

Calcium imaging is an alternative method to detect neuronal activity. Calcium indicators report the intracellular concentration of calcium ions ($\left[Ca^{2+}\right]$). Depolarization of cellular membranes induced by synaptic currents or spiking activity opens voltage-dependent calcium channels, generating a transient increase of $\left[Ca^{2+}\right]$. Therefore, $\left[Ca^{2+}\right]$ can be used as a proxy for neuronal activity. Many calcium indicators have been developed to date and, among those, genetically encoded green fluorescent protein/calmodulin protein sensor (GCaMP) series are widely used. With GCaMP, it is possible to image the spiking activity as well as the subthreshold activity of neurons (Akerboom et al., 2012; Chen et al., 2013; Nakai et al., 2001; Sun et al., 2013). Dozens of GCaMP variants have been developed aiming to improve the signal-to-noise ratio by increasing fluorescent intensity in response to the calcium influx, while decreasing the baseline fluorescence (performance of variants was compared in Chen et al., 2013). GCaMP consists of three molecules: circularly permutated EGFP (cpEGFP), M13 fragment of myosin light chain kinase (M13), and calmodulin (CaM; Figure 4A; Nakai et al., 2001). M13 is a target sequence of CaM. The N-terminal of cpEGFP is connected to M13, whereas the C-terminal is connected to CaM. Binding of Ca^{2+} to CaM induces a conformational change of GCaMP caused by CaM-M13 interaction, resulting in the increase of fluorescence intensity (Figure 4B).

1.6 Two-photon miscroscopy

1.6.1 Principle

In this study, to stimulate caged compounds and optogenetic probes or to image GCaMP, I used two-photon excitation. Two-photon excitation is a nonlinear process in which one atom or molecule absorbs two photons in the same quantum event to be excited. Two-photon microscopy is a microscopy that visualizes fluorescent molecules with two-photon excitation. Two-photon excitation was first theoretically predicted by Göppert-Mayer in 1931 (Göppert-Mayer, 1931). She noticed that

probability of the process where two photons co-act to excite an atom was not zero, although the absorption of two photons in the same quantum event is rare under ordinary light intensities. Thirty years later, two-photon excitation was experimentally demonstrated (Kaiser and Garrett, 1961). In the study, the CaF_2:Eu^{2+} crystals were illuminated with ruby maser, wavelength of which was 694.3 nm, and obtained expected blue fluorescence. To increase the probability of two-photon excitation, the mode-locked pulsed IR laser was later developed (Curley et al., 1992; Huggett, 1968; Spence et al., 1991). Unlike a conventional continuous wave (CW) laser, power delivered from a pulsed laser is condensed in pulses of certain duration and repetition rate. Pulsation of a laser creates denser concentration of photons, leading to the increase of probability of two-photon excitation.

Two-photon microscope was first introduced to neuroscience in 1990 (Denk et al., 1990). Fluorescent molecules require optical irradiation to match the energy gap between the ground and the excited states to emit fluorescence. Conventional confocal microscopes use a UV or visible CW laser to excite fluorescent molecules (Figure 5A). In contrast, two-photon microscope equips a mode-locked pulsed IR laser to induce two-photon excitation of fluorescent molecules. Because two photons are simultaneously absorbed in the two-photon excitation process, photons with wavelength $({\lambda_1}^{-1} + {\lambda_2}^{-1})^{-1}$, where λ_1 and λ_2 are wavelengths of the irradiated laser, are sufficient to excite fluorescent molecules (Diaspro et al., 2005; Denk et al., 2006). In the typical microscopy, $\lambda_1 = \lambda_2$, so that the energy gap can be filled with two photons carrying half of the energy compared to the photons emitted from a CW laser (Figure 5B).

As described above, two-photon excitation requires dense concentration of photons. In the laser scanning microscope, such a condition only occurs at the focus (Figures 5C and 5D). Mathematically, excitation probability outside the focal region is estimated as z^{-2n}, where z is the distance from the focal plane and n is the number of photons absorbed per quantum event (Denk et al., 2006). Therefore, in principle, out-of-focus excitation is negligible in two-photon microscopy allowing the system to simply detect all the photons emitted from the substance.

Two-photon microscopy is superior to the conventional confocal microscopy from the following reasons. First, because fluorescence at out-of-focus is not excited, two-photon microscopy provides better depth resolution (Figures 5C and 5D). Second, two-photon microscopy does not require a pinhole, which is an essential device for the conventional confocal microscope to exclude the signal

from out-of-focus, enabling higher efficiency of photon detection (Svoboda and Yasuda, 2006). Third, because light with longer wavelength penetrate organic tissues better, it can image from deeper regions of the brain (Svoboda and Yasuda, 2006). Forth, avoidance of out-of-focus excitation leads to less photobleaching of fluorescent molecules (Drobizhev et al., 2011).

1.6.2 Two-photon uncaging, optogenetics, and calcium imaging

Given that uncaging, optogenetics, and calcium imaging utilize light to stimulate targeted neurons and molecules as described above, combining these methods with two-photon microscope was expected to provide additional advantages over those using conventional microscopes. These combinations are often termed two-photon uncaging, two-photon optogenetics and two-photon calcium imaging, respectively. Two-photon optogenetics, for example, was shown to evoke action potentials at higher spatial resolution compared with CW laser stimulation (Andrasfalvy et al., 2010).

Chapter 2

Materials and Methods

2.1 Gal4/UAS expression system

The Gal4/UAS system is a genetic method to express a gene of interest in specific cells at a specific developmental stage (Brand and Perrimon, 1993). Gal4 is a transcription factor from yeast. Gal4 binds to the *UAS* (upstream activation sequence) and induces the transcription of the gene of interest downstream of *UAS* (Figure 6A). This binary expression system offers three important advantages. First, because the expression of *UAS* is controlled by the Gal4 expression, the gene of interest can be expressed in cells specified by Gal4 drivers. Second, one can express genes that do not originate in *Drosophila.* Gal4-driven green fluorescent protein (GFP) expression is a typical example. Third, numerous Gal4 lines expressing Gal4 in various spatiotemporal patterns have been generated and widely shared in the community. Nearly a decade after the introduction of Gal4/UAS system, two additional binary expression systems were engineered: namely lexA/lexAop and Q systems (Lai and Lee, 2006; Potter et al., 2010; Riabinina et al., 2015). Because these binary expression systems can operate independently of each other, different genes can be expressed in different types of neurons in the same brain.

Recently, a site-specific insertion of DNA sequence became possible to create these transgenic lines. The bacteriophage ϕC31 encodes a serine integrase that mediates sequence-directed recombination between a bacterial attachment site (*attB*) and a phage attachment site (*attP*; Figure 6B; Thorpe et al., 2000). In the site-specific insertion technique, ϕC31 integrates *attB*-containing plasmids into *attP* landing sites that have been inserted to the genome in advance (Bischof et al., 2007). To generate a fly line carrying *UAS*, for example, pUASattB plasmid is injected into the flies that possess a construct containing *attP* landing site. ϕC31 recombines *attB* and *attP*, resulting in the formation of *attR* and *attL* sequence between which pUASattB is integrated (Figure 6C). Because

attR and *attL* are refractory to the ϕC31 integrase, the recombination process is irreversible (Bischof et al., 2007).

By using this technique, two groups of laboratories have independently created the next generation transgenic lines (the GMR collection and the VT collection; Jenett et al., 2012; von Philipsborn et al., 2011). These collections have three attractive features. First, these fly lines tag far fewer cells compared to the previously generated lines, enabling us to label or manipulate the neurons of interest with higher specificity. Second, more than 4000 lines are generated in those collections, making the chance of finding the lines that specifically label the neurons of interest high. Third, the confocal brain images showing the expression pattern are freely available for each fly line. The open-access databases provide the research community with a rapid and economical way of screening for fly lines tagging the neurons of interest.

2.2 Fly stocks

Flies were raised on standard cornmeal agar under a 12 hour light/ 12 hour dark cycle at 25 °C, except for the flies expressing optogenetic probes, which were raised on the food containing all-*trans* retinal (Toronto Research Chemicals) and kept in dark prior to the experiments. Electrophysiological or imaging experiments were performed on adult females, 3 days or 7-10 days post eclosion, respectively. The following stocks were used: *VT33006-Gal4* (*attP2*) (von Philipsborn et al., 2011); *VT43924-Gal4* (*attP2*) and *APL-Gal4* (*VT43924-Gal4* $\left[attP2\right]$*, UAS-Gal4*) (Wu et al., 2013); *Mz19-Gal4* (Ito et al., 1998; Tanaka et al., 2004), *OK107-Gal4* (Connolly et al., 1996), *UAS-ReaChR::Citrine* (*attP40*) (Inagaki et al., 2014), *UAS-mCD8::GFP* (*attP40*) (Lee and Luo, 1999), *UAS-myr::GFP* (*attP40*), *UAS-myr::GFP* (*attP2*) (Pfeiffer et al., 2010), *UAS-CsChrimson::mVenus* (*attP40*) (Klapoetke et al., 2014), *UAS-GCaMP5G* (*attP40*) (Akerboom et al., 2012), *UAS-GCaMP6s* (*attP40*) and *UAS-GCaMP6s* (*VK00005*) (Chen et al., 2013), *pebbled-Gal4* (Sweeney et al., 2007), *NP3062-Gal4, UAS-CD8GFP* (Hayashi et al., 2002), *UAS-ChR2-C/CyO; UAS-ChR2-B/TM6b* (Hwang et al., 2007), *UAS-CD8GFP; UAS-P2X$_2$/TM6b* (Lima and Miesenböck, 2005), *UAS-ChIEF*$\left[c10\text{-}2\right]$ (Wang et al., 2011), *UAS-ChETA* (*attP40* or *attP2*) (Petersen and Stowers, 2011), *tubP-Gal80ts* (McGuire et al., 2003).

For this project, the following transgenic fly lines were newly generated: *UAS-ChR2(C128A/H134R)-ts-EYFP* (*attP40* or *attP2*), *UAS-ChR2(C128A/H134R)-p2A-EYFP* (*attP40* or *attP2*), *UAS-C1V1(E162T)-ts-EYFP* (*attP40* or *attP2*), *UAS-C1V1(E162T)-p2A-EYFP* (*attP40* or *attP2*), *UAS-Archaerhodopsin3-GFP* (*attP40* or *attP2*) by cloning plasmids (gifts from Edward Boyden) into pUASTattB and injecting the plasmids to embryos though a service provided by Genetic Services, Inc.

2.3 Caged compounds

The following caged compounds were used: 1-(*ortho*-nitrophenyl)-ethyl (NPE)-caged ATP (NU-301, Jena Bioscience), 1-(4,5-dimethoxy-2-nitrophenyl)-ethyl (DMNPE)-caged ATP (A1049, Invitrogen), RuBi-caged nicotine (3855, Tocris Bioscience), DMNP-caged EDTA (6848, Setareh Biotech). NPE-caged ATP was dissolved in the external saline at 1 mM. DMNPE-caged ATP was dissolved in the external saline containing apyrase (A6535, Sigma) at 13 mM. RuBi-caged nicotine was dissolved in the external saline at 1 mM.

DMNP-caged EDTA, first dissolved in ethanol, was mixed with the external saline (final concentration was 1.3 mM). Neither blue laser nor IR laser stimulation to DMNP-caged EDTA evoked responses in PNs (data not shown). However, I might have failed to assess the PN response to DMNP-caged EDTA accurately, because the final caged-EDTA solution was not transparent (white turbidity), preventing the identification of the antennal lobe position using fluorescent signals.

To test the $P2X_2$ activation, ATP without the cage (A9187, Sigma) was dissolved in the external saline at 1 mM.

2.4 Electrophysiology

Flies were dissected in the external saline containing (in mM) 103 NaCl, 3 KCl, 5 N-Tris(hydroxymethyl) methyl-2-aminoethanesulfonic acid (TES), 8 trehalose dehydrate, 10 glucose, 26 $NaHCO_3$, 1 $NaH_2PO_4H_2O$, 1.5 $CaCl_2{\cdot}2H_2O$, 4 $MgCl_2{\cdot}6H_2O$ (pH $\sim$7.2, osmolarity adjusted to $\sim$275 mOsm). The entire brain was removed from the head capsule and fixed dorsal side up on a glass slide with surgical glue (GLUture, Abbott). The preparation was continuously perfused with the external saline, bubbled with 95% O_2 /5% CO_2 (pH $\sim$7.3). All the experiments were conducted at room temperature

($\sim$25 °C), and particularly for the experiments of two-photon optogenetics, the temperature of the bath was monitored and adjusted to 24-25 °C (TC-324B, Warner Instruments). Electrophysiological recordings were made with a Multiclamp 700B amplifier (Molecular Devices) equipped with a CV-7B headstage. Signals were low-pass filtered at 1 kHz and digitized at 10 kHz. Voltages were uncorrected for the liquid junction potential.

2.4.1 PN recordings

Whole-cell patch-clamp recordings from PN somata were performed as previously described (Kazama and Wilson, 2009). In brief, a patch pipette was pulled from a thin-wall glass capillary (1.5 mm o.d./ 1.12 mm i.d., TW150F-3, World Precision Instruments). Resistance of the pipette was typically 8-10 MΩ. The internal solution contained (in mM) 140 KOH, 140 aspartic acid, 10 HEPES, 1 EGTA, 4 MgATP, 0.5 Na_3GTP, 1 KCl, and 13 biocytin hydrazide (pH $\sim$7.2, osmolarity adjusted to $\sim$265 mOsm). Cells were held at around -60 mV by injecting a hyperpolarizing current. GABA receptor antagonists, picrotoxin (PTX; P1675, Sigma) and CGP54626 (CGP; 1088, Tocris), were dissolved in the external saline at 5 μM and 10 μM, respectively (Wilson and Laurent, 2005). Cell-attached recordings from PN somata were conducted in a voltage-clamp mode using pipettes filled with external saline. The command potential was adjusted so that the amplifier did not pass any current. To achieve a proper cell-attached configuration, I applied low intensity light from a 594 nm CW laser to induce spikes in PNs and adjusted the negative pressure applied inside the pipette until the signal-to-noise ratio of spikes became sufficiently high. Recordings were made from one neuron per brain. After the recording, the brain was gently released from the glass slide and was fixed in 4% paraformaldehyde for $>$ 90 min on ice for immunohistochemistry (see below).

2.4.2 KC recordings

Whole-cell patch-clamp recordings from KC somata were performed with the same procedure as PN recordings with several modifications. A thick-wall glass capillary (1.5 mm o.d./ 0.84 mm i.d., 1B150F-3, World Precision Instruments) was pulled and pressure-polished (Goodman and Lockery, 2000; Johnson et al., 2008) with a microforge (MF-820, Narishige) and a pneumatic picopump (Figures 7A-7D; PV820, World Precision Instruments). The air pressure was adjusted to $\sim$35 psi.

The final pipette resistance was typically 10-12 MΩ. Cells were held at around −60 mV by injecting a hyperpolarizing current unless otherwise mentioned. To assess the quality of KC recordings during experiments, I injected current steps at several separate times, and aborted the recording if the KC did not spike in response to the stimulation. In Figure 17, all the physiological properties were measured shortly after attaining the whole-cell configuration. Tetrodotoxin (TTX; 1078, Tocris) was dissolved in the external saline at 1 μM. To examine whether *Mz19-Gal4*-positive PNs are connected to the recorded KC or not (Figures 18 and 19), KC claws were visualized as previously reported (Gruntman and Turner, 2013). Briefly, Alexa 594 (A10438, Invitrogen) was dissolved in the internal solution at 250 μM and injected into the KC neurites through a patch pipette during recording. After the recording, the brain was immediately fixed in 4% paraformaldehyde at room temperature for a short period of time (10 min) to avoid the attenuation of signals of the dye and the fluorescence of a Citrine protein tagged ReaChR. The mushroom body calyx was imaged from the posterior side of the brain to obtain clear images of claws with a confocal microscope (Leica TCS SP2) equipped with a 63× water-immersion objective lens (numerical aperture $\left[\mathrm{NA}\right]$ 0.90). After taking the images of claws, the brain was immunostained to visualize biocytin as described below.

2.5 Immunohistochemistry

The brain was stained with antibodies as previously reported (Badel et al., 2016). The following chemicals were used for primary antibodies: nc82 (Developmental Studies Hybridoma Bank), anti-GFP (04404-84, Nacalai), and anti-GABA (A2052, Sigma). Biocytin was visualized by conjugating with Streptavidin:CF555 (29038, Biotium). Vectashield (H-1000, Vector laboratories) was used as mounting medium. Images of the brain were acquired either with a Leica TCS SP2 confocal microscope equipped with a 20× (NA 0.50) or 63× (NA 0.90) water-immersion objective lens, or with an Olympus FV1000-D confocal microscope equipped with a 60× (NA 1.2) water-immersion objective lens.

2.6 Iontophoresis

For iontophoresis of ACh, a sharp glass pipette ($\sim$15 MΩ) was filled with 10 mM acetylcholine chloride (A6625, Sigma) dissolved in external saline. ACh was ejected into the mushroom body calyx by a brief (500 ms) positive current pulse using an iontophoresis unit (Model 260, World Precision Instruments).

2.7 Stimulation of optogenetic probes

2.7.1 LED/mercury light stimulation

Wide-field optical stimulation was achieved by high power LEDs (M470L2 and M590L3 for ReaChR and CsChrimson, respectively, Thorlabs) or filtered light from a mercury lamp (for Arch). An LED (M470L2) with peak output at wavelength of $\sim$470 nm was used for both the activation of ReaChR and excitation of Citrine tagged to ReaChR. Because ReaChR is sensitive to a broad spectrum of light (Lin et al., 2013), blue light was sufficient to make the PNs expressing ReaChR fire at $\sim$200 Hz (Figures 8A and 8B). Light from an LED or a mercury lamp was collimated and delivered to an upright microscope (BX51Wl, Olympus) equipped with a 40x water-immersion objective lens (NA 0.80). LED light was pulsated at 80 Hz. Neutral-density filters (U-25ND25 or U-25ND6, Olympus) were used to stimulate the cells at lower intensities. All the reported optical intensity of LED light was measured at the back aperture of the objective lens (S120VC sensor, Thorlabs).

2.7.2 IR stimulation

IR stimulation experiments were performed with a two-photon laser scanning microscope (Leica TCS SP2) equipped with a 20$\times$ water-immersion objective lens. A Ti:Sapphire laser (MaiTai eHP, Spectra-Physics) was mode-locked at 960 nm. The beam size of the IR laser was adjusted to under-fill the back aperture of the objective lens to make the excited volume dictated by the point-spread function slightly larger than convention (Helmchen and Denk, 2005). The intensity was adjusted to 10 mW at the back aperture. The resolution of scanning was 0.17 μm/pixel and the dwell time was 2.4 μs/pixel. Prior to IR stimulation, the position of the antennal lobe was determined by imaging

the signals from Citrine tagged to ReaChR with a continuous wave laser (514 nm). 6×6 ROIs (the size of each ROI is 12 μm $\times$ 12 μm) were set to cover the antennal lobe along x- and y- axes. The entire depth of the antennal lobe was covered by scanning 18 frames each separated by 5 μm along the dorsoventral axis (z-axis). ROIs were stimulated by an IR laser individually in turn. PNs responded maximally at a certain ROI and much weakly at several of orthogonally-located collateral ROIs, forming a "cross" shaped response pattern (Figure 15). Responses outside of this "cross" region were negligible. Stimulation of neither cell bodies nor the medial antennal lobe tract (axons) evoked action potentials in PNs.

To study how PN inputs are integrated in KCs, I isolated two cross-shaped ROIs to be stimulated that fulfilled the following criteria. First, they did not overlap with each other along the x- and y-axes. Second, they were located in the same focal plane and that within three rows of ROIs to be stimulated at short intervals (Figures 9A and 9B). Under this condition, centers of two ROIs were stimulated within 173 ms. The same procedure was applied to examine the integration of input from three ROIs (Figure 9C). Because of experimental constraints, I could not examine the integration of more than four ROIs.

2.8 Calcium imaging

Odor-evoked calcium responses of APL neurons and KCs were recorded *in vivo* with a two-photon laser scanning microscope (LSM 7 MP, Zeiss) equipped with a water-immersion objective lens (W Plan-Apochromat, 20×, NA 1.0) as previously described (Badel et al., 2016) with several modifications. Briefly, individual flies were attached to a custom-made recording plate and a small portion of the head cuticle was removed to expose the mushroom body medial lobes. The external saline added on top of the plate was circulated throughout the experiment. Ethyl butyrate (E15701, Sigma-Aldrich) diluted in mineral oil (23334-85, nacalai tesque) by 5 different factors (10^{-9}, 10^{-7}, 10^{-5}, 10^{-3}, and 10^{-1}) was presented for 1 s at 30 s inter-trial-interval with a custom-made olfactometer (Badel et al., 2016). Ethyl butyrate at each concentration was presented four times (Figures 23 and 25) or ten times (Figure 24) in random order. GCaMP was excited with a Ti:Sapphire pulsed laser (Chameleon Vision II, Coherent) mode-locked at 930 nm. The laser intensity was adjusted to $\sim$16

mW at the back aperture of the objective lens. The scanning resolution was 2.08 μm/pixel and the dwell time was 16.6 μs/pixel (23 ms/frame) for Figures 23 and 25, and 6.52 μs/pixel (9 ms/frame) for Figure 24, respectively. GCaMP signals in β, β', and γ lobes were analyzed at their tips where different lobes are clearly segregated in space (Figures 23 and 24) by setting a 16.64 μm $\times$ 16.64 μm ROI, which roughly covers the tip. Mean GCaMP fluorescence within a ROI was calculated using ImageJ (NIH). The reported change in fluorescence (ΔF/F) in Figures 23 and 25 is an average of three, fixed frames around the peak response.

2.9 Data analysis

All statistical analyses were performed in Matlab or R. Sample sizes were not estimated in advance. Statistical tests, significance, and sample size are reported in the figures and figure legends. All mean values are reported as mean $\pm$ SEM. K-means clustering (Figures 19 and 20) was performed in R. Onset time of a response in Figure 24 was detected by a previously described algorithm (Kudoh and Taguchi, 2002). Dynamic range in Figure 25 was calculated in each condition (with or without GABA receptor antagonists) by subtracting the response to 10^{-9} from that to 10^{-1} dilution, normalized by the response to 10^{-1} dilution. Note that the dynamic range can be larger than 1 when the response to 10^{-9} dilution is slightly negative.

Linear discriminant analysis (Figure 25) was performed in R with MASS package as described previously (Bhandawat et al., 2007). For each fly and each cell type, data consisted of 20 responses (responses to 4 repeated presentations of odors at 5 different concentrations). I withheld one response from the data and trained the decoder with the remaining 19 responses. After training, I asked the decoder to identify the concentration corresponding to the withheld response. Decoding accuracy shown in Figure 25 represents the average across analyses, each time withholding one of the four responses, for each concentration.

Chapter 3

Generating spikes in PNs with two-photon excitation

3.1 Introduction

To examine how KCs process PN inputs, it is essential to individually activate PNs in distinct sets of glomeruli. Because glomeruli in the antennal lobe are densely packed, artificial stimulation has to offer high spatial resolution in order to activate only the target glomeruli without activating others. To achieve this, I tested two-photon uncaging and two-photon optogenetics.

3.2 Two-photon uncaging

I first tested two-photon uncaging. The brain was incubated in the external saline containing a caged compound, while recording from randomly selected PNs (Figure 10A). Because most of the caged compounds I tested have not been applied in *Drosophila*, I illuminated the compound first with a CW laser to check whether the compound is capable of activating PNs, and then applied an IR laser to test two-photon uncaging.

3.2.1 Caged-ATP

Caged-ATP is one of the most widely used caged compounds in neuroscience. ATP activates a family of ionotropic P2X receptors and each P2X receptor displays distinct functional properties (Khakh and North, 2012). Among those receptors, $P2X_2$ receptor, a nonselective cation channel (Zemelman et al., 2003), was shown to activate fly neurons when it was ectopically expressed and stimulated with ATP (Lima and Miesenböck, 2005).

As expected, application of ATP without caging chemical (non-caged ATP) depolarized PNs expressing $P2X_2$ receptor and induced action potentials (Figure 10B). I then tested two caged-ATP compounds: DMNPE-caged ATP and NPE-caged ATP. I ectopically expressed $P2X_2$ receptor in PNs. Application of DMNPE-caged ATP in the bath solution evoked bursting of PN spikes in the absence of optical stimulation, presumably because some unwanted free ATP in the caged-ATP solution activated $P2X_2$ receptors. To remove the free ATP, I incubated DMNPE-caged ATP solution with apyrase prior to the experiment (Lima and Miesenböck, 2005). In addition, I conducted the experiment in dark. However, DMNPE-caged ATP solution still evoked bursting in PNs without uncaging light (Figure 10C).

Unlike DMNPE-caged ATP, NPE-caged ATP did not evoke spontaneous firing. However, neither a CW laser nor an IR laser evoked depolarization (Figure 10D). Although I have tested various protocols with various concentrations of the caged compound or intensities of IR laser, I failed to generate action potentials in PNs with NPE-caged ATP.

3.2.2 Caged-nicotine

I next tested the caged-nicotine. Nicotine is an agonist of nicotinic acetylcholine receptors (nAChRs). Because ORN-to-PN synapses are cholinergic and the transmission can be blocked by a nAChR antagonist (Kazama and Wilson, 2008), uncaged nicotine was expected to activate PNs. I used ruthenium-bipyridine based caged nicotine (RuBi-caged nicotine; Filevich et al., 2010). CW laser stimulation successfully evoked action potentials in PNs, although the trial-to-trial reliability of spike generation was low (Figure 10E). IR laser stimulation of RuBi-caged nicotine, on the other hand, failed to generate spikes (Figure 10E).

3.2.3 Discussion

Although I examined various caged compounds (including DMNP-caged EDTA, data not shown, see Materials and Methods), IR light failed to generate spikes in PNs. NPE-caged ATP did not evoke spikes even to the CW laser stimulation (Figure 10D), implying that the efficiency of photolysis was too low to affect the PN.

Rubi-nicotine, on the other hand, was uncaged by the blue laser, as evident from the action poten-

tials in PNs (Figure 10E). However, it did not affect the cell once the stimulation was switched to IR (Figure 10E). Two mechanisms may be underlying these differential responses. First, the efficiency of photolysis by an IR laser may have been lower than that by a CW laser, leading to the production of fewer amount of uncaged (released) nicotine. Second, because the actual focal volume of two-photon excitation is smaller than that with a CW laser (Figure 5C and 5D; Helmchen and Denk, 2005), less amount of nicotine may have been released.

Even if uncaging evoked spikes in PNs, the resolution was expected to be insufficient because of the major problems discussed in Chapter 1. Therefore, I moved to two-photon optogenetics.

3.3 Two-photon optogenetics

Two-photon-elicited photocurrent was expected to be smaller than that of single-photon-elicited one, because the focal volume is smaller (Helmchen and Denk, 2005; Denk et al., 2006). In rodent or zebrafish studies, spikes were evoked by fast scanning of a cell body with an IR laser (Prakash et al., 2012; Zhu et al., 2009), temporally-focused pulsed laser (Andrasfalvy et al., 2010; Papagiakoumou et al., 2010), or a spiral scan (Rickgauer and Tank, 2009). These studies showed that two-photon optogenetics can evoke action potentials at high spatial resolution (Andrasfalvy et al., 2010).

In previous studies using a laser scanning microscope, spikes were elicited by scanning cell bodies (Prakash et al., 2012; Zhu et al., 2009). In *Drosophila* PNs, however, stimulation of the cell body was unlikely to evoke action potentials reliably, because the cell body is expected to be electronically distant from the spike initiation zone (Gouwens and Wilson, 2009).

Two-photon excitation had not been applied for neurophysiological studies in *Drosophila.* Therefore, first I developed a protocol to evoke action potentials in PNs. The induction of spikes with two-photon optogenetics was challenging, because strong illumination with an IR laser seemed to damage fly neurons (see Appendix).

Optogenetics (with CW light) is now widely used in *Drosophila*, and various UAS reporter lines that carry genes encoding optogenetic probes are available. To express optogenetic probes in the majority of glomeruli, I first used *NP225-Gal4* which labels ∼37 glomeruli out of ∼51 (Tanaka et al., 2012). However, I found that progenies of this Gal4 line crossed with some UAS reporter

lines showed lethality: they died at the larval or pupal stages (see Appendix). The lethality was observed in the progeny of *NP225-Gal4* crossed with *UAS-ChR2-lineB*, *UAS-ChR2-H134R*, or *UAS-ReaChR*. Based on the observation, in the later experiments, I identified *VT33006-Gal4*, which labels $\sim$44 glomeruli while avoiding the lethality. Because generation of action potentials in PNs with two-photon-elicited photocurrents requires high photocurrent, I excluded wild type ChR2, ChR2 with H134R mutation and ChETA from the candidates given that those probes were expected to generate low photocurrent after performing pilot experiments. Instead, I pursued ChIEF (Lin et al., 2009), C1V1$_{\mathrm{T}}$ (Yizhar et al., 2011), ChR2AR (Prakash et al., 2012), and ReaChR (Lin et al., 2013). I expressed the optogenetic probes in the majority of glomeruli and stimulated them with CW light or a pulsed laser, while recording from randomly-selected PNs (Figures 11A, 12A).

3.3.1 ChIEF

First, I tested ChIEF, a chimera of channelrhodopsin-1 (ChR1) and ChR2 with a single mutation (Lin et al., 2009). The photocurrent of ChIEF is larger than that of the wild type ChR2, although the two channels show similar kinetics (Mattis et al., 2012). I expressed *UAS-ChIEF* using *NP225-Gal4* driver. Stimulation with a CW laser evoked spikes in PNs (Figure 11B). However, IR laser stimulation neither evoked spikes nor even significant depolarization (Figure 12B).

3.3.2 C1V1$_{\mathrm{T}}$

Next, I examined C1V1$_{\mathrm{T}}$. C1V1$_{\mathrm{T}}$ is a chimera of ChR1 and *Volvox carteri* ChR1 (VChR1) (Yizhar et al., 2011; Zhang et al., 2008) and was shown to generate robust photocurrents in mammalian neurons under the IR stimulation (Prakash et al., 2012). Transgenic fly lines carrying C1V1$_{\mathrm{T}}$ were newly generated and I drove expression in PNs using *NP225-Gal4*. Unexpectedly, neither blue nor green light stimulation activated PNs (Figure 11C), although fluorescent molecules tagged with C1V1$_{\mathrm{T}}$ (EYFP) was expressed properly (data not shown). This was not because of the selection of a Gal4 driver, because PNs expressing C1V1$_{\mathrm{T}}$ driven by the different Gal4 line, *Mz19-Gal4*, also did not respond to the optical stimulation (Figure 11D). A prior study using C1V1$_{\mathrm{T/T}}$, which has one additional mutation to C1V1$_{\mathrm{T}}$, also failed to induce the expected gustatory behavioral responses (Inagaki et al., 2014). These results suggest that C1V1$_{\mathrm{T}}$ is not functional in *Drosophila* neurons.

3.3.3 ChR2AR

Optogenetic channels with slower closing kinetics may elicit larger two-photon-elicited currents, because a given neuron expressing these probes can sum up the photocurrents evoked by the IR stimulation. Point mutation of cysteine 128 residual to alanine (C128A) or threonine (C128T) turns ChR2 to a bi-stable channelrhodopsin (Berndt et al., 2009), which is opened by blue light ($\sim$470 nm) and stays conductive until the green light ($\sim$520 nm) is applied (Ritter et al., 2013; Stehfest et al., 2010). ChR2AR is ChR2 with double mutations: C128A confers bi-stability and H134R confers enhanced photocurrents. A previous study showed that two-photon-elicited photocurrent of ChR2AR is maximal at 940 nm (Prakash et al., 2012). To express ChR2AR in fly neurons, a transgenic line carrying *UAS-ChR2AR* was newly generated. As predicted, *NP225-Gal4* driven ChR2AR depolarized PNs in response to the blue light and the amount of depolarization was high enough to induce spikes (Figure 11E). Subsequent amber light stimulation (594 nm) decreased the membrane potential to the resting level (Figure 11E). 940 nm IR stimulation evoked spikes, and sequential applications of IR and 594 nm lasers elicited spikes at restricted z-frames (Figure 12C). To check the ratio of glomeruli that can generate action potentials in response to IR stimulation, I expressed ChR2AR using two Gal4 lines, *NP225-Gal4* and *VT33006-Gal4.* I found that 11 out of 19 glomeruli (58%; n = 25 PNs) showed spikes.

Although ChR2AR successfully generated spikes in many glomeruli, I noticed that the IR-evoked firing rate was relatively low: IR stimulation generated 40.0 $\pm$ 15.1 spikes/s (mean $\pm$ standard deviation), whereas CW stimulation evoked 94.3 $\pm$ 29.7 spikes/s in the same glomeruli (n = 7 PNs from 5 glomeruli). Because ChR2AR could only evoke weak responses, I decided not to use it further.

3.3.4 ReaChR

Finally I examined ReaChR. ReaChR was constructed from ChIEF, VChR1 and VChR2 (Lin et al., 2013). ReaChR provides larger photocurrent compared to ChIEF or C1V1$_{\mathrm{T}}$ and its off-kinetics are slower (137 ms; Lin et al., 2013). I expressed *UAS-ReaChR* in PNs with *VT33006-Gal4.* Amber light stimulation strongly depolarized PNs and made them spike at high firing rates (Figure 11F). IR stimulation also elicited action potentials in PNs at high firing rates, while providing higher depth

resolution (Figure 12D).

3.3.5 Discussion

In the optogenetic probes I tested, ChR2AR and ReaChR successfully generated spikes in PNs in response to IR stimulation. Importantly, these probes evoked spikes only at restricted z-frames in response to IR stimulation (Figure 12C and 12D), conferring higher spatial resolution. ReaChR-driven firing rate is higher than that driven by ChR2AR. Because one of the aims of this study is to examine the integration of PN inputs in KCs, higher PN firing rate and subsequent larger KC depolarization is beneficial. Therefore, we decided to use ReaChR in the IR experiments described below.

Chapter 4

Origins of cell-type-specific olfactory processing in the mushroom body

4.1 KCs add inputs from multiple PNs linearly

Anatomically, KCs receive inputs from seven PNs on average (Caron et al., 2013). In response to odors, KCs generate action potentials by integrating coincident inputs from multiple PNs (Gruntman and Turner, 2013). Therefore, it is important to determine how multiple subthreshold synaptic inputs interact in KCs. A previous study examined this issue by stimulating an optogenetic probe expressed in a few glomeruli with light, and comparing the postsynaptic responses of KCs receiving various numbers of PN inputs (Gruntman and Turner, 2013). However, combinations of only three, fixed glomeruli were tested and the comparison was made between KC responses in different animals. Therefore, it remains to be investigated how individual KCs integrate synaptic inputs from multiple PNs and that belonging to various glomeruli.

I tackled the problem by optogenetically activating diverse sets of PNs connected to single KCs either sequentially or simultaneously and comparing the postsynaptic responses. I achieved this with two-photon excitation of an optogenetic probe because it provides higher spatial resolution than optogenetic activation with a continuous wave laser (Andrasfalvy et al., 2010). Specifically, I expressed ReaChR (Inagaki et al., 2014; Lin et al., 2013) in PNs in 44 out of $\sim$51 glomeruli and targeted a subset of them with a pulsed laser (Figures 13A-13C and Table 1). To stimulate individual glomeruli, I separately excited 6 $\times$ 6 regions of interest (ROIs, 12 μm $\times$ 12 μm each) placed every 5 μm along the depth to cover the entire antennal lobe (Figure 14A, see Materials and Methods).

Two-photon excitation effectively depolarized PNs in all the ReaChR-positive glomeruli tested (25/25 glomeruli; Figure 14C). Excitation with stronger laser power made these responses exceed

the spiking threshold (Figure 14D). The laser power was kept at an appropriate level to retain the high spatial resolution of optogenetic activation while evoking spikes in a substantial number of glomeruli (15/25 glomeruli; Figures 14B, 14E and 14G). These spiking responses were reliable (Figure 14F). The same stimulation also evoked clear postsynaptic responses in KCs (Figures 14B and 14G). PNs showed strong spiking responses in one ROI and weaker responses in neighboring, orthogonal ROIs (Figure 15A). The lateral resolution (full width at half maximum = 15.8 μm) was comparable to the typical diameter of a glomerulus ($\sim$10 to 15 μm, Figure 15B). As indicated by theoretical studies (Helmchen and Denk, 2005; Rickgauer and Tank, 2009), the axial resolution was relatively lower than the lateral resolution (full width at half maximum = 25.7 μm, Figure 15B). These results suggest that stimulation of a single ROI approximately corresponds to stimulation of a single glomerulus.

To examine how KCs integrate inputs from multiple PNs, I first activated two ROIs individually while recording from KCs (Figures 16A and 16B). I then stimulated these two ROIs nearly simultaneously (coactivation in Figure 16B) and compared the response to a simple summation of KC responses to individual stimulations (arithmetic sum in Figure 16B). The coactivated response matched the arithmetic sum. I tested various combinations of ROIs and found that responses were always combined linearly or slightly sublinearly in all KC types (Figure 16C). This relationship did not deviate much even for the integration of three ROIs (Figure 16D). These results demonstrate that, at the subthreshold level, KCs pool inputs from multiple PNs close to linearly, irrespective of the identity of glomeruli.

KCs do not show voltage-dependent boosting of synaptic inputs (Gruntman and Turner, 2013; Murthy et al., 2008). This argues that integration of inputs from two ROIs should not depend on the KC membrane potential. As expected, KCs combined dendritic inputs linearly at every holding membrane potential examined (Figure 16E). Smaller responses at higher holding potentials can be explained by a decrease in electrical driving force across the cellular membrane (Murthy et al., 2008).

4.2 α'/β' KCs are intrinsically more excitable

To understand how depolarizing input will lead to spikes in KCs, I examined the relationship between the membrane potential and the firing rate by injecting different amount of currents to the cell body. I found that, despite the similarity in input resistance measured at the soma (Figure 17A), the ability to generate spikes varied across cell types (Figure 17B). The rank order of excitability was α'/β', α/β, and γ. α'/β' KCs had a lower firing threshold compared to the other two cell types (Figure 17C). Intriguingly, this order of excitability can account for the previously reported rank order of broadness of odor tuning, spontaneous firing rate, and odor-evoked firing rate (Turner et al., 2008). These results suggest that the intrinsic property of KCs contributes to cell-type-specific olfactory processing in the mushroom body (see below for further examination).

4.3 PN activation recruits local, GABAergic inhibition

I found that activation of PNs also recruits inhibition in KCs. To simultaneously activate a larger number of PNs than in the case of two-photon optogenetics experiments, I expressed ReaChR in 13 PNs using *Mz19-Gal4* and activated it with wide-field illumination (Figure 18A; Gruntman and Turner, 2013; Jefferis et al., 2004). I confirmed that LED light can make *Mz19-Gal4*-positive PNs spike vigorously (Figure 8B). When these PNs were optogenetically stimulated with higher intensity of light, excitatory KC responses were followed by more salient, slow inhibition (Figures 18A and 18B). Different KCs exhibited different amount of inhibition (Figure 18C). This illustrates that individual KCs integrate both excitatory and inhibitory inputs. It has been shown that strong input to the mushroom body activates APL neuron, which provides feedback inhibition to KCs (Lin et al., 2014). This inhibition was described as all-to-all inhibition, because APL neuron inhibited all KCs at a time and blockade of output from all KCs was necessary to suppress the inhibition. Such a wide-spread inhibition, which I term here as global inhibition, is also observed in the locust mushroom body (Papadopoulou et al., 2011).

To facilitate the characterization of inhibitory input to KCs, I isolated the lateral inhibitory component by recording from KCs that were not directly connected with boutons of *Mz19-Gal4*-positive PNs (Figure 19A, see Materials and Methods). Clear inhibition was induced by light stimulation,

but unexpectedly, not in all KCs (Figure 19B). Some KCs were almost not hyperpolarized at all, suggesting that the inhibition is effective locally (Figures 19B and 19C). The lack of hyperpolarization is unlikely to be related to the health of the cell because these KCs showed normal input resistance and spiked in response to current injection to the soma.

Even though a single APL neuron innervates the entire mushroom body, I still hypothesized that it is the origin of this local inhibition from the following reasons. First, APL neuron is a putative analogue of the locust giant GABAergic neuron (GGN), which has a single cell body per hemisphere and provides inhibitory feedback to KCs (Papadopoulou et al., 2011). GGN is a non-spiking neuron. Non-spiking neurons rely on the graded potential but not action potentials to release neurotransmitters (Burrows and Siegler, 1976; Graubard, 1978). Therefore, APL neuron may utilize graded potential to release vesicles from a subset of neurites. Second, because APL neuron expresses presynaptic and postsynaptic markers throughout the neurite (Wu et al., 2013), the interactive loop between KCs and APL neuron can be closed locally at any part of the neurite.

To test this hypothesis, I first examined the neurotransmitter responsible for the inhibition. Consistent with the reports that APL neuron is immunopositive for GABA (Liu and Davis, 2009; Tanaka et al., 2008), antagonists for $GABA_A$ and $GABA_B$ receptors (picrotoxin $\left[\text{PTX}\right]$ and CGP54626 $\left[\text{CGP}\right]$, respectively) significantly decreased the inhibition (Figure 19D). Next, to directly examine whether APL neuron is the origin of local inhibition, I expressed an optogenetic silencer archaerhodopsin (Arch; Chow et al., 2010) with *APL-Gal4* (Figures 20A and 20B; Wu et al., 2013) and suppressed the activity of APL neuron. To induce inhibition, I mimicked the inputs from PNs to KCs by iontophoresing acetylcholine (ACh), a neurotransmitter released from PNs, into the mushroom body calyx (Figure 20A). The strength of the input to the mushroom body was controlled by adjusting the current for iontophoresis. With this approach, I was able to isolate a purely inhibitory component in some KCs. To ensure that the induced inhibition remains local, I confirmed that some other KCs in the same brain showed no response under the identical iontophoresis condition (Figure 20C). Under this setting, I found that light activation of Arch significantly decreased the inhibition (Figures 20D and 20E), indicating that the local inhibition originates from APL neuron.

4.4 α'/β' KCs preferentially recruit inhibition from APL neuron

Previous studies suggest that KCs directly activate APL neuron (Lin et al., 2014; Yasuyama et al., 2002). To examine how KCs recruit inhibition from APL neuron, I evoked action potentials in single KCs by injecting a current to their cell body and measured the feedback inhibition (Figure 21A), an approach applied to characterize a dendrodendritic feedback loop between mitral/tufted cells and inhibitory granule cells in the rodent olfactory bulb (Chen et al., 2000; Isaacson and Strowbridge, 1998). I found that activation of single KCs recruits a hyperpolarizing offset response, but unexpectedly, only prominently in α'/β' KCs (Figure 21B). Stronger activation of each KC proportionally induced larger offset responses in α'/β' KCs whereas responses remained small in the other two cell types (Figure 21C). KC spikes were necessary to evoke this offset response because it was abolished by the addition of TTX (Figure 21D). The offset response does not reflect intrinsically generated slow afterhyperpolarization as it was significantly reduced by GABA receptor antagonists (Figure 21E). Strong reduction in inhibition upon optical suppression of APL neuron further confirmed that the synaptic inhibition is mediated by APL neuron (Figure 21F). These results revealed that α'/β' KCs preferentially recruit GABAergic feedback inhibition via APL neuron.

4.5 APL neuron can inhibit all types of KCs with a similar strength

This cell-type-specific inhibition can be explained by two mechanisms. One possibility is that α'/β' KCs activate APL neuron more strongly than the other two types so that, in turn, they receive stronger inhibition. Another possibility is that although all three types of KCs can activate APL neuron equally, α'/β' KCs are more sensitive to inhibitory input from APL neuron. To evaluate these possibilities, I optogenetically activated APL neurons using CsChrimson (Klapoetke et al., 2014) and recorded responses from every type of KCs (Figure 22A). I found that responses were mediated by both $\mathrm{GABA_A}$ and $\mathrm{GABA_B}$ receptors (Figures 22B and 22C) and, critically, similar in strength between all types of KCs (Figures 22D and 22E). This result suggests that cell-type-specificity of inhibition originates in the ability of α'/β' KCs to activate APL neuron more strongly than the other two cell types. Furthermore, inhibition was observed in every single KCs I examined, implying that APL neuron can modulate all $\sim$2000 KCs.

4.6 The spatial extent of APL neuron activity can be lobe-specific or global depending on the olfactory input to the mushroom body

If α'/β' KCs had the privilege of preferentially recruiting APL neurons on top of higher intrinsic excitability (Figure 17), branches of APL neuron in the α'/β' lobe should be activated first as olfactory input to the mushroom body is gradually increased. To test this, I expressed the genetically encoded Ca^{2+} indicator GCaMP6s (Chen et al., 2013) in APL neurons and used two-photon microscopy to visualize their response to a strong odor (ethyl butyrate) diluted over a wide range (Figure 23A). I imaged GCaMP signals in three medial lobes (β, β', and γ; Figures 23B and 23C). As expected, I consistently observed Ca^{2+} responses in the β' lobe even to low concentrations of odor (10^{-9} and 10^{-7}), which only evoked negligible responses in the other two cell types (Figures 23D and 23E). When I gradually increased the concentration, signals appeared and grew in β and γ lobes as well (Figure 23E). This is in line with our earlier observation that optogenetic activation of APL neuron can inhibit all KCs of all types (Figure 22). Together, these results demonstrate that neurites of APL neuron in the β' lobe are indeed preferentially activated and APL neuron responds in a lobe-specific to global manner flexibly depending on the strength of the olfactory stimulus.

4.7 α'/β' KCs are more responsive and sensitive to odor presentation and carry more information about odor concentrations than other KC types

Given these differential physiological properties of KC types, one can infer that several aspects of KC responses to odors should also be cell-type-specific. First, because α'/β' KCs are intrinsically more excitable, these neurons are expected to detect odors more rapidly. To test this hypothesis, I expressed GCaMP5 (Akerboom et al., 2012) in all KCs under the control of *OK107-Gal4* (Connolly et al., 1996) and imaged the medial lobes (Figure 24A). I found that α'/β' KCs, indeed, responded to ethyl butyrate with shorter latency as compared to the other two cell types (Figures 24B-24D). Therefore, having α'/β' KCs in the circuit is beneficial in speeding up the detection of odors.

Second, from the same reason, α'/β' KCs are likely to be more sensitive to olfactory stimuli. As

expected, α'/β' KCs showed significantly larger responses to ethyl butyrate at low concentrations (10^{-9} and 10^{-7}) than the other two cell types, which remained nearly unresponsive to these stimuli (Figure 25A). Responses of α'/β' KCs increased gradually with concentration and remained strongest among responses of three cell types at all concentrations examined (Figure 25A).

This result further suggests that α'/β' KCs can better discriminate between different, especially low concentrations of odors. To test this, I quantified whether responses of α'/β' KCs carry more information about the identity of the concentration using linear discriminant decoding analysis. To quantify the decoding accuracy, for each cell type, I withheld one response from the entire data (responses to 4 repeated presentations of odors at 5 different concentrations), trained the decoder with the remaining data, and predicted the identity of the concentration that evoked the withheld response (see Materials and Methods). As hypothesized, decoding accuracy was higher for α'/β' KCs at low concentrations (10^{-9} or 10^{-7}), while performance was comparable across three cell types at higher concentrations ($\geq 10^{-5}$; Figure 25B).

Because the balance between excitation and inhibition is important for the stability of a system, I finally asked if this high discriminability of α'/β' KCs may be compromised by suppressing the feedback inhibition, which should normally control both the overall gain and the trial-to-trial fluctuation of excitatory input. Given that α'/β' KCs receive the strongest GABAergic inhibition from APL neurons (Figure 21) and branches of APL neurons are most strongly activated by odors in the β' lobe (Figure 23), I further hypothesized that blockade of GABAergic transmission in all three KCs will have the largest effect on α'/β' KCs. Indeed, although application of GABA receptor antagonists made the responses larger and more variable in all cell types, disinhibition of mean response to low concentrations of odor was particularly prominent in α'/β' KCs (Figure 25C). Consequently, the dynamic range calculated as a difference between normalized responses to the highest and lowest concentration of odor became significantly narrower in α'/β' KCs (Figure 25D). To examine how this decrease in the dynamic range and increase in variability together affect the discriminability between olfactory stimuli, I again performed a decoding analysis and found that the discriminability became lower in the presence of GABA receptor antagonists in α'/β' KCs (Figure 25E). These results suggest that feedback inhibition matched with the higher excitability is crucial for α'/β' KCs to discriminate between olfactory stimuli of various strengths.

Chapter 5

Discussion

5.1 Linear mixing of excitatory inputs in KCs

In an attempt to understand how multiple PN inputs are integrated in KCs, a previous study reported that responses of KCs are correlated with the number of PN inputs (Gruntman and Turner, 2013). However, synaptic integration remained to be investigated because the comparison was made between KCs in different animals and not within the same cell. Another study in rodents instead showed that coactivation of olfactory bulb glomeruli with glutamate uncaging induced supralinear postsynaptic responses in the piriform cortex (Davison and Ehlers, 2011). Here, I activated individual glomeruli with precision using two-photon optogenetics and found that KCs sum inputs from multiple PNs linearly, irrespective of the identity of glomeruli. Because I have likely sampled PNs connected to KC claws, dendritic structures that enwrap PN boutons (Caron et al., 2013; Gruntman and Turner, 2013), at diverse physical locations, this indicates that KCs pool inputs equally from any combination of claws. Importantly, each KC receives on average seven inputs from a random set of PNs (Caron et al., 2013) with some local rules (Gruntman and Turner, 2013). Therefore, my results suggest that $\sim$2000 KCs mix different aspects of olfactory information reaching their claws equally to create diverse odor representations. This functional organization of the mushroom body circuit is advantageous in that it represents odors distinctively in a high-dimensional coding space and thus can enhance odor discriminability (Babadi and Sompolinsky, 2014; Litwin-Kumar et al., 2017).

5.2 Local and global modes of inhibition by single APL neurons

As PNs were more strongly activated, KCs not only showed enhanced excitation but also inhibition. Inhibition followed excitation by several hundred ms and were often strong enough to override the initial depolarization (Figures 18B and 18C). This is likely one mechanism that generates spatially (Honegger et al., 2011; Lin et al., 2014) and temporally sparse odor representations in KCs (Murthy et al., 2008; Turner et al., 2008). In the locust KCs (Perez-Orive et al., 2002) and the rodent piriform cortex neurons where odors are encoded sparsely (Poo and Isaacson, 2009), excitatory input is similarly followed by global inhibition found in most cells.

What was different from the previous studies was that the effect of inhibition can be local: some KCs received prominent inhibition while others in the same brain received none (Figures 19 and 20C). Moreover, activation of single KCs by current injection was sufficient to induce feedback synaptic inhibition (Figure 21). My optogenetic silencing experiment demonstrated that this was mediated by GABAergic APL neurons even though they have been reported to innervate throughout the mushroom body and only mediate global inhibition (Lin et al., 2014). Therefore, APL neurons can exert inhibition both locally and globally. Because APL neuron is excited by KCs (Lin et al., 2014), this local processing represents an efficient solution to provide inhibition matched with the level of KC activity without necessarily inhibiting the whole system. This suggests that APL neuron serves a role in addition to the global gain control that maintains the sparseness of odor representations in the mushroom body (Lin et al., 2014).

How, then, does a single neuron innervating the entire mushroom body inhibit KCs locally? Two factors suggest dendrodendritic (or neurite-to-neurite) release as a mechanism for local inhibition. First, ectopically expressed pre- and postsynaptic markers in APL neurons distribute throughout the mushroom body (Wu et al., 2013), implying that the recurrent loop between KCs and APL neuron may close within a local region. Second, the locust analogue of APL neuron is non-spiking (Papadopoulou et al., 2011), making graded release of neurotransmitter likely in APL neuron as well. In fact, at least APL neuron does not seem to spike within an input range that evokes localized GCaMP signals in only one of the lobes (Figure 23). If spikes had been generated, I should have observed global signals in APL neuron because spikes generally elevate calcium concentration throughout the cell (Smetters et al., 1999; Yuste and Denk, 1995). This mechanism is reminiscent

of that in the mammalian olfactory bulb in which granule cells mediate lateral inhibition through dendrodendritic release in response to inputs from mitral/tufted cells (Chen et al., 2000; Isaacson and Strowbridge, 1998).

There exits another set of GABAergic neurons in the mushroom body, dorsal paired medial (DPM) neurons, that are qualified to mediate this inhibition. In each hemisphere, DPM neuron innervates the entire mushroom body except for the calyx (Tanaka et al., 2008) and connects with APL neuron via gap junctions (Wu et al., 2011). Therefore, there is a possibility that DPM neurons are also involved in inhibiting KCs.

5.3 Cell-type-specific mechanisms enhance detection speed and discrimination between different odor concentrations in α'/β' KCs

Three types of KCs pooled PN inputs in a similar manner (Figure 16). However, upon depolarization, α'/β' KCs spiked most readily, followed in order by α/β and γ KCs (Figure 17). This mirrors the rank order of broadness of odor tuning, spontaneous firing rate, and odor-evoked firing rate (Turner et al., 2008), suggesting that the intrinsic mechanism of spike generation is one of the origins of cell-type-specific responses in KCs. The heterogeneity in intrinsic excitability may reflect differential possession of voltage-sensitive conductances as recent transcriptome analyses revealed that the gene expression profile is different between KC types (Crocker et al., 2016; Perrat et al., 2013).

Incidentally, α'/β' KCs were also the most effective in recruiting feedback inhibition by APL neurons (Figure 21). This can be either due to preferential activation of APL neuron by α'/β' KCs or preferential inhibition of α'/β' KCs by APL neuron. Our results supported the former because optogenetic activation of APL neurons inhibited all three types of KCs equally (Figure 22). This conclusion was corroborated by our additional observation that APL neuron exhibits highest sensitivity and responsiveness to odors in the β' lobe (Figure 24). How do α'/β' KCs more effectively activate APL neuron? First factor is their higher intrinsic excitability. Because they generate spikes more readily, the total drive to the APL neuron will be larger under a particular input to the mushroom body. Second is their stronger functional connection with the APL neuron.

Because the same number of spikes evoked larger inhibition in α'/β' KCs (Figure 21C), these cells likely form stronger or more abundant synapses with APL neurons. This is in line with the anatomical observation that APL neurons contact most densely with α'/β' KCs in the lobes (Pitman et al., 2011).

The three types of KCs have been morphologically subdivided into finer categories in some studies (Aso et al., 2014a; Costa et al., 2016; Lin et al., 2007; Tanaka et al., 2008). In terms of function, α/β core and α/β surface KCs, for example, are shown to be involved in different aspects of olfactory learning (Perisse et al., 2013). Therefore, although I did not find clear clusters in our data within each of the three conventional cell types, there may be additional complexity in cell-type specificity.

Based on the differences in physiological properties between KC types, I was able to predict and confirm previously unidentified functions of α'/β' KCs in odor processing. As suggested by higher intrinsic excitability, α'/β' KCs detected ethyl butyrate with shortest latency and highest sensitivity (Figures 24 and 25). This allowed α'/β' KCs discriminate between different odor concentrations most accurately, which required balanced feedback inhibition by APL neuron (Figure 25). These results indicate that, by having α'/β' KCs, the mushroom body circuit can enhance the detection speed, sensitivity, and discriminability of different odor concentrations. Notably, the actual decoders of the KC activity, the mushroom body output neurons, innervate particular compartments in the lobes to contact generally one of three KC types (Aso et al., 2014a). These mushroom body output neurons encode valence and bias the behavior towards attraction or aversion in various learning tasks (Aso et al., 2014b; Owald et al., 2015). Therefore, the mushroom body output neurons innervating the α'/β' lobes may shape the fly's initial behavioral response to an odor and that with a higher sensitivity and discriminability.

5.4 Applicability of the results obtained with ethyl butyrate to other odors

To predict odor responses of KCs, I used one specific odor, ethyl butyrate, throughout the study and I did not test other odors. Therefore, one may argue that the results I showed with odor stimulation

are specific to this particular odor. Although I cannot exclude this possibility, I believe that my results can be generalized to any odor from the following reasons.

First, in calcium imaging experiments, I recorded the average fluorescence at the tip of each lobe, which is innervated by the axons of all the KCs of a particular type. This means that what I have reported is the overall activity of all the KCs belonging to a particular type. Second, because all types of KCs sample activity of random combinations of PNs, the overall activity of each KC type should reflect that of total PNs. Therefore, although different odors recruit PNs belonging to different combinations of glomeruli, the information about the identity of odor is lost in the overall activity of PNs. Taken together, my results are dependent on the total activity of PNs and KCs but not on the identity of odors. Finally, regardless of the identity, higher concentrations of odors evoke stronger responses in PNs (Bhandawat et al., 2007) and KCs (Endo et al., unpublished data). Thus, similar response patterns to different concentrations of odors should be observed regardless of the identity of the odor.

5.5 Discrimination between different odors versus different concentrations of the same odor

In this dissertation, I have exclusively focused on discrimination between odor responses evoked by different concentrations of the same odor (ethyl butyrate). However, my results can be extended to discrimination between different odors from the following reason. Although different odors activate PNs in different combinations of glomeruli, a single odor typically recruit additional glomeruli as concentration is increased and thus recruit different combination of glomeruli. Therefore, from the perspective of population glomerular activity, changing the concentration of a particular odor has similar consequences to changing the identity of odors.

5.6 Ethological plausibility of odor concentration used in the study

Ethyl butyrate is a fruity odor: similar to the flavor of a pineapple. When flies first detect the odor from the food at a distance, the concentration of the odor is very low due to passive diffusion. As

the fly approaches the food and finally land on it, the concentration becomes very high. Therefore, the fly experiences a wide range of concentration from low to high, making various concentrations of an odor that I used in this study all relevant for animal behavior.

5.7 Relevance of cell-type-specific mechanisms to other known functions of the mushroom body and animal behavior

5.7.1 Memory processing

Three types of KCs pool PN inputs in a similar manner (Figure 16) but spike differently (Figure 17). Interestingly, the order of cellular excitability matches the temporal sequence in which olfactory memory traces appear in different lobes: modulated odor responses are observed between 0-1 h in the α'/β' lobe (Cervantes-Sandoval et al., 2013; Wang et al., 2008), 9-24 h in the α/β lobe (Akalal et al., 2011; Cervantes-Sandoval et al., 2013; Yu et al., 2006), and 18-48 h in the γ lobe (Akalal et al., 2010) after olfactory associative learning. Sustained memory traces might appear first in the α'/β' lobe because it is composed of the most excitable KC type and because this cell type preferentially contacts the dorsal paired medial neuron, whose activity is hypothesized to consolidate memories (Krashes et al., 2007; Pitman et al., 2011; Wu et al., 2011). On the other hand, memory traces in α/β and γ lobes appear only after the formation of late-phase memories that requires protein synthesis (Krashes and Waddell, 2008; Tully et al., 1994). The less excitable α/β and γ KCs might require the incorporation of additional molecular components to show elevated odor responses. Transcriptome analyses have revealed that the gene expression profile is different between KC types (Crocker et al., 2016; Perrat et al., 2013) and it can change following long-term memory formation in some mushroom body neurons (Crocker et al., 2016). This approach should help reveal the molecular basis of cell-type-specific physiology I found in this study as well as the dynamic memory traces.

Recent work indicates that olfactory memories are embedded in synapses made between KCs and their postsynaptic mushroom body output neurons through modulation by dopaminergic neurons (Aso et al., 2014a; Aso et al., 2012; Aso and Rubin, 2016; Burke et al., 2012; Cohn et al., 2015; Hige et al., 2015; Liu et al., 2012; Owald et al., 2015; Yamagata et al., 2015). Each mushroom body output neuron encodes a particular valence (Aso et al., 2014b; Owald et al., 2015) and each

dopaminergic neuron specifies the characteristics of memory formed in distinct synapses (Aso et al., 2012; Aso and Rubin, 2016; Yamagata et al., 2015). Because KCs, mushroom body output neurons and dopamine neurons all interact in a circuit (Aso et al., 2014a; Ichinose et al., 2015), the cell-type-specific physiology found in KCs also is likely to contribute to the processing of distinct memories stored in individual synapses.

5.7.2 Decision making

A previous study revealed that olfactory decision making by *Drosophila* can be explained by the drift-diffusion model, and activity of α/β KCs expressing *FoxP* gene determine both reaction time and accuracy of decision (DasGupta et al., 2014). However, the physiological mechanisms underlying this process are not well understood. Although the influence of suppressing α'/β' KCs or APL neurons on this task has not been reported, several inferences can be made based on the physiological findings of my study.

I showed that α'/β' KCs are activated first by odor stimulation (Figure 24), and they strongly recruit lateral inhibition from APL neurons (Figures 20 and 21). Besides, APL neurons can inhibit α/β KCs (Figure 22), including those expressing *FoxP*. Therefore, local lateral inhibition initiated by α'/β' KCs may inhibit some *FoxP*-expressing α/β KCs. As a consequence, only *FoxP*-expressing α/β KCs that receive strong excitatory drive to overcome this inhibition might be capable of contributing to decision making. This suggests the presence of additional uncharacterized complexity underlying mechanisms of decision making.

Silencing *FoxP*-expressing α/β KCs lead to two outcomes: prolongation of reaction time and less accurate decision (DasGupta et al., 2014). As for the reaction time, excitability of these cells is expected to be important (DasGupta et al., 2014). For this aspect, inhibition of KCs by APL neuron seems disadvantageous, because it merely slows the speed of decision making by decreasing the excitability of *FoxP*-expressing α/β KCs. However, inhibition may contribute to enhancing the accuracy of decision. Previous study showed that suppressing the neurotransmitter release from APL neurons made the KC representations less sparse and decorrelated, which led to the decrease of behavioral performance in discrimination of similar odors (Lin et al., 2014). Given that APL neurons inhibit all KCs (Figure 22), inhibition from APL neuron to *FoxP*-expressing α/β KCs may

contribute to more accurate decision by setting a proper level of sparseness and correlation.

Chapter 6

Conclusion

In this study, I aimed to understand the physiological mechanisms underlying cell-type-specific odor responses of KCs. I found that all types of KCs add inputs from multiple PNs linearly, α'/β' KCs have the highest intrinsic excitability as well as the ability to recruit local inhibition. From these physiological properties, I predicted and confirmed a superior function of α'/β' KCs in odor processing: they detect odors with shortest latency and contribute to the accurate discrimination of odor concentrations. From a broad perspective, this represents the discovery of cell-type-specific circuit mechanisms underlying sensory computations.

Appendix

Lethality

I found that progenies of some Gal4 lines crossed with UAS lines were lethal: they died either at a larval (1st or 2nd instar) or pupal stage, depending on the genotype of the progeny. This problem is not specific to our lab, because similar observation was reported by another lab that expressed ChR2 with *OK371-Gal4* (Liu and Wilson, 2013). Although the lethality may be caused by any one or combination of complex molecular interactions at each developmental stage, I could, at least, exclude some possibilities as described below.

A cross involves lethality if the number of adult progenies carrying single copies of Gal4 and UAS is significantly below the mathematical expectation based on the Mendel's law. Lethality derived from balancer chromosomes is excluded for the estimation of Gal4/UAS-derived lethality. In the cross between *NP225-Gal4/CyO* (II) and *UAS-ReaChR/CyO* (II), for example, one third of the progenies are expected to be *NP225-Gal4/UAS-ReaChR*, because *CyO* is a balancer chromosome (*CyO/CyO* is lethal).

I frequently observed lethality when the cross involved UAS lines encoding optogenetic probes such as wild type ChR2 or ReaChR, although I did not systematically test UAS lines encoding non-optogenetic constructs (Tables 2 and 3). Therefore, I hypothesized that the unregulated basal activity of optogenetic probes causes the lethality. To test this possibility, I crossed *UAS-C1V1*$_{\mathrm{T}}$ line with *NP225-Gal4* (pan-PN line) and *pebbled-Gal4* (pan-ORN line). Importantly, C1V1$_{\mathrm{T}}$ does not depolarize fly neurons even under the presence of strong light of preferred wavelength (Figures 11C and 11D). Therefore, if C1V1$_{\mathrm{T}}$ causes lethality, this means that unregulated activity of optogenetic probes is unlikely to be the major cause of the phenomenon. To further reduce the baseline activity of optogenetic probes, I reared the flies in dark and kept them on the standard fly food (namely, negligible provision of trans form of retinal). I found that progenies of *UAS-C1V1*$_{\mathrm{T}}$ line crossed with *NP225-Gal4* and *pebbled-Gal4* showed lethality (Table 4): they died at a larval stage, implying

that the unregulated activity of optogenetic probes is unlikely to be the cause of lethality. In addition, if the unregulated photocurrent generates lethality, expression of optogenetic probes that generate a similar level of photocurrents such as ReaChR and CsChrimson should result in an equal level of lethality. However, whereas the combination of *NP225-Gal4* and *UAS-ReaChR* induced lethality, the combination of *NP225-Gal4* and *UAS-CsChrimson* did not (Tables 2 and 3), further excluding the possibility that unregulated photocurrent causes lethality.

I next examined if the high expression level of Gal4-driven UAS construct is responsible for lethality. To suppress the Gal4 expression, I used temperature-sensitive Gal80 (Gal80ts; McGuire et al., 2003). Under the restrictive temperature ($\sim$18 $^{\circ}$C), Gal80ts represses Gal4 expression to the undetectable level. Higher temperature ($>$ 25 $^{\circ}$C) removes the influence of Gal80ts and restores Gal4 expression. I crossed *pebbled-Gal4; tubP-Gal80ts* fly line with *UAS-C1V1$_{\mathrm{T}}$-p2A* line to test the influence of Gal80ts, because flies carrying both *pebbled-Gal4* and *UAS-C1V1$_{\mathrm{T}}$-p2A* were lethal, irrespective of the rearing temperature (Table 4). The flies were reared in 18 $^{\circ}$C at all developmental stages. I found that the ratio of the progenies carrying all Gal4, Gal80ts, and UAS exceeded the expected value, showing that suppression of Gal4 expression contributes to the avoidance of the lethality (Table 4). This result suggests that the expression level of Gal4/UAS is crucial for the lethality.

Non-physiological increase of membrane potential under IR stimulation

As described in Chapter 3, the photocurrent elicited by two-photon excitation was expected to be smaller than that elicited by CW-light excitation. There are two basic strategies to increase the photocurrent in a neuron expressing an optogenetic probe: increasing the expression level of the probe or illuminating the molecule with higher intensity of light. In *Drosophila*, the expression level of a UAS reporter is determined by three factors: intrinsic expression level of Gal4 of the Gal4 driver, rearing temperature (higher temperature leads to higher Gal4 expression) and age (older flies have higher expression level because of the accumulation in case Gal4 lines continue to express Gal4). Among these, rearing temperature and speed of aging is related: higher temperature leads to

faster aging (Greenspan, 1997). To conduct electrophysiological recordings in adult flies, the ideal age is 2-4 days after eclosion if kept at 25 °C. Therefore the room to increase the expression level of an optogenetic probe is limited.

Before using *UAS-ReaChR* released in 2014 (Inagaki et al., 2014) to evoke action potentials with IR stimulation, I illuminated the optogenetic probes available at the time such as ChR2, ChETA or ChIEF with higher intensity of IR to increase the photocurrent. I found that the membrane potential of recorded PNs increased rapidly and irreversibly upon application of the strong intensity of IR (Figure 26A). The phenomenon could also be observed in cells without expression of optogenetic probes (data not shown). Repetitive applications of IR laser brought the membrane potential to around 0 mV. I wondered if IR light damages the plasma membrane physically so that the intracellular potential becomes equal to that of the extracellular side (membrane potential = 0 mV). To analyze this possibility, first I injected a fluorescent dye (Alexa 488, MW = 570, A10436, Sigma) into PNs through patch-clamping and examined whether the dye escapes from the intracellular side (Hirase et al., 2002; Figure 26B). I found that the dye stayed inside the cell after IR stimulation, even though the membrane potential jumped up to $\sim$0 mV.

In mammalian neurons, violet-blue light (400-490 nm) produces H_2O_2 through an oxidase (Hockberger et al., 1999). H_2O_2 damages the cell and increases the membrane potential, which can be prevented by applying anti-oxidants such as astaxanthin (Sacconi et al., 2006). I tested the published protocol (Sacconi et al., 2006) and applied astaxantin (013-23051, Wako Pure Chemical Industries) dissolved in 20% Pluronic in DMSO (P3000MP, Molecular Probes) at 20 mM to the brain. Incubation of the brain in astaxantin solution did not prevent the rapid increase of membrane potential in *Drosophila* PNs (Figure 26C).

As described, I was unable to identify why IR stimulation evoked the rapid increase of membrane potential. However, because the phenomenon was observed when the cells were illuminated with higher intensity of IR, one can avoid this trouble by applying weaker intensity of laser to the recently developed optogenetic probes such as ReaChR or CsChrimson. Because theses probes require lower intensity of an IR laser to generate spikes in PNs, the non-physiological increase of membrane potential can be avoided by using such probes.

Putative PN-to-KC transfer function determined by optogenetic stimulation

Single photon stimulation

Odor evokes fluctuation in PN firing rate (Bhandawat et al., 2007), which determine the amount of depolarization in KCs. I conducted a pilot experiment to examine the impact of single PN's spiking activity on postsynaptic KCs. To directly stimulate PNs, I expressed ReaChR with *Mz19-Gal4*, which labels 13 PNs innervating three glomeruli (DA1, VA1d, and DC3; Figure 27A; Gruntman and Turner, 2013; Jefferis et al., 2004). ReaChR was stimulated by blue light of various intensities to drive PNs at different firing rates. To analyze the KC responses to an input from only single PNs, I utilized the morphological characteristics of KCs. In the mushroom body calyx, each KC forms dendritic claws that enwrap boutons at axon terminals of PNs (Caron et al., 2013; Leiss et al., 2009). Because each claw receives input from only one PN bouton (Caron et al., 2013; Leiss et al., 2009), the number of inputs that the recorded KC receives from *Mz19-Gal4*-positive PNs can be evaluated by counting the number of claws enwrapping boutons of these PNs (Figure 27B; Gruntman and Turner, 2013). I focused on KC synapses made with DA1 PNs because these connections were expected to appear more frequently (Caron et al., 2013). These synapses could be distinguished from others based on the considerably higher sensitivity of DA1 PNs to blue light (Figure 27C).

Whole-cell recordings from PNs and KCs showed that both the PN firing rate and the KC postsynaptic response increased as the intensity of applied blue light was increased (Figure 27D). I evaluated the KC response shortly (200 ms) after the onset, because some KCs received inhibition after $\sim$200 ms upon stronger illumination as described in Chapter 4 (Figure 18B). I found that KC responses scaled linearly with the PN spiking activity throughout the typical range of PN firing rate (Figures 27E and 27F; Bhandawat et al., 2007). Therefore, the degree of PN spiking activity is faithfully transmitted to KCs.

Importantly, however, although I focused the blue light on the antennal lobe, I cannot exclude the possibility that stronger intensity of blue light may have stimulated the PN's presynaptic terminals directly, as well as evoking spikes by stimulating the spike initiation zone. The direct stimulation of presynaptic terminals and subsequent releases of neurotransmitter onto postsynaptic KCs may

not be correlated with PN firing rate; rather, they may be related to the intensity of blue light. In other words, the KC responses I reported might include both the release driven by spikes and direct stimulation of presynaptic terminals. The influence of the latter on KC depolarization may continuously increase as a function of light intensity even after the PN spike rate plateaus, which might have contributed to the linear PN-to-KC transfer function I reported.

There are three methods to distinguish between the spike-driven release and the direct stimulation-driven release. The first is the same experiment as described above but in the presence of TTX to isolate the direct stimulation-derived component. TTX suppresses spike generation by blocking a voltage-dependent Na^+ channel. Therefore, if the recorded KC shows significant depolarization at certain intensity of blue light under TTX, the response is generated by direct stimulation but not spikes.

The second approach is to stimulate the antennal lobe glomeruli through ACh iontophoresis. ACh released at the ORN terminals stimulates PNs, but does not have a direct influence on KCs. In addition, glia enwrapping individual glomeruli prevents ACh from diffusing to neighboring glomeruli. Injection of ACh into glomerulus takes the advantages of these two features.

The third approach is two-photon optogenetics. IR stimulation of the antennal lobe can be used to evoke spikes in PNs without directly activating their presynaptic terminals because of its higher spatial resolution. The result of this approach is described in more detail below.

Two-photon stimulation

In the previous section, by stimulating *Mz19-Gal4*-positive PNs, I showed preliminary evidence that KCs respond proportionally to the firing rate of DA1-PNs. In the experiments described in Chapter 4 (genotype of the flies is *VT33006>ReaChR*), I stimulated the most strongly responding ROI at various intensities of IR to drive PNs at different firing rates while recording from a postsynaptic PN. Both PNs and KCs responded proportionally to the intensity of an IR laser (Figures 28A and 28B). By combining these data, I found that the relationship between the PN firing rate and the KC response was linear within a certain range of PN firing rate (Figure 28C). I observed similar results in 8 different glomeruli, suggesting that the relationship between the PN firing rate and the KC response is linear irrespective of the identity of the glomerulus.

Dual whole-cell recording from PNs and KCs

To analyze the transformation between PNs and KCs, I first attempted dual whole-cell recordings from a PN and a KC. Dual whole-cell recording from pre- and postsynaptic neurons is a powerful technique, because it can reveal the relationship between the presynaptic firing rate and the postsynaptic response, the strength and the plasticity of synapses, and the existence of electrical synapses. Given that single KCs receive inputs from on average seven out of ∼150 PNs (Caron et al., 2013), the probability of recording from one of the connected PNs is 4.7% (7/150). To increase the probability, I expressed either CsChrimson or ReaChR using *Mz19-Gal4* line to label 13 PNs that innervate three glomeruli. A previous study showed that the KCs connected with the glomeruli labeled by *Mz19-Gal4* driver appeared more frequently (Caron et al., 2013). If a randomly selected KC shows depolarization to the blue light stimulation to *Mz19-Gal4*-positive 13 PNs, the probability that I can record from one of the connected PNs is 7.7% (1/13). In case the recorded KC did not show depolarization in response to optogenetic stimulations, I recorded from randomly selected PNs.

I recorded from 40 PN-KC pairs (n = 14 KCs and 40 PNs, including 7 *Mz19-Gal4*-positive PNs). Only one pair seemed to be connected, because the KC showed depolarization in response to PN spikes driven by the current injection into the PN cell body (Figures 29A and 29B). However, I lost the cells before conducting additional experiments. Given the low probability of hitting a pair of connected PNs and KCs (2.5% = 1/40) and the difficulties in performing dual whole-cell recordings, I decided not use this approach and used the method described in the previous section instead.

Induction of single action potentials in PNs

To characterize the synaptic transmission between PNs and KCs, it is useful to develop a protocol that can generate single action potentials in PNs. I attempted to achieve this with two methods: current injection into PN cell bodies or optogenetics. In both methods, the spike should ideally appear with a short latency after the onset of the stimulation, because the latency determines the maximum firing rate a particular method can evoke. For example, a given PN should generate two action potentials within 5 ms to mimic firing at 200 spikes/s.

Current injection to PN cell bodies

I first performed current clamp recordings from PNs. Action potentials were generated by injecting currents into the cell body. With the fixed current amplitude, longer duration increased the probability of spike generation (Figure 30A), whereas with the fixed duration, larger current amplitude shortened the time to spike (Figure 30B). However, although larger currents shortened the latency, it could not be made shorter than 20 ms (Figure 30C), which limits the maximum firing rate to 50 spikes/s. Injection of a larger current ($\sim$100 pA) tended to damage PNs.

This long latency is partially due to the time it requires to charge the membrane capacitance, because the response of a model cell to current injections (Molecular Devices) also showed slow rise kinetics (Figures 30D and 30E). Contrary to the current clamp, in voltage clamp, currents rapidly follow the change in the membrane potential (Figure 30F). Therefore, I next tried to generate a transient current that reflects an action potential ("action current"; Kazama and Wilson, 2008). In the voltage clamp mode, $\sim$8 ms of stimulation was required to generate an action current (Figure 30G), which corresponds to 125 spikes/s. The jitter of spike timing was small ($\ll$ 1 ms; Figure 30H).

A previous study showed that the spike initiation zone of PNs is distant from the soma (Gouwens and Wilson, 2009), suggesting that a longer time is required to charge the spike initiation zone with current injections at the cell body. Therefore, I next applied the optogenetic method to stimulate the spike initiation zone of PNs directly.

Optogenetics

Many optogenetic probes have been designed for generating action potentials in neurons at various stimulus frequencies. This is achieved by making the off-kinetics faster, while maintaining the photocurrent high enough to exceed the firing threshold. I tested four probes: ReaChR, CsChrimson, ChETA and ChR2AR. The off-kinetics of the probes is: 137 ms for ReaChR (Lin et al., 2013), 15 ms for CsChrimson (Klapoetke et al., 2014), and 4.8 ms for ChETA (Gunaydin et al., 2010). In case of ChR2AR, transient blue light will keep the channels in an open state until amber light is applied.

I found that controlling the spike timing with optogenetic probes is difficult. The probes with higher photocurrent such as ReaChR and CsChrimson evoke trains of action potentials but not

single spikes, in response to even a short pulse of light (Figures 31A1 and 31A2). This is because the membrane potential does not decay instantaneously after the removal of optical stimulation. In ChETA and ChR2AR, photocurrents were too low to generate an action potential (Figures 31A3 and 31A4).

Together, although spikes can be evoked at ∼125 spikes/s in PNs in a voltage-clamp mode, I did not employ this method because there is a need to perform dual recordings from PNs and KCs to characterize synaptic transmission.

Wavelength specificity of optogenetic activation of PNs

Each optogenetic probe has a preferred wavelength. ReaChR and CsChrimson are red-light sensitive (Klapoetke et al., 2014; Lin et al., 2013), whereas Arch is green-amber light sensitive (Chow et al., 2010). To examine the wavelength specificity of the probes expressed in *Drosophila* neurons, I illuminated the probes at various wavelengths of light. Interestingly, ReaChR and CsChrimson showed low wavelength dependency (Figures 32A and 32B): PNs expressing these probes showed depolarization at a similar level, irrespective of the wavelength. In contrast, Arch hyperpolarized the PN maximally with green-amber light stimulation (Figure 32C).

p2A-based separation of opsins and fluorescent proteins in olfactory neurons

In optogenetic experiments, fly lines carrying either *opsin-p2A-EYFP* or *opsin-ts-EYFP* were newly generated. The *p2A* sequence induces cleavage events, resulting in the release of individual protein products (Osborn et al., 2005). The trafficking signal (*ts*) enhances the localization of opsins and fluorescent proteins to membranes (Gradinaru et al., 2010). A prior study in rodent neurons showed that a *p2A* motif indeed led to a separation of an *opsin* and *EYFP*, resulting in the differential expression of proteins in a cell: p2A-EYFP localized in the cell body whereas ts-EYFP localized in the processes (Prakash et al., 2012). I tested whether the same phenomenon occurs in *Drosophila* olfactory neurons.

I crossed *UAS-ChR2AR-p2A-EYFP* and *UAS-ChR2AR-ts-EYFP* with *NP225-Gal4.* Consistent with the previous observation that *p2A* separates the peptides effectively in cultured *Drosophila* cells or larval motor neurons (Daniels et al., 2014), EYFP signal was detected in different locations in the antennal lobe (Figure 33A and 33B). p2A-EYFP signal was strong in PN cell bodies and weak in dendrites and axons, whereas signal from ts-EYFP was strong in processes and weak in cell bodies. Differential expression pattern of EYFP suggests that *p2A* cleavage successfully separate an opsin and a fluorescent molecule as shown in the mammalian neurons (Prakash et al., 2012).

The spatial extent of APL neuron activity within a lobe

GCaMP imaging experiments in Chapter 4 showed that the activity level of APL neuron's neurites differed in different lobes (Figure 23). In a separate experiment, I confirmed the observation with iontophoresing ACh into the calyx (Figure 34A). Similarly to the experiment described in Figure 23, I measured the GCaMP signal at the tip of the lobes (Figure 34B). Quantitative analysis showed that Ca^{2+} signal first appeared in the β' lobe (Figures 34C and 34D), consistent with the result that α'/β' KCs preferentially recruit inhibition from APL neuron (Figures 21). As the current amplitude became stronger, β and γ lobes were recruited in this order (Figures 34C and 34D).

Thus, APL neuron's activity in the β' lobe is higher than that in the other lobes. However, as shown in Figure 19B, not all α'/β' KCs are inhibited at a time. This implies that APL neuron can act locally even within a lobe. If so, GCaMP expressed in APL neuron within a lobe should exhibit localized signals. To test this, I iontophoresed ACh into the calyx (Figure 35A) and examined the activity of APL neuron in response to weak stimulation, which may be difficult to achieve with odor stimulation. I imaged GCaMP responses in the β' lobe (Figure 35B). Note that because APL neuron innervates all three medial lobes, it is difficult to distinguish between the lobes based on fluorescence. Therefore, I first imaged the baseline fluorescence from the β' lobe tip, as shown in Figure 23, and traced the neurite back to the middle of the lobe.

As expected, at low current, the Ca^{2+} response was spatially localized to nearly a single neurite (Figure 35B). When I gradually increased the amount of current, the responding area continued to increase until it covered the entire medial lobes (Figure 35B4, 35B5, and 35C). These results

demonstrate that the spatial extent of APL neuron's activity can vary from a single neurite to the entire lobes, depending on the level of KC activity.

Construction of a thin fluorescent film

In the initial experiments, I attempted to measure the point spread function (PSF) of the two-photon microscope. My aim was to increase the two-photon-elicited photocurrent by enlarging the PSF. To measure the PSF of laser scanning microscopes, a thin fluorescent film or fluorescent beads are often used. I developed a protocol to create a thin (< 100 nm) fluorescent film and measured its thickness with an atomic force microscope (AFM). I prepared 1 wt% and 5 wt% polyvinyl alcohol (PVA; 163-03045, Wako Pure Chemical Industries) dissolved in pure water (18 $^{\circ}$C). The PVA solutions were, then, mixed at 1 wt% : 5 wt% = 5 : 1. The fluorescent molecule, rodamine 6G, was dissolved in the PVA solution at 0.1 M. 10 μl of PVA-Rodamine solution was placed at the center of the cover glass (Figure 36A). A thin fluorescent film was generated by rotating the cover glass (spin coating; Figure 36B; 1H-D3 spin coater, Misaka). The rotation protocol was 500 rpm for 5 sec, 1000 rpm for 5 sec, and 2500 rpm for 20 sec.

The thickness of the fluorescent film was measured by a tapping mode AFM (NS3A-FNUAS01-S, Bruker AXS). AFM uses the forces between the probe at the tip of the cantilever and the sample (Figure 36C). In the tapping mode AFM, the cantilever is driven to oscillate at a certain amplitude and frequency. The cantilever scans the surface of the sample with tapping. The interaction between the cantilever and the sample disturbs the constant oscillation. The servo motor that controls the height of the stage receives the feedback signal from the cantilever and it regulates the stage up and down so that the oscillation of the cantilever is kept constant; if the height of the sample increases, the servo motor moves the stage down so that the cantilever can keep the tapping amplitude, and if the height of the sample deceases, the motor moves the stage up to detect the response to tapping. The movement of the stage is quantified as the height of the sample, or thickness.

To measure the thickness of the fluorescent film, a small portion of the film was removed by scratching (Figure 36D), and the thickness was measured as the axial distance between the surface of the film and the cover glass (Figure 36E). I found that 1 wt% : 5 wt% = 5 : 1 PVA solution

generated 45-100 nm film (Figure 36F). Adding 5 wt% solution resulted in the increase of the thickness of the film.

Figures

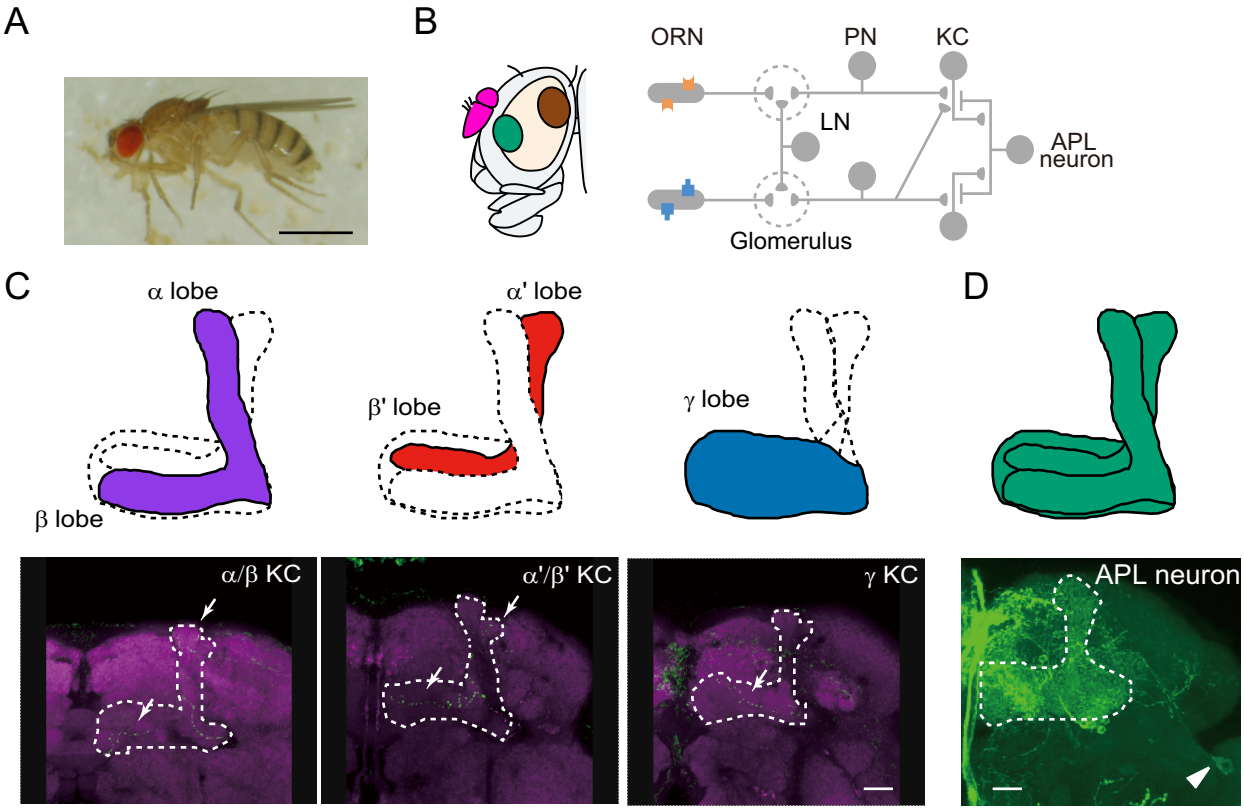

Figure 1: The adult *Drosophila* and its olfactory circuit
(A) The adult female *Drosophila.* Scale bar, 1 mm.
(B) Left, schematic of a fly head. Odor information detected by the antenna (pink) is transformed in the antennal lobe (green), and then in the mushroom body (brown). Right, the *Drosophila* olfactory circuit.
(C) Schematic of the mushroom body lobes innervated by different KC types and immunostained images of biocytin-filled single KC neurites (green, neuropil in magenta). Dotted line indicates the outline of the mushroom body. Arrow indicates the dye signal in lobes. Scale bar, 20 μm.
(D) Schematic of the arborization of APL neuron in the left hemisphere and the immunostained image (anti-GFP in green). Arrowhead indicates the cell body. Dotted line indicates the outline of the mushroom body. APL neuron innervates the entire mushroom body. Scale bar, 20 μm.

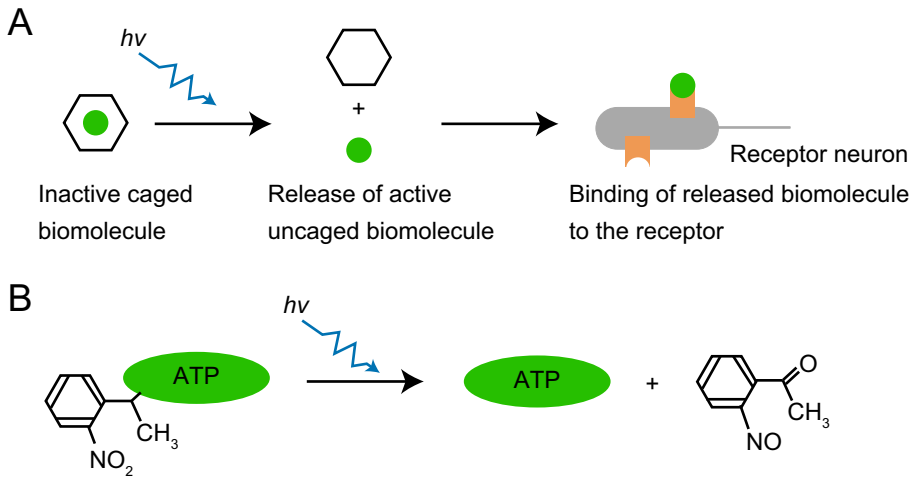

Figure 2: Mechanism of uncaging
(A) Schematic of uncaging. A caged compound is a biomolecule that is made inactive by the attachment of the caging chemical. The biomolecule is released from caging chemical upon absorption of the uncaging light. The released biomolecule can bind to the receptor.
(B) Photochemistry of NPE-caged ATP as an example. ATP cannot bind to its receptor unless the uncaging light liberates it from the caging chemical (NPE).

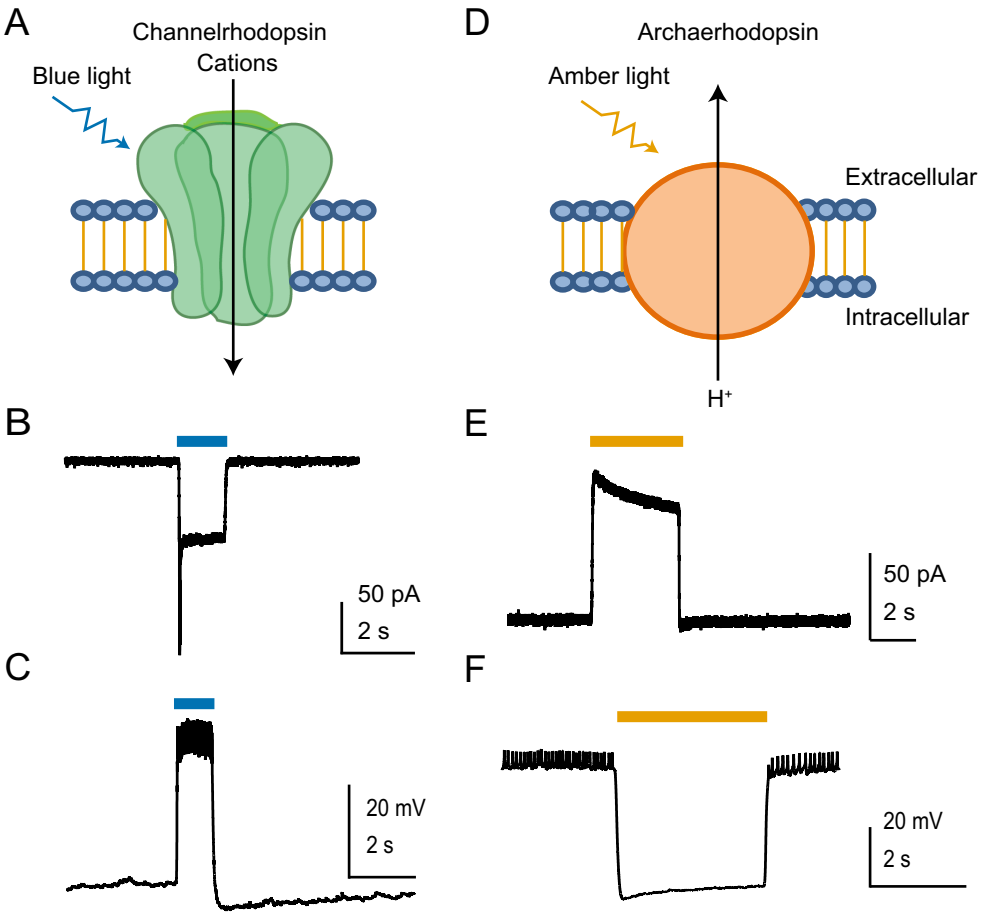

Figure 3: Optogenetic probes depolarize/hyperpolarize neurons
(A) Schematic of a channelrhodopsin molecule. Channelrhodopsin is a non-selective cation channel that opens during the application of blue light.
(B) Sample current response of a PN expressing ChR2 showing the inward photocurrent evoked by light application. Voltage was clamped at −60 mV.
(C) Sample light response of a PN expressing ChR2 in a current-clamp mode.
(D) Schematic of an archaerhodopsin (Arch) molecule. Arch is a proton-selective ion pump that hyperpolarizes the cellular membrane in response to amber light.
(E) Sample current response of a PN expressing Arch showing the outward photocurrent evoked by light application. Voltage was clamped at −60 mV.
(F) Sample light response of a PN expressing Arch in a current-clamp mode.

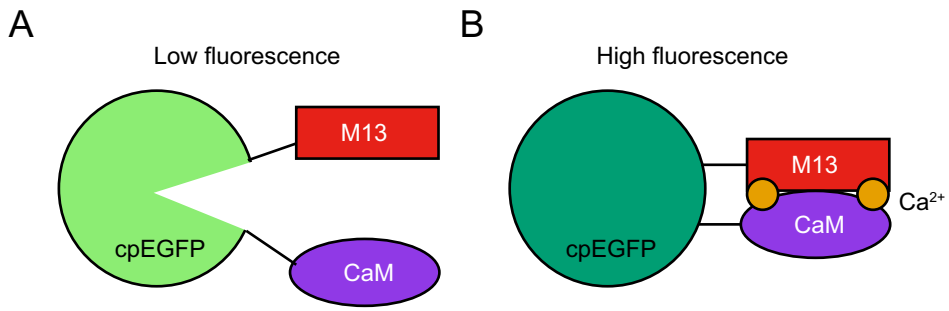

Figure 4: A genetically encoded calcium indicator GCaMP
(A) Inactive form of GCaMP.
(B) Active form of GCaMP. GCaMP go through a conformational change after binding to Ca^{2+}, resulting in an increase of fluorescence.

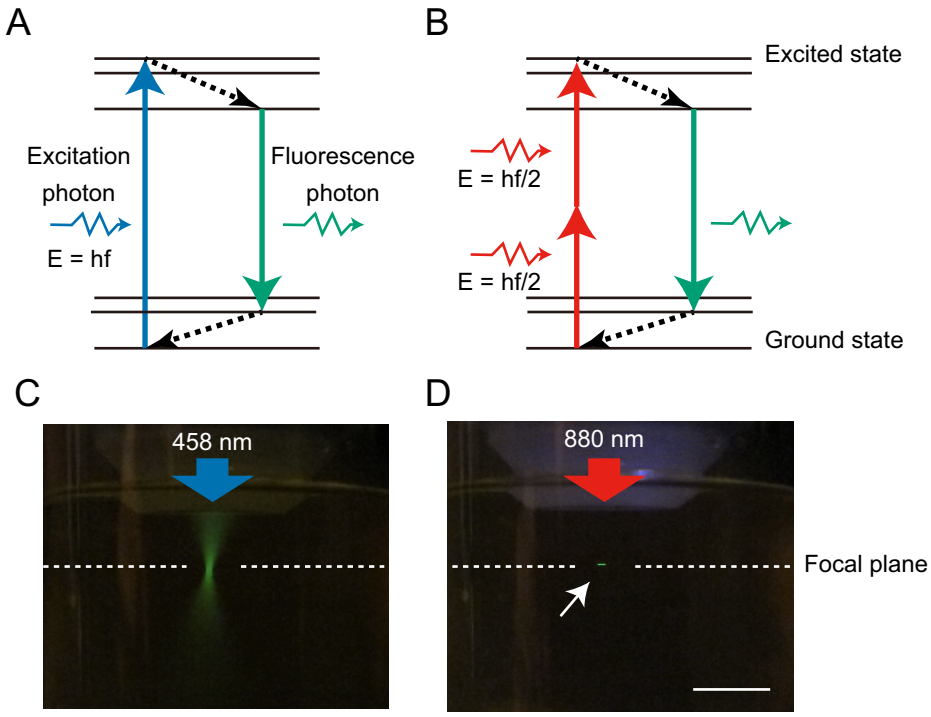

Figure 5: Mechanism of two-photon excitation

Jablonski diagram illustrating single-photon excitation (A) and two-photon excitation (B). In the two-photon excitation process, two photons that have half the energy compared with the photon that evokes single photon excitation, contribute to the transition from the ground state to the excited state.

Application of light with a 458 nm CW laser (C) or 880 nm pulsed IR laser (D) to the fluorophore (vitamin B_2 in Lipovitan D, 1:100 dilution, Taisho Pharmaceutical). Green, fluorescence. Arrow indicates fluorescence exclusively generated at the focal point by two-photon excitation. Scale bar, 0.5 mm.

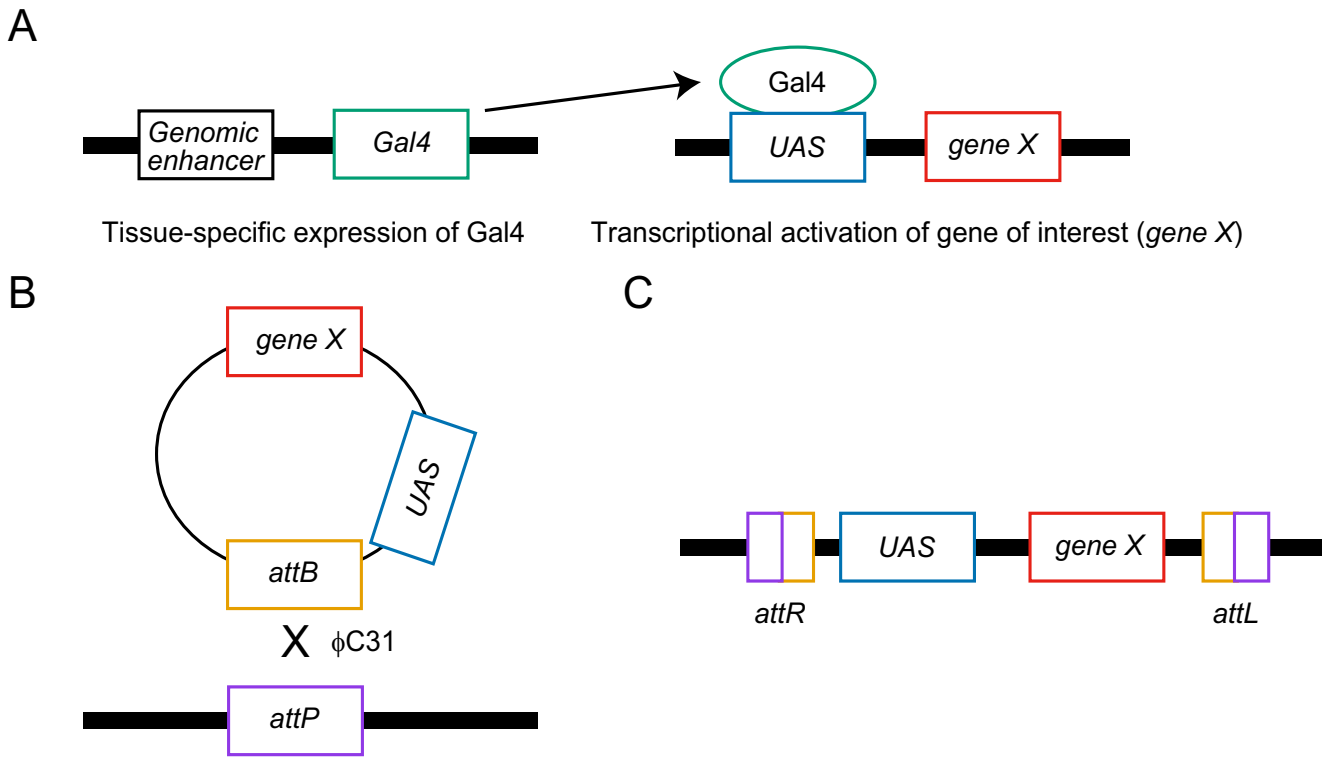

Figure 6: The Gal4/UAS binary expression system
(A) Schematic of the Gal4/UAS system. The genomic enhancer enables tissue-specific expression of a transcription factor Gal4. Gal4 binds to the *UAS* sequence and induces the expression of a target gene X.
(B) Schematic of site-specific insertion. *UAS-gene X* plasmid is integrated into the *attP* site by a ϕC31 integrase.
(C) Site-specific integration between the *attB* and *attP* sequences encompasses *UAS-gene X* plasmid. Formation of *attR* and *attL* sequences terminates the activity of the ϕC31 integrase.

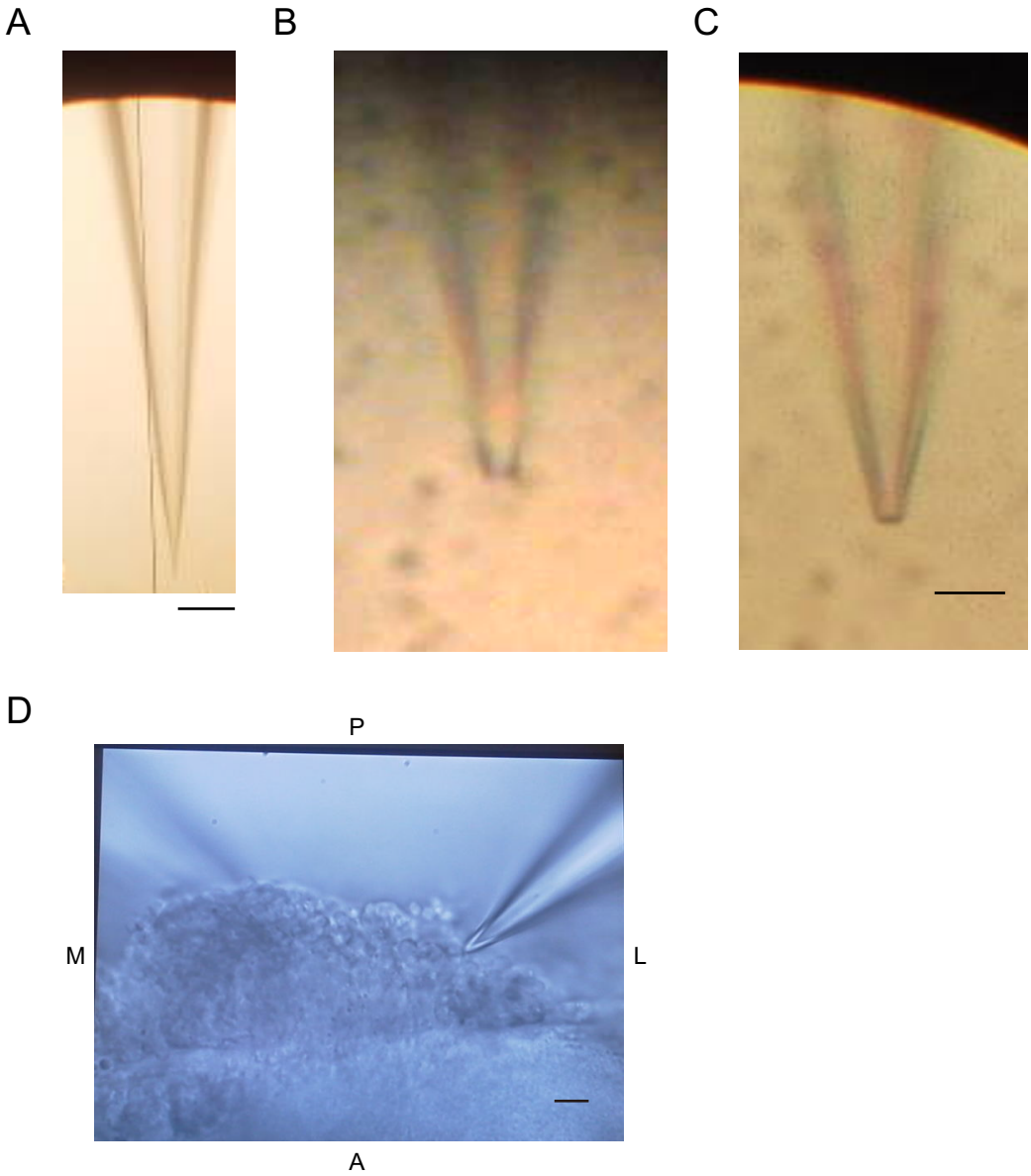

Figure 7: Patch pipette used for KC recordings
(A) Picture of a patch pipette used for whole-cell recordings from KCs. Scale bar, 50 μm.
(B) A patch pipette before pressure polishing.
(C) The same patch pipette in (B) after pressure polishing. Pressure polishing makes the tip of the pipette smaller, thickens the glass wall around the tip, and increases the angle cone. Scale bar, 5 μm.
(D) A patch pipette targeting a KC. Scale bar, 5 μm. A, anterior, P, posterior, L, lateral, M, medial.

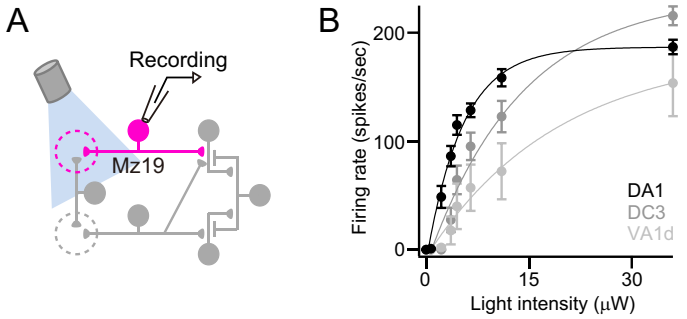

Figure 8: Response of *Mz19-Gal4*-positive PNs to blue LED
(A) Schematic of an experiment.
(B) Relationship between *Mz19-Gal4*-positive PN firing rate and LED light intensity in *Mz19-Gal4>ReaChR* flies (n = 11, 4, 4 for DA1, DC3 and VA1d PNs, respectively). Firing rate was calculated in 50-ms bins overlapped by 25 ms and averaged across the illumination period (1 s).

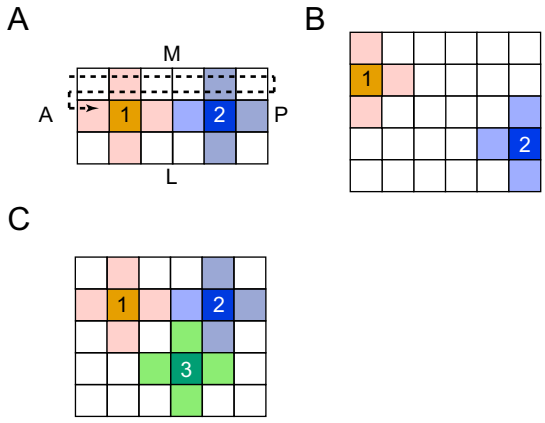

Figure 9: Example of IR stimulation patterns
(A-C) Examples of stimulation patterns used to examine the integration of inputs from two (A and B) or three (C) ROIs in KCs. See Materials and Methods for the criteria for selecting the ROIs. A, anterior, P, posterior, L, lateral, M, medial. Arrow indicates the scan direction. Scan speed along A-P axis is shorter than that for M-L axis.

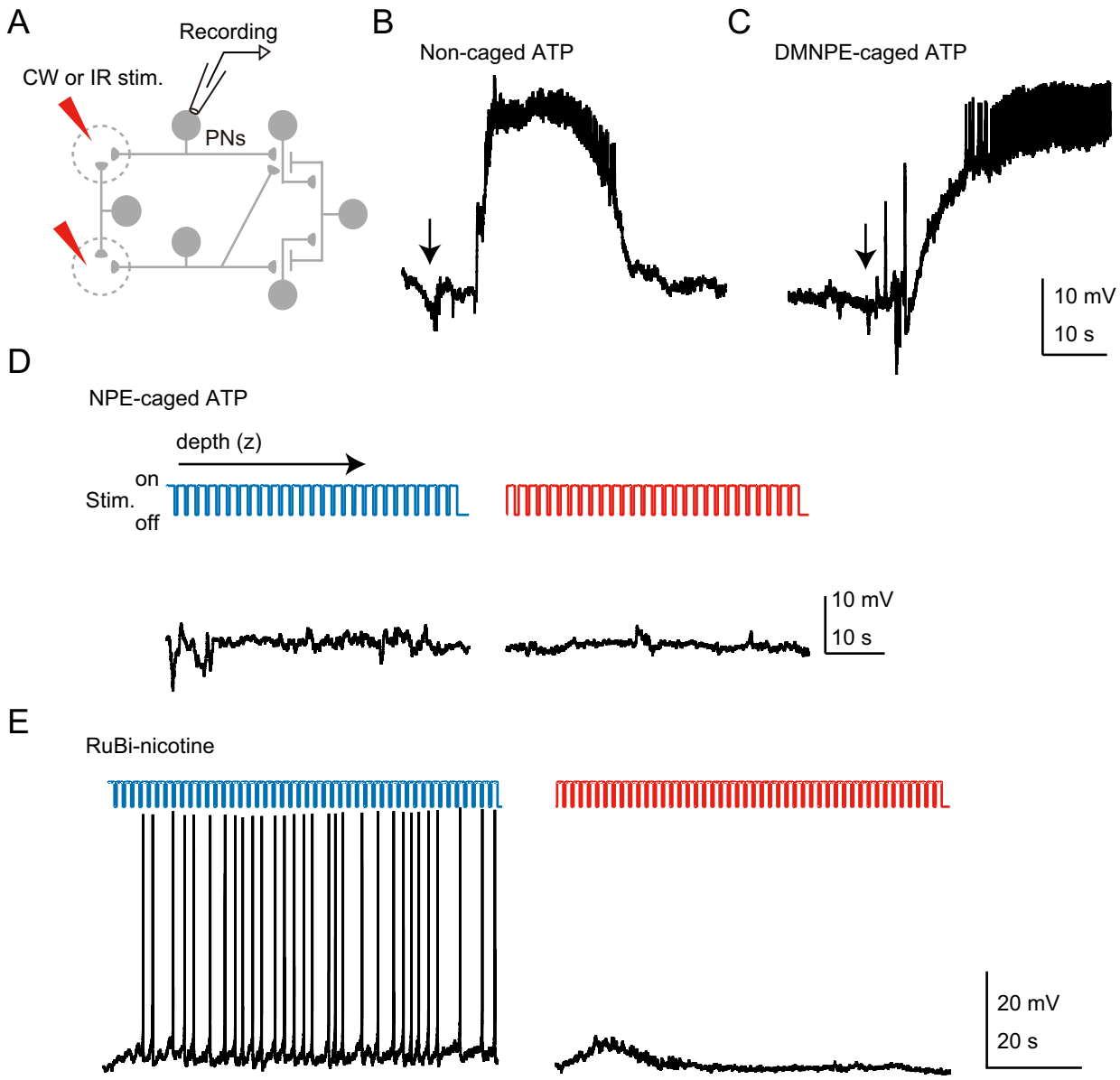

Figure 10: PN responses to caged compounds
(A) Schematic of an experiment. The brain was incubated by the external solution containing caged compounds.
(B) Sample response of a PN expressing $P2X_2$. The PN spiked in response to non-caged ATP stimulation (1 mM). Arrow indicates the timing of ATP application.
(C) Sample response of a PN expressing $P2X_2$. DMNPE-caged ATP (13 mM) evoked spontaneous spikes in PNs without an optical stimulation. DMNPE-caged ATP was incubated in the apyrase prior to the experiment. Arrow indicates the timing of application of DMNPE-caged ATP.
(D) Sample PN responses to NPE-caged ATP (1 mM) under the blue laser stimulation (left) or IR laser stimulation (right). Neither blue laser nor IR laser evoked depolarization reliably in a PN.
(E) Sample PN responses to RuBi-nicotine (1 mM). Blue laser (left) evoked action potentials in a PN, whereas IR laser generated negligible amount of depolarization (right).

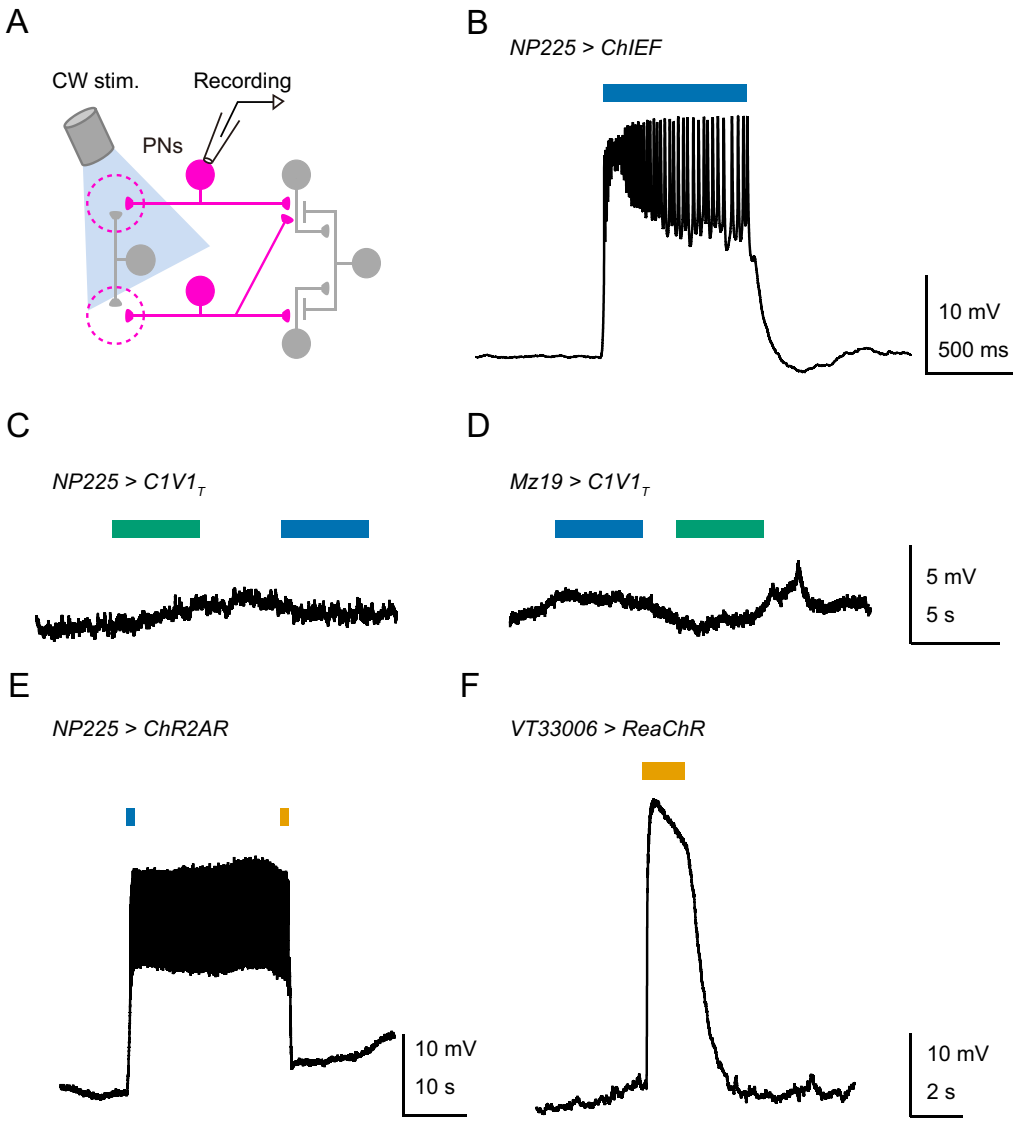

Figure 11: Responses of PNs expressing various optogenetic probes to CW stimulation
(A) Schematic of an experiment. PNs expressing an optogenetic probe were stimulated by filtered light from a mercury lamp.
(B) Sample response of a PN expressing ChIEF.
(C) Sample response of a PN expressing $C1V1_T$ driven by *NP225-Gal4*. Neither blue nor green light evoked a response.
(D) Sample response of a PN expressing $C1V1_T$ driven by *Mz19-Gal4*. Regardless of the Gal4 driver, $C1V1_T$ did not depolarize PNs.
(E) Sample response of a PN expressing ChR2AR. Blue light evoked spikes in the PN by opening the optogenetic channel and amber light decreased the membrane potential to a resting potential by closing the channel.
(F) Sample response of a PN expressing ReaChR. Amber light depolarized the PN strongly. Note that the PN spiked at a high rate.

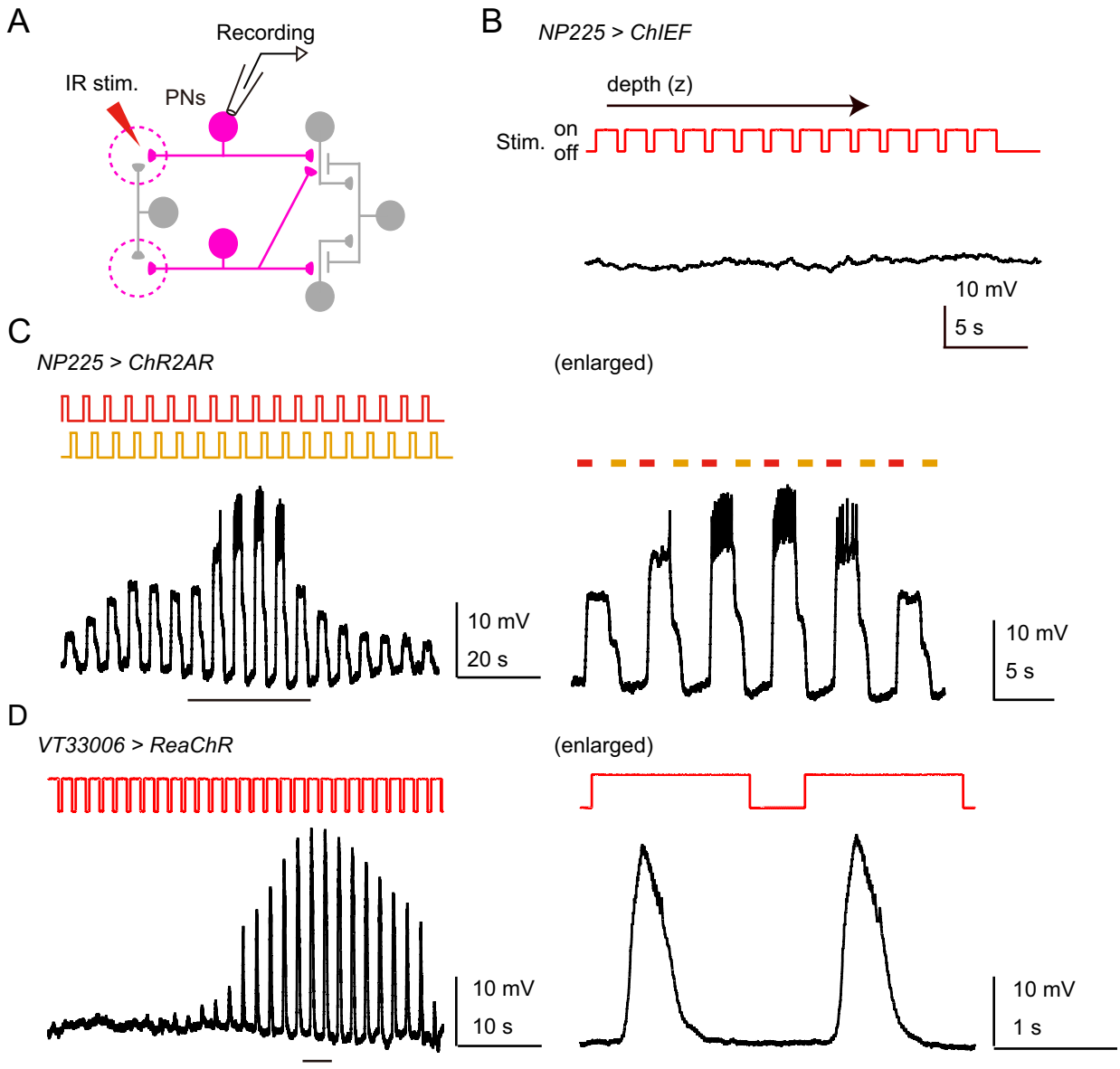

Figure 12: Responses of PNs expressing various optogenetic probes to IR stimulation
(A) Schematic of an experiment.
(B) Sample response of a PN expressing ChIEF. The PN did not show depolarization in response to IR stimulation. Optical sectioning stimulated different z-frames from dorsal to ventral.
(C) Left, sample response of a PN expressing ChR2AR. ChR2AR was opened by an IR laser and closed by an amber laser (594 nm). The PN spiked at restricted z-frames. Right, expansion of a response indicated by the black bar.
(D) Left, sample response of a PN expressing ReaChR. The PN showed spikes at restricted z-frames. The ReaChR-evoked firing rate was higher than the ChR2AR-evoked firing rate. Right, expansion of a response indicated by the black bar.

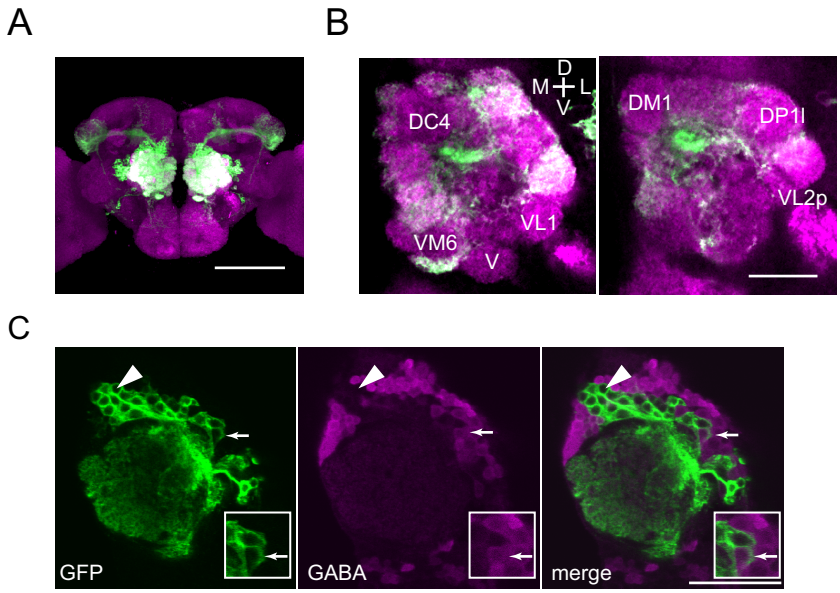

Figure 13: Identification of *VT33006-Gal4*
(A) Projection of a confocal stack of a fly brain (neuropil in magenta) expressing myr::GFP (green) driven by *VT33006-Gal4*. *VT33006-Gal4* labels 44 antennal lobe glomeruli. Scale bar, 100 μm. See Table 1 for the identity of labeled glomeruli.
(B) Confocal images of the immunostained antennal lobe taken at different planes along the anterior-posterior axis. Magenta, nc82 (neuropil), green, anti-GFP. *VT33006-Gal4* labels $\sim$44 antennal lobe glomeruli. The identities of Gal4-negative glomeruli are indicated in white. D, dorsal, V, ventral, L, lateral, M, medial. Scale bar, 20 μm.
(C) Immunostaining against GABA (magenta). Scale bar, 50 μm. Most of the *VT33006-Gal4*-positive cells are immunonegative for GABA (arrowhead) and only a small number of them are immunopositive (arrow, inset; 9.7 $\pm$ 1.7 cells per hemisphere, n = 3 flies). Furthermore, this Gal4 line labels the medial antennal lobe tract strongly (data not shown). These results together suggest that most of the *VT33006-Gal4*-positive cells are PNs.

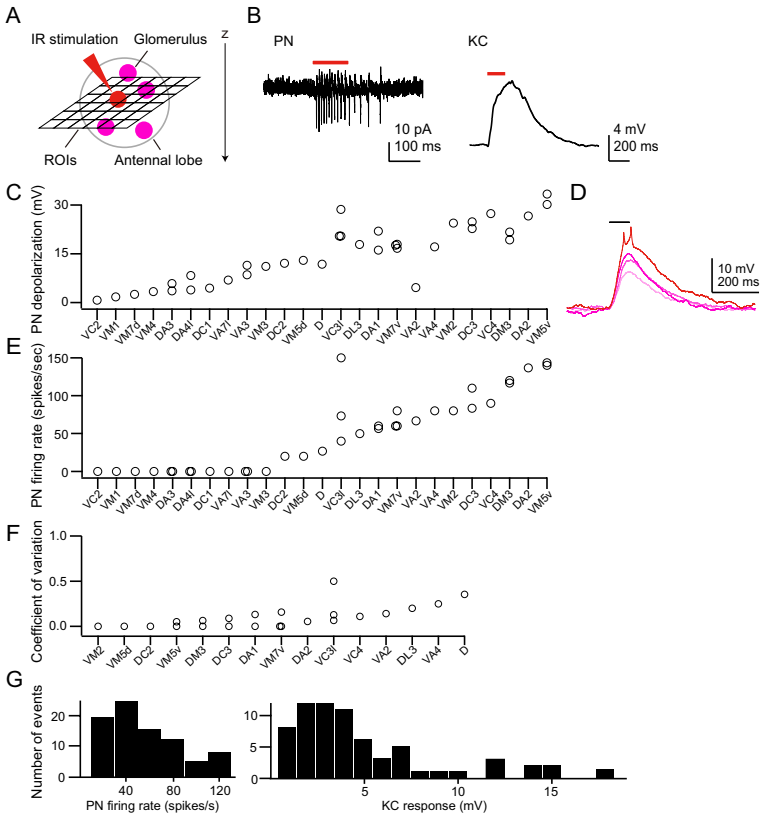

Figure 14: PN/KC response to IR stimulation

(A) Schematic of the experiment. ReaChR driven by *VT33006-Gal4* was stimulated by a pulsed infrared (IR) laser. A horizontal plane covering the entire antennal lobe was divided into 6 $\times$ 6 ROIs and the IR light was sequentially applied to individual ROIs one at a time. The size of each ROI is 12 μm $\times$ 12 μm. The antennal lobe was optically sectioned at 5 μm intervals along the z-axis.

(B) Left, sample cell-attached recording of PN spikes in response to IR stimulation (red). Right, sample whole-cell recording of a KC response to the same stimulus.

(C) Peak depolarization in ReaChR-expressing PNs upon two-photon excitation of single ROIs. Depolarization was observed in all the 25 *VT33006-Gal4*-positive glomeruli tested (n = 36 PNs). Each dot corresponds to data from a single PN.

(D) Stimulation with stronger laser power made PNs spike (example responses in glomerulus VM3, stimulation at 8, 10, 11, and 14 mW). Black bar, IR stimulation.

(E) Spikes were evoked in 15 out of 25 *VT33006-Gal4*-positive glomeruli tested (60%, n = 36 PNs) in response to IR stimulation at the laser power employed for examining the integration of multiple synaptic inputs in KCs. Each dot corresponds to data from a single PN.

(F) Coefficient of variation was calculated from data shown in (E) to quantify the trial-to-trial variability of PN spiking responses. Low coefficient of variation in most of the glomeruli indicates that IR stimulation drives PNs reliably.

(G) Histograms of the PN spiking response (left) and the KC response (right) evoked by single ROI stimulation. Firing rate was calculated in 50-ms bins overlapped by 25 ms. Values are peak activity during IR stimulation. n = 81 ROIs from 11 PNs and 67 ROIs from 9 KCs.

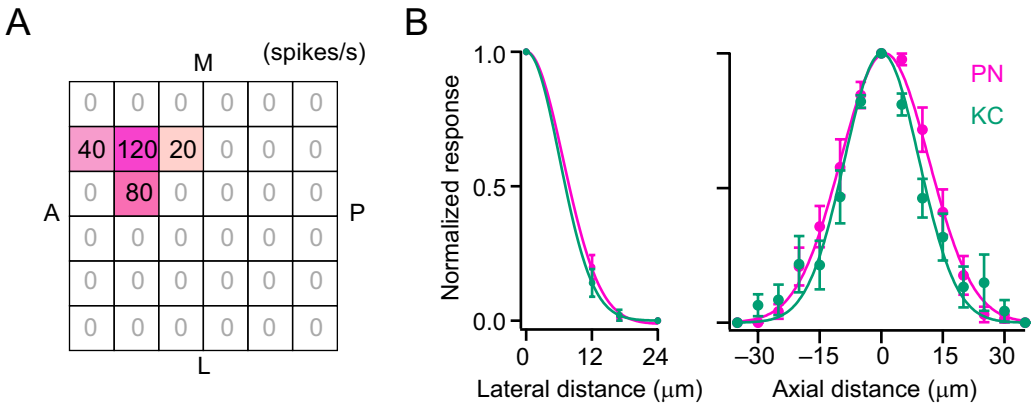

Figure 15: Spatial resolution of PN/KC response to IR stimulation
(A) Sample PN activity evoked by IR stimulation of each ROI. A, anterior, P, posterior, L, lateral, M, medial.
(B) Relationship between normalized PN responses and the lateral (x- and y- axes) distance (left) or the axial (z-axis) distance (right) from the most effective ROI. Solid lines are Gaussian fits. A positive axial distance corresponds to a dorsal shift. For the lateral distance, the full width at half maximum is 15.8 μm for PNs and 14.2 μm for KCs. For the axial distance, the full width at half maximum is 25.7 μm for PNs and 19.4 μm for KCs. n = 11 PNs and 9 KCs. The chance of simultaneously stimulating two neighboring glomeruli presynaptic to our set of recorded KCs was likely low, because both lateral and axial resolutions of KC responses matched with those of PN spikes. If multiple PNs in neighboring glomeruli were activated by the stimulation of each ROI, the resolution of KC responses would have been much worse than that of PN spikes.

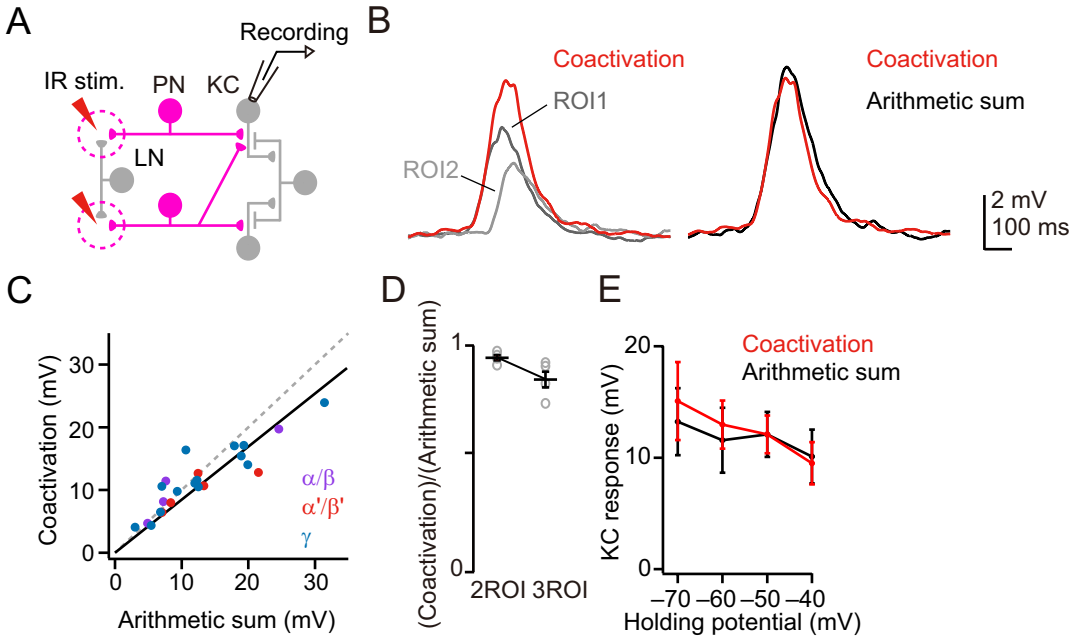

Figure 16: KCs add inputs from multiple PNs linearly
(A) Schematic of the synaptic integration experiment.
(B) Representative KC responses to optogenetic activation of single ROIs (gray traces) and coactivation of these ROIs (red). Black is an arithmetic sum of single ROI responses. Each trace is an average of three trials. Short time difference between individual KC responses reflects the time for the laser to travel from the first to the second ROI (see Figure 9).
(C) All KC types integrate inputs from multiple PNs approximately linearly (slope = 0.89, 0.75, 0.86 for α/β, α'/β', and γ KCs, respectively, n = 4, 5, 15 for α/β, α'/β', and γ KCs, respectively). Black line is a linear fit for all KCs (slope = 0.85, R^2 = 0.81, $p < 10^{-7}$).
(D) KCs add inputs from up to three ROIs approximately linearly (pairwise data, n = 4 KCs).
(E) Response to coactivation of ROIs is not significantly different from the arithmetic sum of single ROI responses at all tested holding potentials (spikes were removed by low-pass filtering at 13 Hz, n = 5 KCs, p = 0.50, two-way ANOVA with repeated measurements).

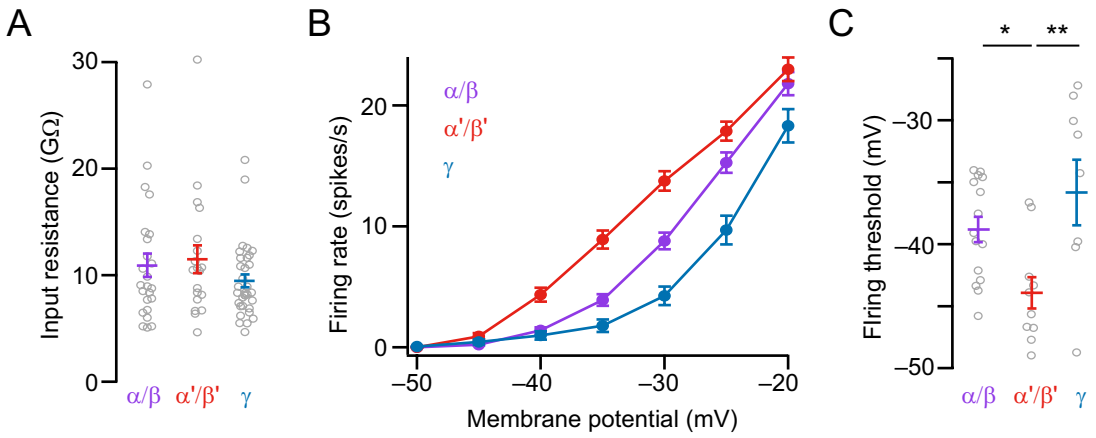

Figure 17: α'/β' KCs are intrinsically the most excitable
(A) Input resistance measured at soma is not significantly different between cell types (n = 24, 19, 33 for α/β, α'/β', and γ KCs, respectively. p = 0.30, one-way ANOVA).
(B) Relationship between the KC membrane potential and the firing rate. Membrane potential changes were elicited by injecting currents into the KC soma, and the mean firing rate was measured for each level of depolarization. The rank order of excitability is α'/β' to α/β to γ. n = 15, 10, 7 for α/β, α'/β', and γ KCs, respectively.
(C) α'/β' KCs have the lowest firing threshold (n = 15, 10, 8 for α/β, α'/β', and γ KCs, respectively. $\star$p < 0.05, $\star\star$p < 0.01, one-way ANOVA with post-hoc Tukey HSD).

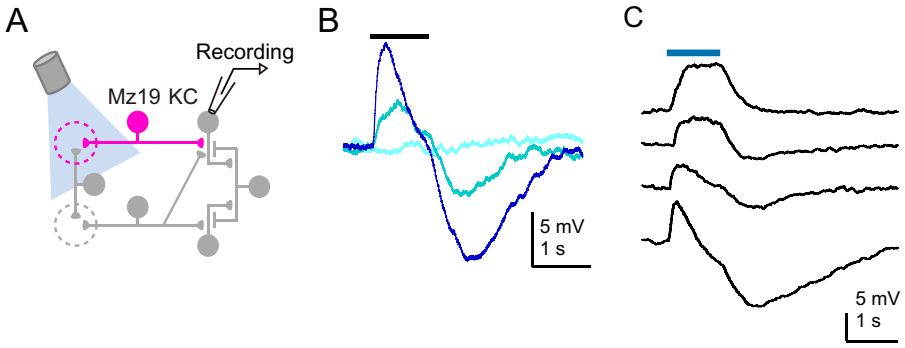

Figure 18: KC response is determined by both excitatory and inhibitory inputs
(A) Schematic of an experiment. *Mz19-Gal4*-positive PNs expressing ReaChR were stimulated with LED light. Recordings were made from KCs connected to *Mz19-Gal4*-positive PNs.
(B) Sample recording of KC responses to light at three different intensities (0.7, 1.9, and 11 μW). Stronger stimulation recruited stronger excitation and offset inhibition. Each trace is an average of three trials.
(C) Responses of four different KCs to light in *Mz19-Gal4>ReaChR* flies (6.5 μW). Blue bar, light stimulation. Each trace is an average of three trials.

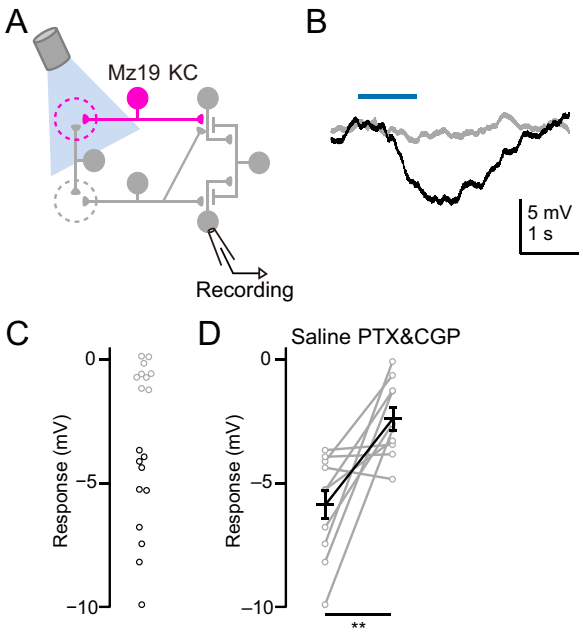

Figure 19: Local, lateral inhibition is mediated via GABA signaling
(A) Schematic of an experiment. *Mz19-Gal4*-positive PNs expressing ReaChR were stimulated with LED light. Recordings were made from KCs that were not connected with *Mz19-Gal4*-positive PNs.
(B) Responses of two KCs to light stimulation. Both are α'/β' KCs. Light intensity is 6.5 μW. Blue bar, light stimulation. Each trace is an average of three trials.
(C) KCs were classified by unsupervised (k-means) clustering into two groups that did (black) or did not (gray) receive inhibition (n = 19 KCs). Offset responses were measured at 500 ms after the removal of light.
(D) Inhibitory offset responses were significantly suppressed by GABA receptor antagonists ($\star\star p < 0.01$, paired t-test, n = 10).

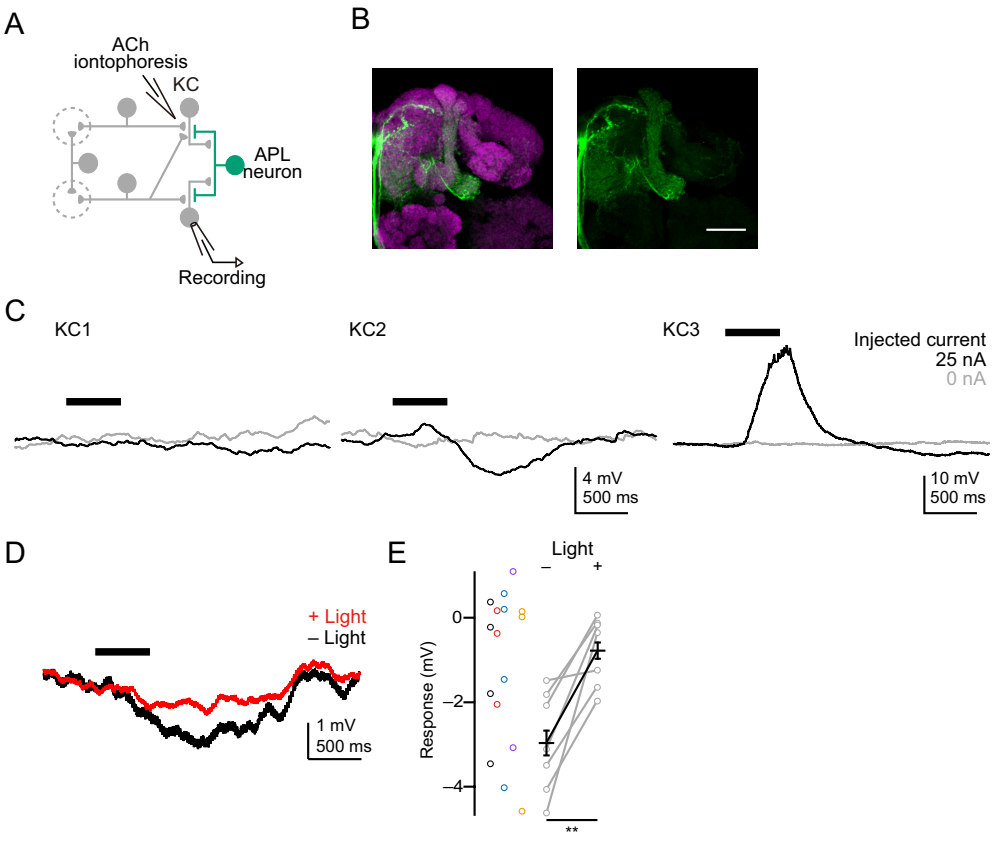

Figure 20: Local, lateral inhibition is mediated via APL neurons
(A) Schematic of an experiment. KCs were activated by iontophoresis of acetylcholine (ACh) into the mushroom body calyx. Archaerhodopsin (Arch) was expressed in APL neurons. To ensure that the recruited inhibition is local, at least two KCs were recorded from the same brain, and the current amplitude that evoked inhibition in a fraction of KCs was used for stimulation.
(B) Left, projection of a confocal stack of a fly brain (neuropil in magenta) expressing myr::GFP (green) driven by *APL-Gal4*. Scale bar, 20 μm. Although GFP signals are found in neurons innervating the superior medial protocerebrum and the crepine (cell bodies are anterior to the spur), importantly, the Gal4 driver does not label cells other than APL neurons in the mushroom body (Wu et al., 2013). Right, GFP channel.
(C) Representative KC responses from the same brain to iontophoresis of ACh into the mushroom body calyx. To ensure that the induced inhibition remains local (KC2), we confirmed that some KCs (KC1) in the same brain showed no response under the identical iontophoresis condition. Some KCs under the direct influence of injected ACh showed excitation (KC3). Black bar, current injection.
(D) Representative KC responses to ACh iontophoresis in the calyx in a fly expressing Arch in APL neurons with (red) or without (black) optical stimulation. Each trace is an average of three trials. Light was applied continuously throughout the response period. Black bar, current injection for ACh iontophoresis (500 ms). Optical suppression of APL neuron decreases the amount of inhibition evoked by ACh iontophoresis.
(E) KC responses to iontophoresis. Data obtained from the same brain are plotted in the same color (n = 16 KCs from 5 brains). Offset responses were measured 300 ms after the removal of the current. Light activation of Arch significantly decreased the inhibitory offset response ($\star\star p < 0.01$, paired t-test, n = 7 KCs from 5 brains). Light was applied continuously throughout the response period.

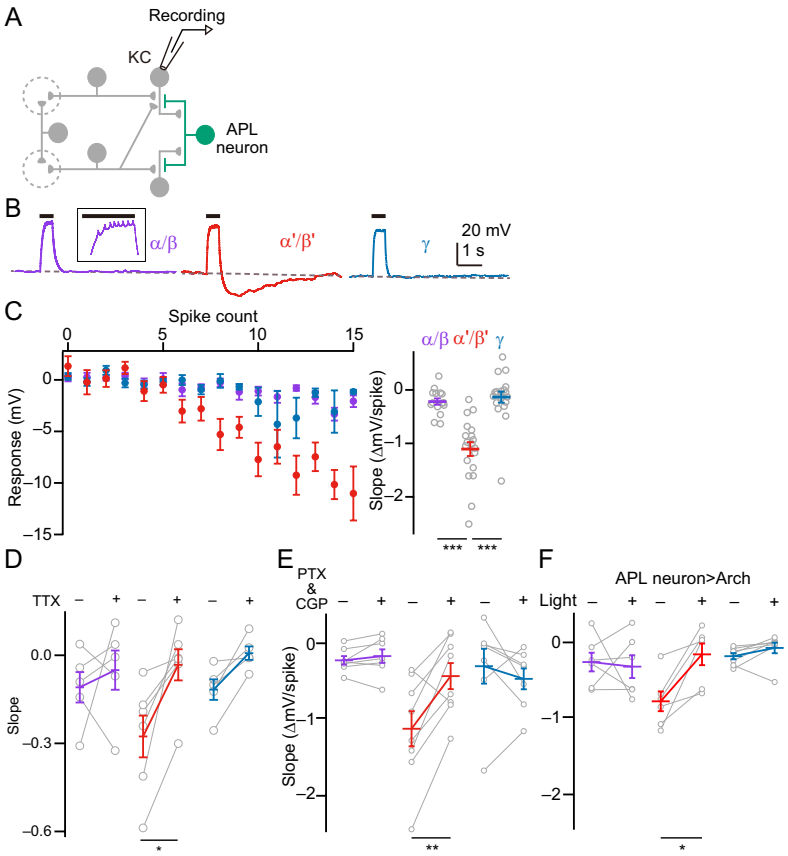

Figure 21: KC-type-specific recruitment of GABAergic inhibition via APL neurons
(A) Schematic of an experiment.
(B) Typical KC traces showing a cell-type-specific inhibitory offset response following spikes. Spikes were evoked in KCs (inset) by injecting a current into the soma for 500 ms (black bar). α'/β' KCs show a stronger inhibitory offset response compared to the other two cell types. Dotted line indicates the resting potential.
(C) Left, relationship between the KC spike count in 500 ms and the offset response measured 500 ms after the end of current injection (5-40 pA). Right, the slope of a line fit separately to data from each KC types within the linear range (3 to 15 spikes). The slope for α'/β' KCs is significantly steeper than that for the other two cell types ($\star\star\star p < 0.001$, one-way ANOVA with post-hoc Tukey HSD. n = 15, 19, 19 for α'/β' to α/β to γ KCs, respectively).
(D) Relationship between the mean KC membrane potential during current injection and the offset response measured 500 ms after the end of current injection. n = 5, 6, 5 for α/β, α'/β', and γ KCs, respectively. The slope for α'/β' KCs was significantly decreased by the addition of tetrodotoxin (TTX; $\star p < 0.05$, paired t-test with Bonferroni correction). The slope for α'/β' KCs after application of tetrodotoxin was not significantly different from zero ($p > 0.60$, t-test).
(E) The slope for α'/β' KCs was significantly decreased by GABA receptor antagonists ($\star\star$p ¡ 0.01, paired t-test with Bonferroni correction. n = 7, 8, 7 for α/β, α'/β', and γ KCs, respectively).
(F) Light activation of Arch expressed in APL neurons significantly decreased the slope for α'/β' KCs (*p ¡ 0.05, paired t-test with Bonferroni correction. n = 6, 6, 7 for α/β, α'/β', and γ KCs, respectively).

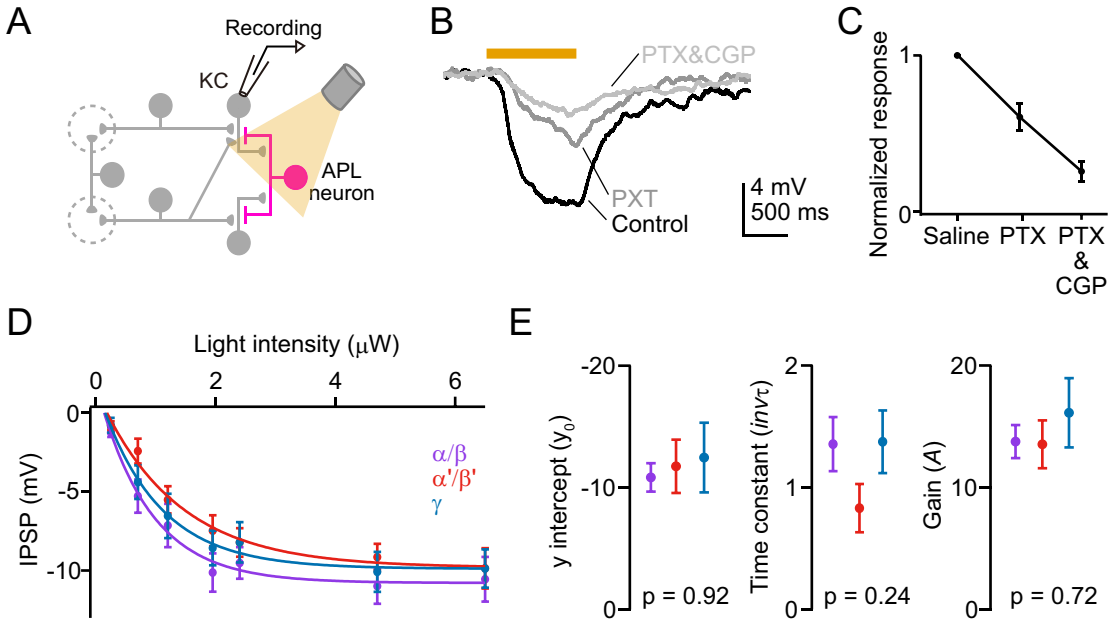

Figure 22: Optogenetic activation of APL neurons inhibit all types of KCs with a similar strength
(A) Schematic of an experiment. CsChrimson expressed in APL neurons was activated with amber LED light.
(B) KC responses to optogenetic activation of APL neurons with or without the presence of GABA receptor antagonists. Each trace is an average of three trials.
(C) KCs receive inhibition from APL neurons through both $GABA_A$ and $GABA_B$ receptors (n = 10 KCs).
(D) Optogenetic activation of APL neurons at various light intensities (n = 5, 8, 9 for α/β, α'/β', and γ KCs, respectively). The smooth lines are fit to the data with an exponential function

$$f(\text{Light intensity}) = y_0 + A\exp\{-inv\tau \cdot (\text{Light intensity})\}.$$

(E) Three parameters that determine the shape of the exponential fit in (D) are not significantly different between cell types. p-values are shown in each panel (one-way ANOVA).

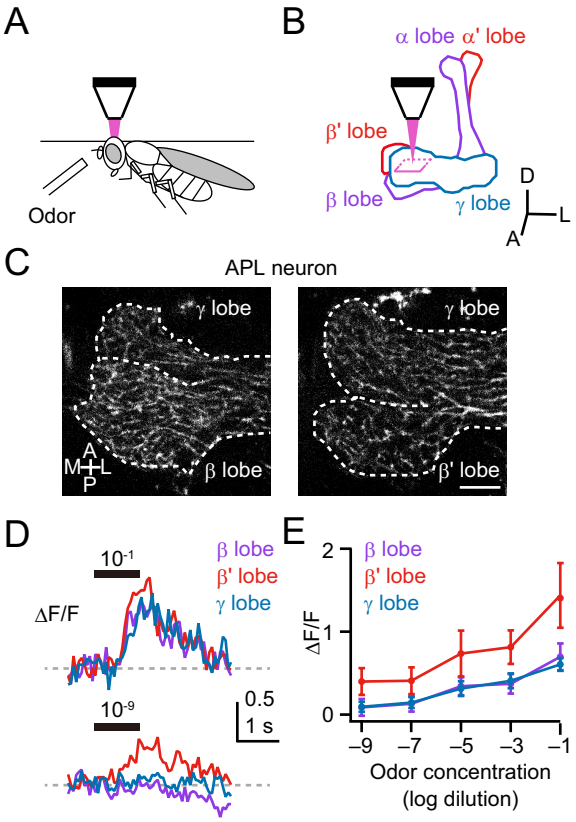

Figure 23: The spatial extent of calcium responses in APL neuron shifts from lobe-specific to global with increasing olfactory input to the mushroom body

(A) Schematic of an experiment. Odor responses of APL neurons were recorded with calcium imaging. GCaMP6s was expressed in APL neurons with *VT43924-Gal4*.

(B) GCaMP signals were recorded from three medial lobes. A, anterior, D, dorsal, L, lateral.

(C) Baseline signal of GCaMP6s. The dotted lines indicate the boundaries of different medial lobes. Odor responses were recorded at the tip of the lobes where different lobes can be clearly segregated. Dorsal view. Scale bar, 10 μm. A, anterior, P, posterior, L, lateral, M, medial.

(D) Sample recording (mean ΔF/F in 16.64 μm $\times$ 16.64 μm ROI averaged across four trials) from three lobes in response to ethyl butyrate at 10^{-1} (top) or 10^{-9} (bottom) dilution. Black bar, odor application (1 s).

(E) Responses of APL neuron in three lobes to ethyl butyrate at various concentrations. Neurites in the β' lobe showed substantially larger responses as compared to those in the other two lobes ($p < 0.001$, two-way ANOVA with repeated measurements. β vs β' and β' vs γ, $p < 0.001$, post-hoc Tukey HSD. n = 6 flies).

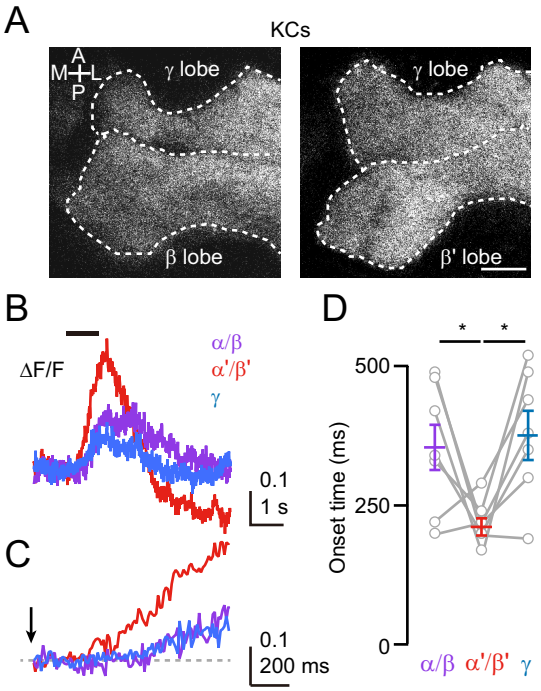

Figure 24: α'/β' KCs respond to odors with shorter latency
(A) Baseline signal of GCaMP5 expressed in all KCs with *OK107-Gal4.* The dotted lines indicate the boundaries of different medial lobes. Signals were imaged and analyzed as in Figure 23. Dorsal view. Scale bar, 10 μm. A, anterior, P, posterior, L, lateral, M, medial.
(B) Sample recording from three types of KCs in response to ethyl butyrate (10^{-1} dilution). Black bar, odor application (1 s). Each trace is an average of ten trials.
(C) Enlarged view of calcium responses during odor application period shown in (B). Arrow indicates the onset of the odor.
(D) Onset time of GCaMP signals. α'/β' KCs start to respond earlier than the other two cell types ($\star p < 0.05$, one-way ANOVA with post-hoc Tukey HSD. n = 7 flies).

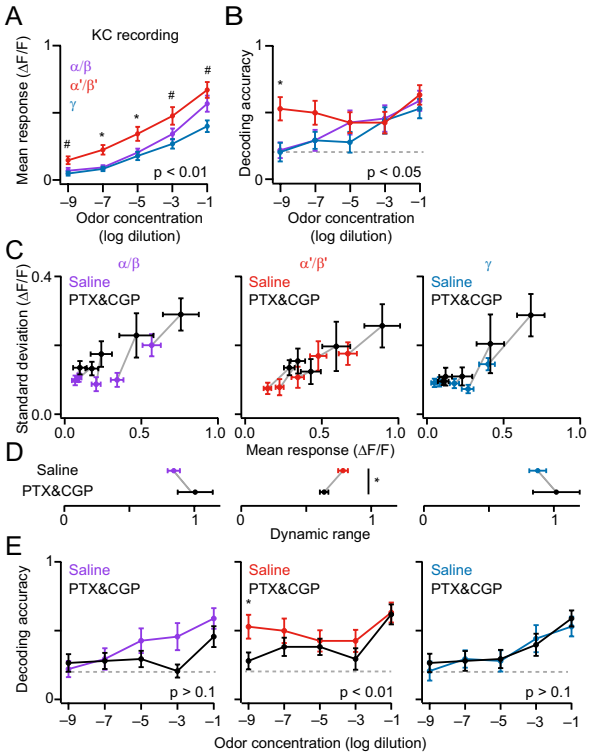

Figure 25: Higher sensitivity of α'/β' KCs and cell-type-specific inhibition enhances discrimination between different odor concentrations

(A) Activity of KCs recorded in medial lobes in response to various concentrations of ethyl butyrate. The same genotype as in Figure 24. α'/β' KCs respond more strongly than the other two cell types. p-value of two-way ANOVA with repeated measurements (difference between cell types) is shown in the panel. Asterisks ($\star$) denote significant differences ($p < 0.05$, Tukey HSD) for α/β vs α'/β' and for α'/β' vs γ, hashes (#) denote significant differences for α'/β' vs γ. n = 17 flies (same flies across all the panels in Figure 25).

(B) Accuracy of decoding odor concentrations using linear discriminant analysis. The dotted line indicates chance performance. Accuracy was significantly different between cell types. p-value (difference between cell types) is shown in the panel (two-way ANOVA with repeated measurements. $\star p < 0.05$, α'/β' vs γ, Tukey HSD).

(C) Application of GABA receptor antagonists increases both response amplitude (mean ΔF/F) and trial-to-trial variability (standard deviation) in all cell types (mean and standard deviation were calculated from responses to the same stimuli in four trials; $p < 0.05$, two-way ANOVA with repeated measurements, saline vs PTX & CGP). Gray line connects responses to the same concentration of odor.

(D) GABA receptor antagonists narrow the dynamic range, defined as the difference in normalized responses to 10^{-1} and 10^{-9} dilutions (see Materials and Methods) in α'/β' KCs ($\star p < 0.05$, paired t-test with Bonferroni correction).

(E) Application of GABA receptor antagonists decreases the performance of decoding in α'/β' KCs. p-values are shown in each panel (two-way ANOVA with repeated measurements, saline vs PTX & CGP. $\star p < 0.05$, Tukey HSD). The dotted line indicates chance performance.

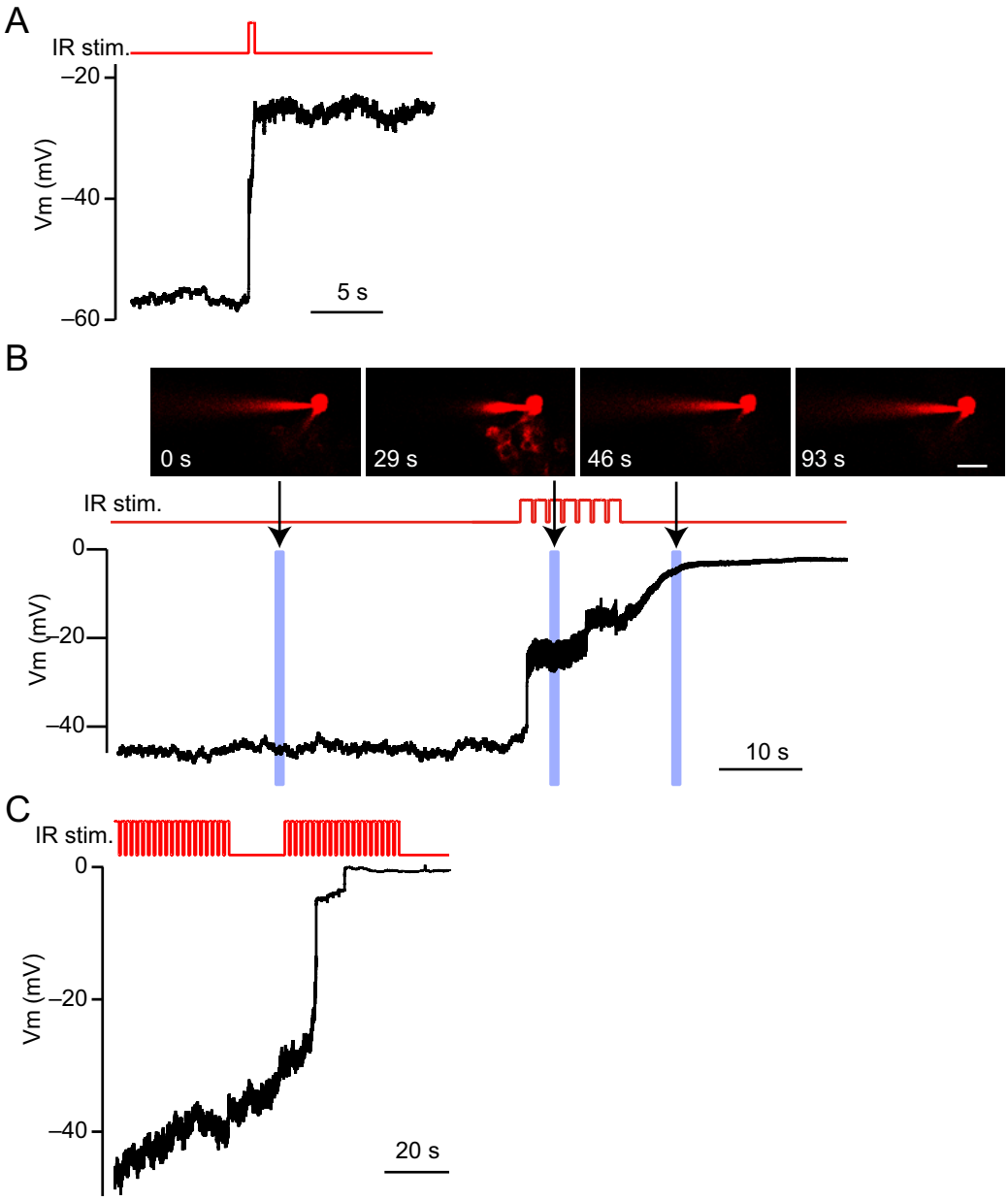

Figure 26: Strong IR stimulation increases the PN membrane potential rapidly and irreversibly
(A) Typical PN response to relatively strong intensity ($\sim$25 mW) of IR (700 nm). The membrane potential of a PN kept at around the resting potential (~ -60 mV) increased rapidly by the IR stimulation.
(B) Relatively strong intensity of IR stimulation was applied, while imaging the dye injected into a PN cell body, to examine whether the dye escapes out from the neurites or the soma. I did not detect the leak of the dye, even after the membrane potential reached $\sim$0 mV. Scale bar, 10 μm.
(C) Sample response of a PN incubated with astaxanthin. IR stimulation still increased the membrane potential.

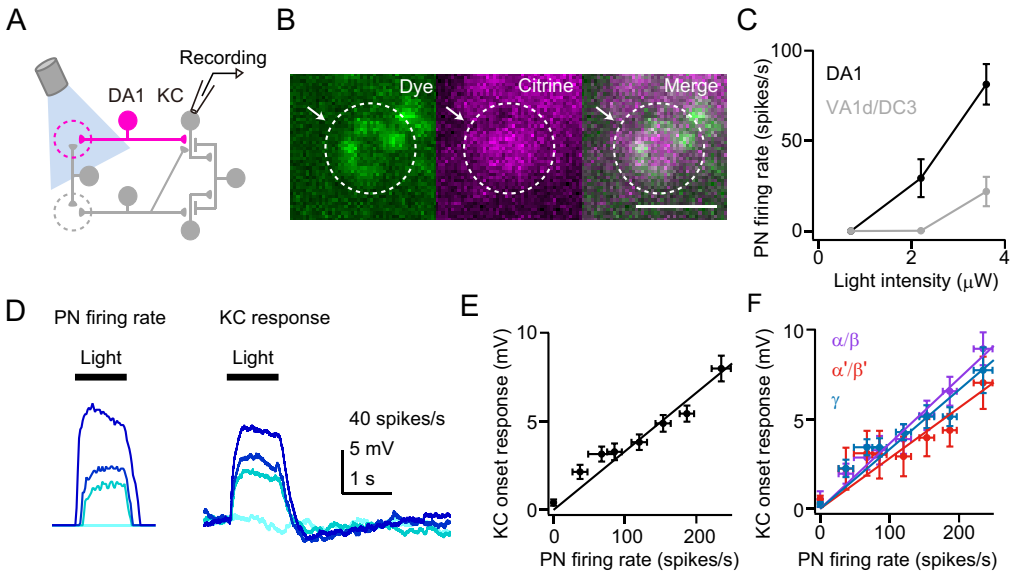

Figure 27: PN-to-KC transfer function created based on responses to LED stimulation
(A) Schematic of the experiment. ReaChR was expressed in a subset of PNs with *Mz19-Gal4* and stimulated by blue light from LED. Whole-cell recordings were performed from KCs connected with a single *Mz19-Gal4*-positive PN innervating glomerulus DA1.
(B) Raw image of a KC claw filled with dye through a patch pipette (green) contacting a single PN bouton expressing Citrine (magenta). Scale bar, 2 μm.
(C) Relationship between LED light intensity and DA1- or VA1d/DC3-PN firing rate (n = 11, 4, 4 for DA1, VA1d and DC3 PNs, respectively). At 2.2 μW, DA1-PNs generated substantial number of spikes (37.1 $\pm$ 10.4 spikes/s), whereas VA1d/DC3-PNs almost did not respond at all (0.34 $\pm$ 0.32 spikes/s). This clear difference in light sensitivity was used to distinguish DA1-PN-connecting KCs from VA1d/DC3-PN-connecting KCs.
(D) Example PN and KC responses to blue light with different intensities. Each trace is an average of five trials. Black bar, light stimulation.
(E) Responses of four different KCs to light applied at the highest intensity used in (D) (6.5 μW). Blue bar, light stimulation.
(F) Relationship between the PN firing rate and the KC response shortly (200 ms) after the onset of light stimulation (n = 11 PNs and 21 KCs, R^2 = 0.96, p = 0.0018).
(G) Relationship between the KC onset response and the PN firing rate as in (F), but for each type of KCs (n = 7, 5, 9 for α/β, α'/β', and γ KCs, respectively).

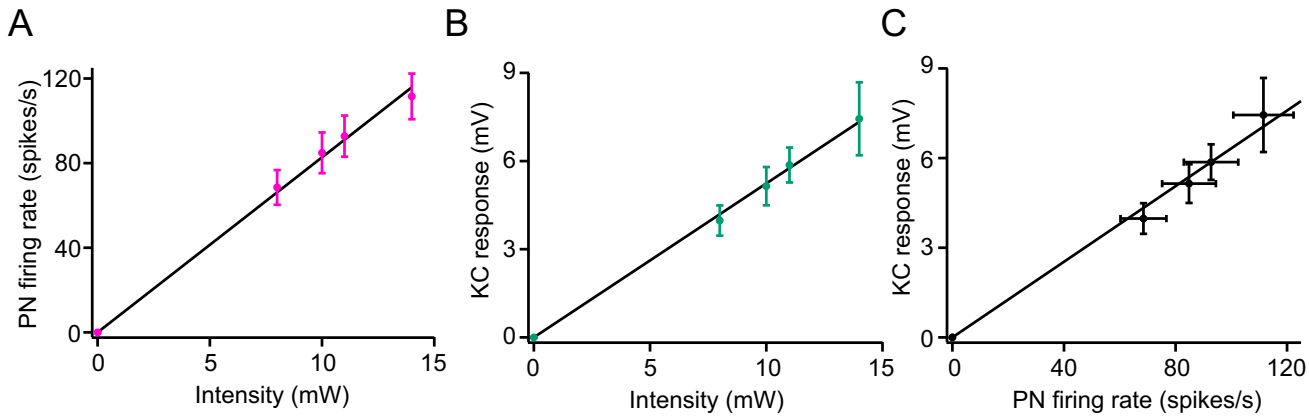

Figure 28: PN-to-KC transfer function created based on responses to IR stimulation
Peak PN firing rate (A) or KC response (B) to the single ROI stimulation with various intensity of IR. (A) and (B) are merged in (C). n = 6 KCs and 11 PNs from 8 glomeruli. $R^2 = 0.94$, $p < 0.05$.

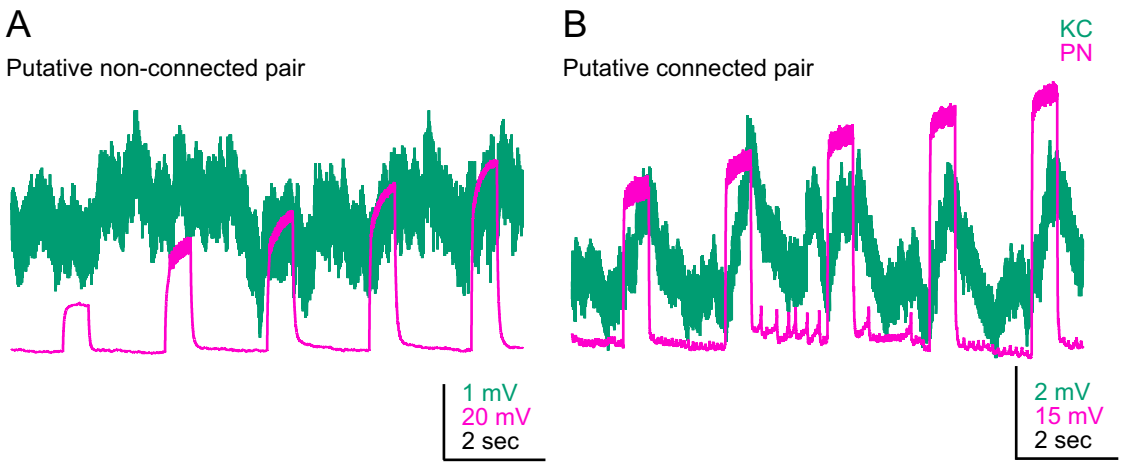

Figure 29: Dual whole-cell recordings from PN-KC pairs
Sample traces from a KC and two PNs either putative non-connected (A) and connected (B). PN spikes were evoked by injecting a current into the cell body. Depolarization of the KC correlates with PN firing in (B), whereas it does not in (A).

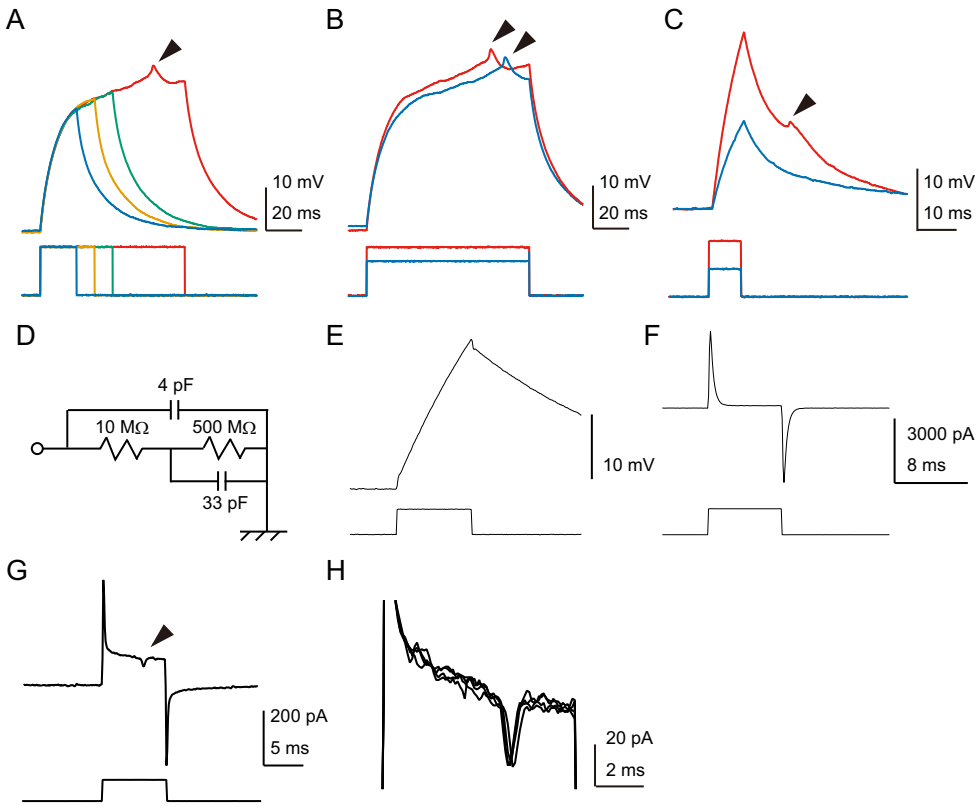

Figure 30: Induction of single action potentials by current injection into the PN cell body
(A) Sample PN responses to a current injection (70 pA) into the cell body for various amount of time: 20 ms (blue), 30 ms (amber), 40 ms (green), and 80 ms (red). Arrowhead indicates an action potential. An action potential appeared ∼60 ms after the onset of the current injection. 20-40 ms current pulses failed to generate action potentials.
(B) Sample PN responses to an 80 ms current injection with different amplitudes: 60 pA (blue) and 70 pA (red). Arrowheads indicate action potentials. Larger current amplitude shortens the latency to spike.
(C) Sample PN responses to 8 ms current injection. Current amplitudes are 50 pA (blue) or 90 pA (red). Arrowhead indicates an action potential. Even when larger current was applied, spikes appeared with latency of ∼20 ms. Note that current amplitude larger than 100 pA damages PNs, limiting the range of current amplitude that can be applied.
(D) An electrical circuit mimicking the whole-cell configuration. Voltage-clamp recording or current-clamp recording was performed with the circuit to test the influence of electrical devices.
(E) Voltage response to a current injection (120 pA, 8 ms) into the circuit. Response was measured in a current-clamp mode. Note that the voltage response did not saturate within 8 ms.
(F) Current response to a voltage step (−60 mV to 0 mV, 8 ms) into the circuit obtained in a voltage-clamp mode. Unlike in the current-clamp mode, the response follows the voltage step rapidly.
(G) Sample current response to a voltage step (from −40 mV to 20 mV, 8 ms). Arrowhead indicates the current reflecting an action potential (action current). Action current appeared ∼5 ms after the onset of stimuli.
(H) Five trials of current responses. The jitter of spike timing was less than 1 ms.

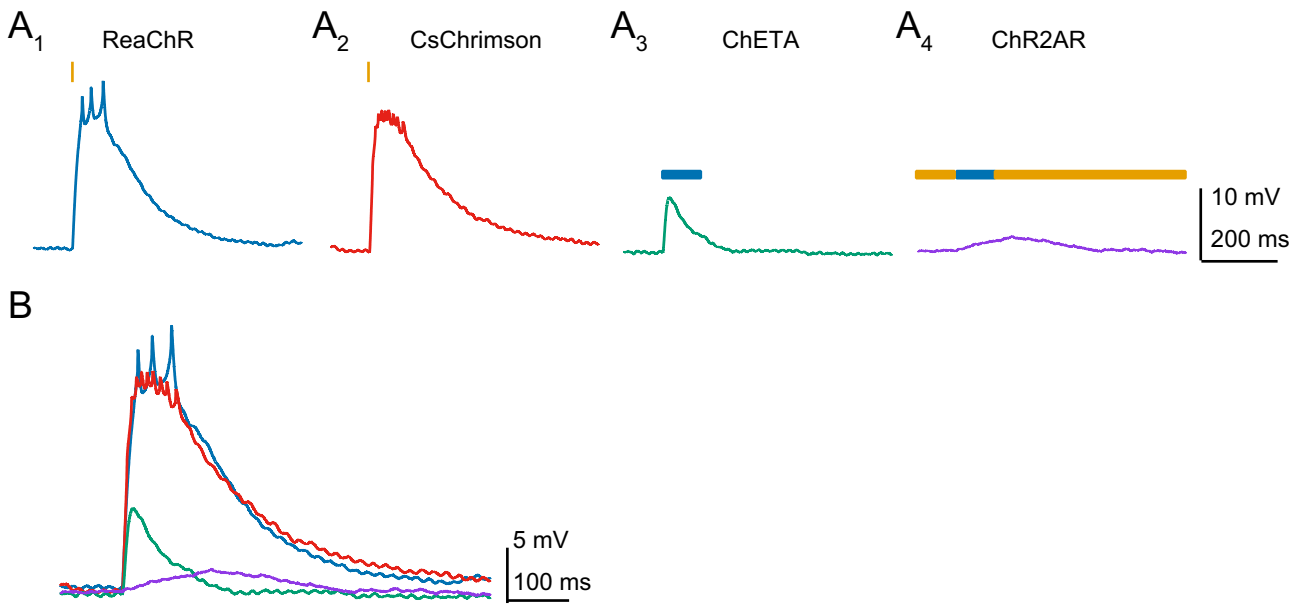

Figure 31: Induction of single action potentials by optogenetics
(A) Sample responses of PNs expressing ReaChR (A_1), CsChrimson (A_2), ChETA (A_3), and ChR2AR (A_4). The probes were stimulated by blue/amber LEDs. Duration of the stimulation was 0.01 ms (A_1, A_2), and 100 ms (A_3, A_4).
(B) Same traces as shown in A, but with baselines aligned to compare the temporal kinetics of the optogenetic probes.

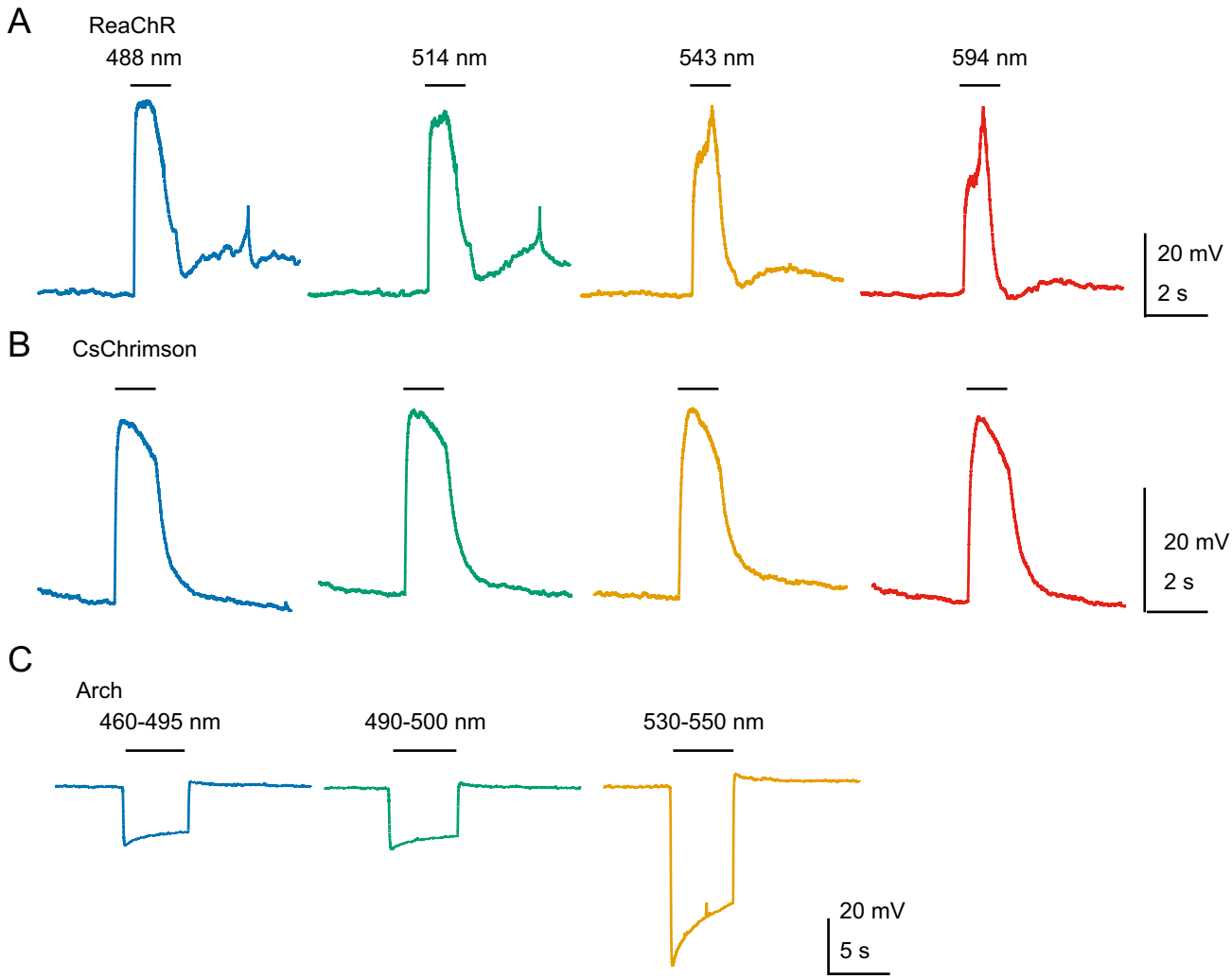

Figure 32: Wavelength specificity of optogenetic probes expressed in PNs
Sample traces obtained from a PN expressing ReaChR (A), CsChrimson (B) or Arch (C).
(A, B) Cells were stimulated with a CW laser. Laser intensities were 100-300 μW. These optogenetic probes depolarized PNs at similar level even with lasers emitting light with non-preferred wavelengths.
(C) Cells were stimulated with filtered light from a mercury lamp. Intensity of light was adjusted to $\sim$20 mW.

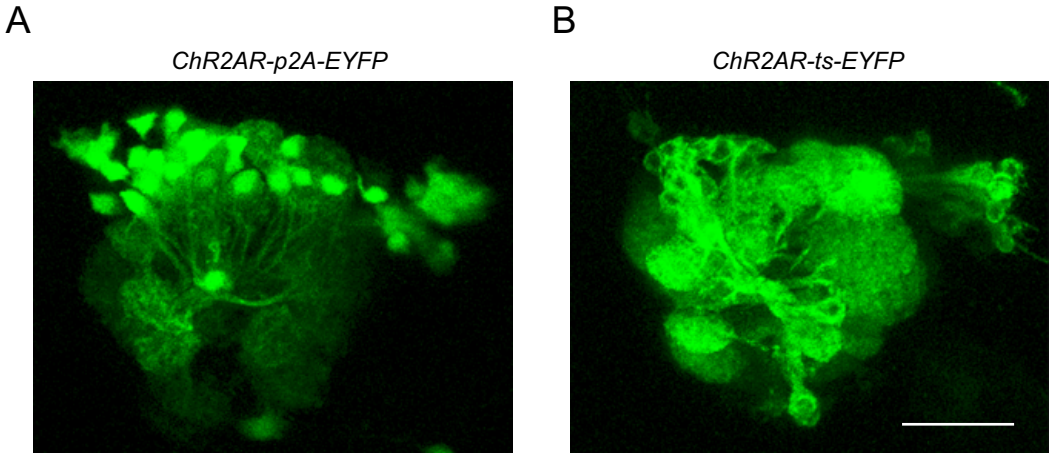

Figure 33: Expression of fluorescence proteins and the effect of a *p2A* sequence
(A) A confocal stack of a raw p2A-EYFP signal in PNs. Fluorescence signal from cell bodies was brighter than that from dendrites (glomeruli).
(B) A confocal stack of a raw ts-EYFP signal in PNs. Unlike p2A-EYFP, fluorescence signals from nuclei are dim and those from dendrites are bright. Scale bar, 30 μm. The confocal images were obtained by the same laser intensity.

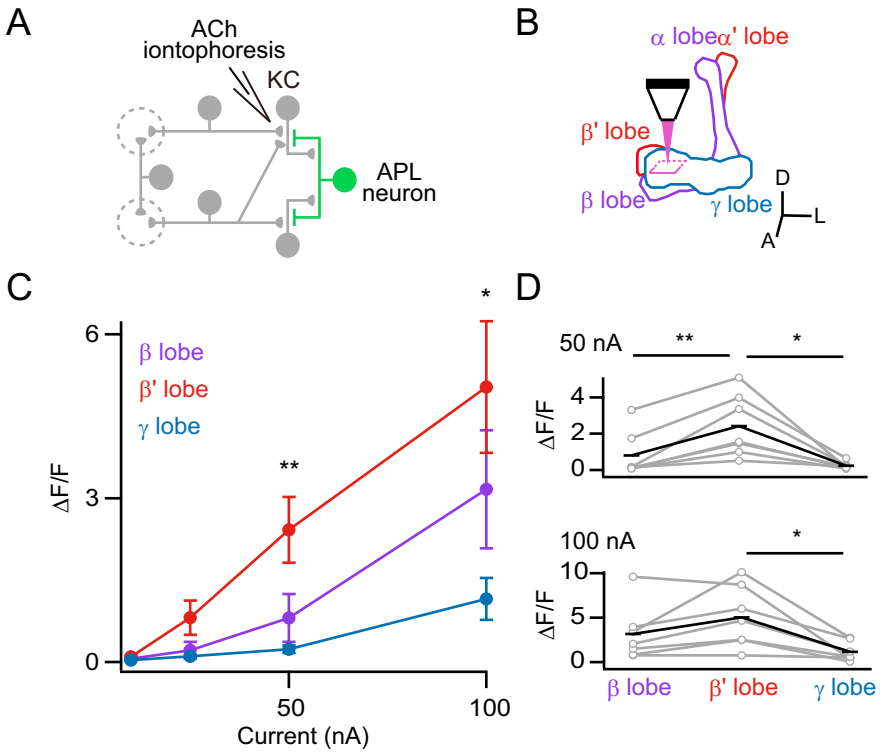

Figure 34: The spatial extent of calcium responses in APL neuron revealed by iontophoresis
(A) Schematic of the experiment. GCaMP was expressed in the APL neuron. KCs were activated by iontophoresis of acetylcholine (ACh) into the mushroom body calyx.
(B) GCaMP was imaged at the tip of lobes. A, anterior, D, dorsal, L, lateral. (C) Relationship between the response amplitude (ΔF/F) and the current amplitude. In each brain, all three lobes were imaged (n = 7 flies; $\star$p = 0.013, $\star\star$p $<$ 0.01, one-way ANOVA with repeated measurements with Holm correction).
(D) Calcium responses are significantly larger in the β' lobe than in the other lobes under stimulation with both 50 and 100 nA current injections ($\star$p = 0.013, $\star\star$p $<$ 0.01, paired t-test with Holm correction).

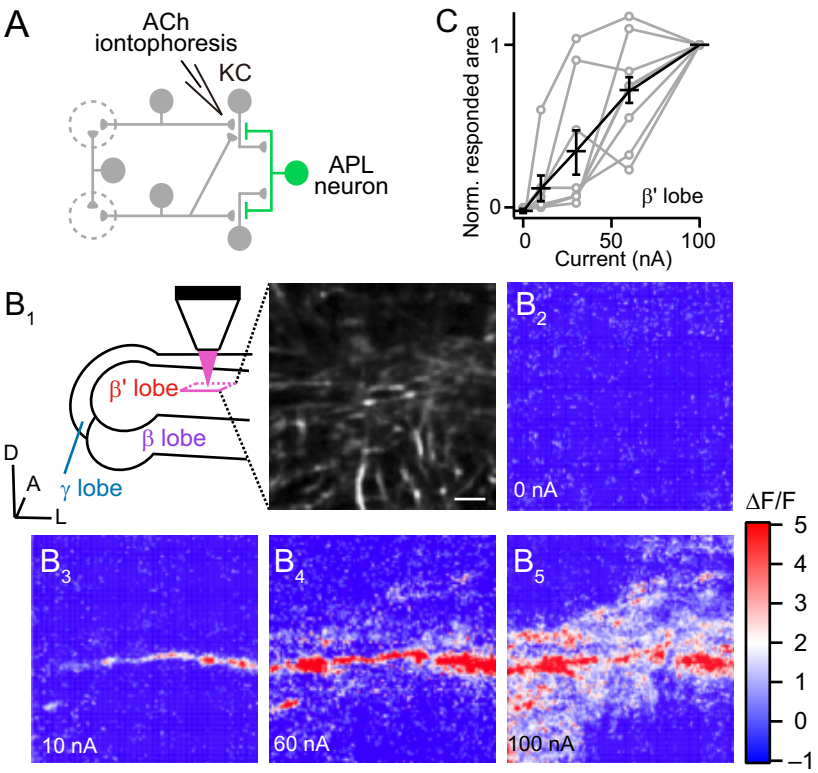

Figure 35: The spatial extent of calcium responses in APL neuron within lobes
(A) Schematic of the experiment. GCaMP was expressed in the APL neuron. KCs were activated by iontophoresis of acetylcholine (ACh) into the mushroom body calyx.
(B) Calcium imaging from the β' lobe. Schematic of imaging configuration (B_1). GCaMP6s was expressed in APL neurons under the control of *VT43924-Gal4*. ACh iontophoresis into the mushroom body calyx was used to provide an excitatory drive to KCs. The β' lobe was imaged from the dorsal side. Scale bar, 5 μm. As the current for iontophoresis was increased, GCaMP signals in the APL neuron spread from local to global regions first within and then beyond the β' lobe (B_2 to B_5).
(C) Peak responding area during ACh ejection period. Pixels in which $\Delta F/F$ exceeds 1.5 were defined as a responding area. Data were normalized by the response to 100 nA injection. n = 8 flies.

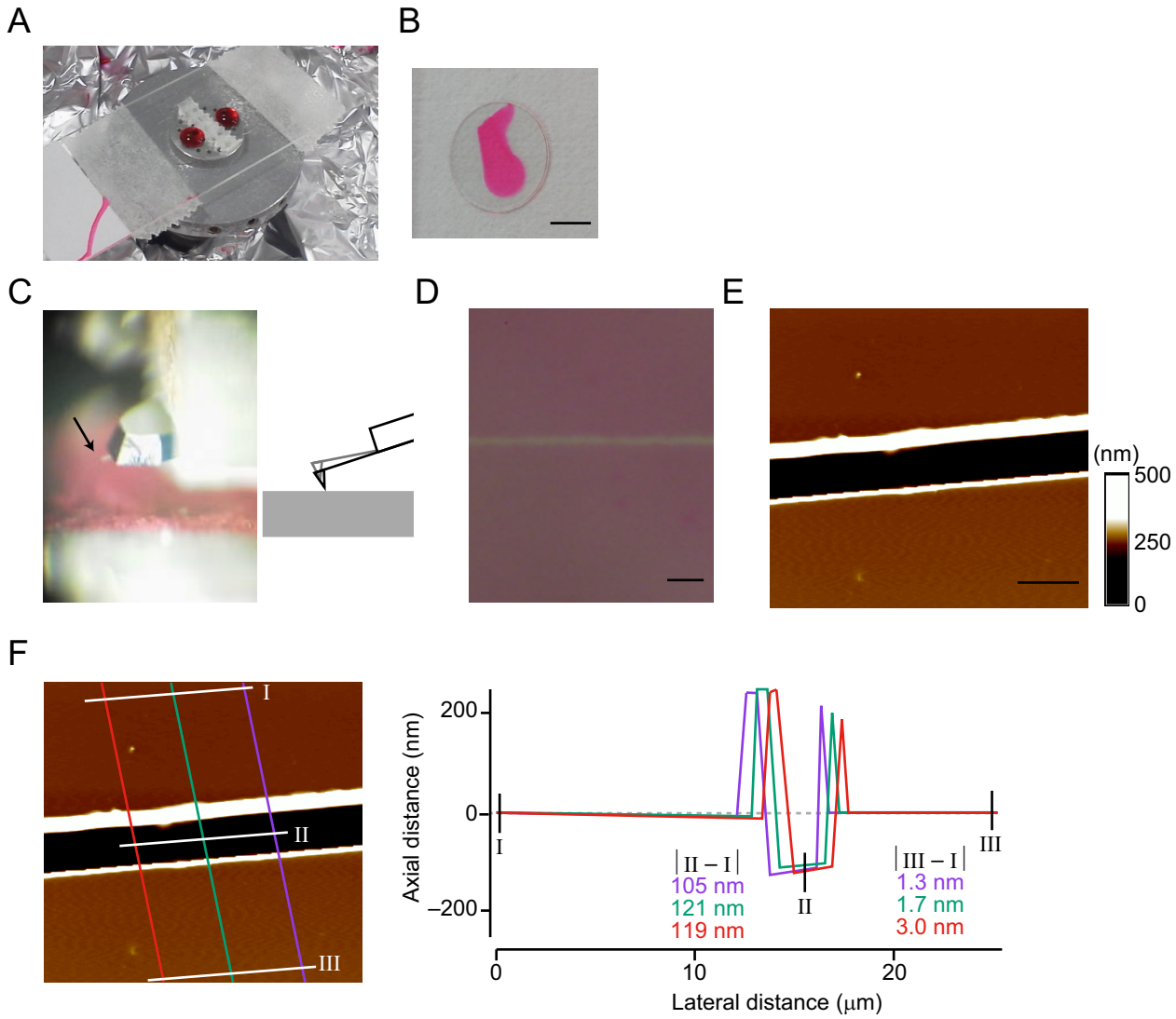

Figure 36: Generation of a thin fluorescent film and the measurement of its thickness
(A) Picture of two circular cover glasses on a spin coater. The red drops are PVA solution containing rodamine 6G. A piece of double-stick tape immobilizes the cover glass during spinning and prevents the spillover of the PVA solution to the reverse side.
(B) Spin-coated fluorescent film on the cover glass. Scale bar, 6 mm.
(C) Left, cantilever of AFM (arrow). Right, schematic of a tapping mode AFM scanning the surface of the sample.
(D) Stereoscopic image of a fluorescent film. Horizontal line in the middle is a scar made by a blade to measure the thickness of the film. Scale bar, 10 μm.
(E) Sample AFM image showing the thickness of the film. Scale bar, 5 μm.
(F) Sample AFM measurement of thickness. The thickness of the film, defined as the difference between the axial distances at I and II, was estimated to be 115 ± 7.1 nm (mean $\pm$ standard deviation).

Tables

Table 1: List of *VT33006-Gal4*-positive glomeruli
The list of antennal lobe glomeruli labeled by *VT33006-Gal4* (indicated with an open circle).

Glomerulus	VT033006
D	○
DA1	○
DA2	○
DA3	○
DA4l	○
DA4m	○
DC1	○
DC2	○
DC3	○
DC4	
DL1	○
DL2d	○
DL2v	○
DL3	○
DL4	○
DL5	○
DM1	
DM2	○
DM3	○
DM4	○
DM5	○
DM6	○
DP1l	
DP1m	○

Glomerulus	VT033006
V	
VA1d	○
VA1v	○
VA2	○
VA3	○
VA4	○
VA5	○
VA6	○
VA7l	○
VA7m	○
VC1	○
VC2	○
VC3l	○
VC3m	○
VC4	○
VL1	
VL2a	○
VL2p	
VM1	○
VM2	○
VM3	○
VM4	○
VM5d	○
VM5v	○
VM6	
VM7d	○
VM7v	○

Table 2: Combinations of Gal4 and UAS lines that cause lethality, in case of the progenies carry 1 Gal4 and 1 UAS.
Gal4 and UAS list that cause lethality when progenies carry 1 Gal4 and 1 UAS copies.

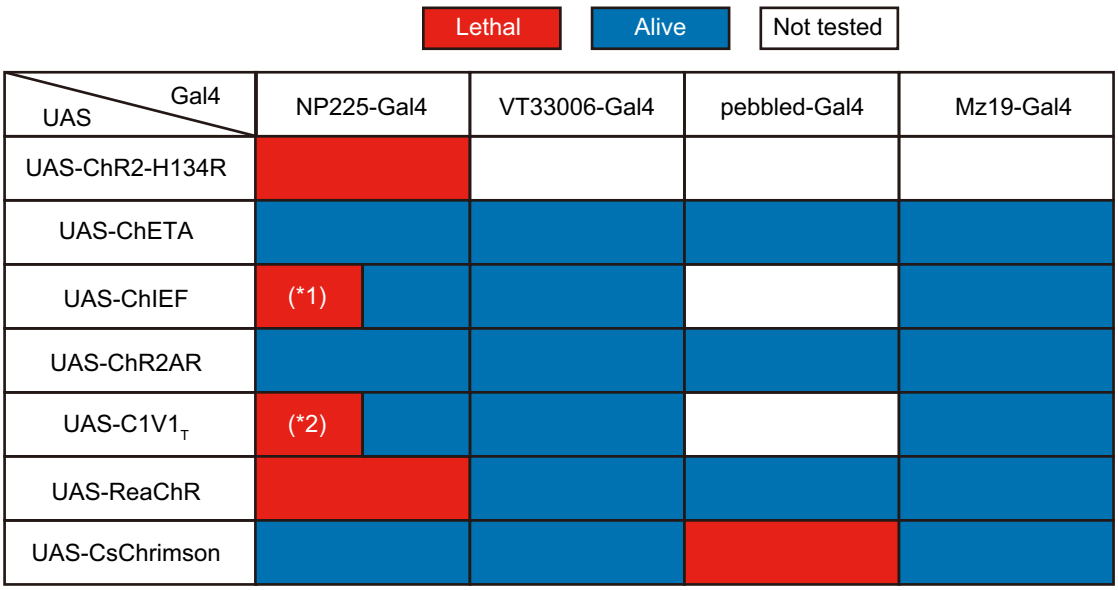

(*1) UAS-ChIEF[c3-3] was lethal. Other insertions, [c10-2], [c4-4] and [c1] were alive.

(*2) UAS-C1V1$_T$-p2A line was lethal. UAS-C1V1$_T$-ts line was alive.

Table 3: Combinations of Gal4 and UAS lines that cause lethality, in case of the progenies carry 2 Gal4 and 2 UAS.
Gal4 and UAS list that cause lethality when progenies carry 2 Gal4 and 2 UAS copies.

Lethal | Alive | Not tested

UAS \ Gal4	NP225-Gal4	VT33006-Gal4	pebbled-Gal4	Mz19-Gal4
UAS-ChR2-H134R				
UAS-ChETA		(*1)		(*2)
UAS-ChIEF				
UAS-ChR2AR				
UAS-C1V1$_T$				
UAS-ReaChR				
UAS-CsChrimson				(*3)

Genotypes with maximam number of Gal4 and UAS copies with which flies stay alive.
(*1) *UAS-ChETA (attP40)/+; VT33006-Gal4 (attP2)*
(*2) *Mz19-Gal4, UAS-ChETA (attP40)/+; UAS-ChETA (attP2)/+*
(*3) *Mz19-Gal4, UAS-CsChrimson (attP40)/+; +*

Table 4: Relationship between lethality and the expression level of an optogenetic probe.

Rearing temperature	Parental genotype		Genotype of progeny	N	Mathematical expectation	Actual probability	Lethality
25℃	*NP225-Gal4*	*UAS-C1V1$_T$-p2A (attP40)/CyO*	*NP225-Gal4/UAS-C1V1$_T$-p2A (attP40)*	0	50%	0%	◯
			Others	21	50%	100%	
	NP225-Gal4; +	*+; UAS-C1V1$_T$-p2A (attP2)/TM6b*	*NP225-Gal4/+; +/UAS-C1V1$_T$-p2A (attP2)*	1	50%	3.1%	◯
			Others	31	50%	96.9%	
	pebbled-Gal4/Y; +	*+; UAS-C1V1$_T$-p2A (attP40)/CyO*	*pebbled-Gal4/+; +/UAS-C1V1$_T$-p2A (attP40)*	0	50%	0%	◯
			Others	27	50%	100%	
	pebbled-Gal4/Y; +; +	*+; +; UAS-C1V1$_T$-p2A (attP2)*	*pebbled-Gal4/+; +; +/UAS-C1V1$_T$-p2A (attP2)*	0	50%	0%	◯
			Others	48	50%	100%	
18℃	*pebbled-Gal4/Y; tubP-Gal80(ts)/CyO*	*+; UAS-C1V1$_T$-p2A (attP40)/CyO*	*pebbled-Gal4/+; tubP-Gal80(ts)/UAS-C1V1$_T$-p2A (attP40)*	5	16.7%	25%	
			Others	15	83.3%	75%	
	pebbled-Gal4/Y; tubP-Gal80(ts)/CyO; +	*+; Bl/CyO; UAS-C1V1$_T$-p2A (attP2)/TM6b*	*pebbled-Gal4/+; tubP-Gal80(ts)/(Bl or CyO); +/UAS-C1V1$_T$-p2A (attP2)*	16	16.7%	30.2%	
			Others	37	83.3%	69.8%	
	pebbled-Gal4/Y; +	*+; UAS-C1V1$_T$-p2A (attP40)/CyO*	*pebbled-Gal4/+; +/UAS-C1V1$_T$-p2A (attP40)*	3	50%	13%	◯
			Others	20	50%	87%	
	pebbled-Gal4/Y; +; +	*+; +; UAS-C1V1$_T$-p2A (attP2)*	*pebbled-Gal4/+; +; +/UAS-C1V1$_T$-p2A (attP2)*	3	50%	6.8%	◯
			Others	41	50%	93.2%	

Table 5: List of genotypes used in the experiments
The genotypes used in the study are as follows (continue to the next page):

Figure	Genotype
Figure 1D	*UAS-myrGFP (attP40)/+; UAS-myrGFP (attP2)/APL-Gal4*
Figures 3B, C	*NP3062-Gal4, UAS-CD8GFP/+; UAS-ChR2-C/+; UAS-ChR2-B/+*
Figures 3E, F	*UAS-Archaerhodopsin (attP40); VT33006-Gal4 (attP2)*
Figure 8B	*Mz19-Gal4, UAS-ReaChR (attP40); +*
Figures 10B-D	*NP225-Gal4/UAS-CD8GFP; UAS-P2X$_2$/+*
Figure 11B	*NP225-Gal4, UAS-myrGFP (attP40)/+; UAS-ChIEF*[c10-2]/+
Figure 11C	*NP225-Gal4/+; UAS-C1V1$_{\mathrm{T}}$(attP2)/+*
Figure 11D	*Mz19-Gal4/UAS-C1V1$_{\mathrm{T}}$-p2A (attP40)*
Figure 11E	*NP225-Gal4/UAS-ChR2AR (attP40)*
Figure 11F	*UAS-ReaChR (attP40)/+; VT33006-Gal4 (attP2)/+*
Figure 12B	*NP225-Gal4, UAS-myrGFP (attP40)/+; UAS-ChIEF*[c10-2]/+
Figure 12C	*NP225-Gal4/UAS-ChR2AR (attP40)*
Figure 12D	*UAS-ReaChR (attP40)/+; VT33006-Gal4 (attP2)/+*
Figures 13A-C	*UAS-myrGFP (attP40)/+; UAS-myrGFP (attP2)/VT33006-Gal4 (attP2)*
Figures 14B-G	*UAS-ReaChR (attP40)/+; VT33006-Gal4 (attP2)/+*
Figures 15A, B	*UAS-ReaChR (attP40)/+; VT33006-Gal4 (attP2)/+*
Figures 16B-F	*UAS-ReaChR (attP40)/+; VT33006-Gal4 (attP2)/+*
Figures 18B, C	*Mz19-Gal4, UAS-ReaChR (attP40); +*
Figure 20B	*UAS-myrGFP (attP40)/+; UAS-myrGFP (attP2)/APL-Gal4*
Figures 20C-E	*UAS-Archaerhodopsin (attP40); APL-Gal4*
Figure 21F	*UAS-Archaerhodopsin (attP40); APL-Gal4*
Figures 22B-E	*UAS-CsChrimson (attP40); VT43924-Gal4 (attP2)*
Figures 23A-E	*UAS-GCaMP6s (attP40); VT43924-Gal4 (attP2), UAS-GCaMP6s (VK00005)*
Figures 24A-D	*UAS-GCaMP5G (attP40); ; OK107-Gal4*
Figures 25A-E	*UAS-GCaMP5G (attP40); ; OK107-Gal4*
Figures 27B-F	*Mz19-Gal4, UAS-ReaChR (attP40); +*
Figures 28A-C	*UAS-ReaChR (attP40)/+; VT33006-Gal4 (attP2)/+*
Figure 31A$_1$	*Mz19-Gal4/UAS-ReaChR (attP40)*
Figure 31A$_2$	*Mz19-Gal4/UAS-CsChrimson (attP40)*
Figure 31A$_3$	*Mz19-Gal4/UAS-ChETA (attP40)*
Figure 31A$_4$	*VT33006-Gal4 (attP2)/UAS-ChR2AR (attP2)*

Figure	Genotype
Figure 32A	*UAS-ReaChR (attP40)/+; VT33006-Gal4 (attP2)/+*
Figure 32B	*NP225-Gal4/+; UAS-CsChrimson (attP2)/+*
Figure 32C	*UAS-Arch (attP40); VT33006-Gal4 (attP2)*
Figure 33A	*NP225-Gal4/UAS-ChR2AR-p2A-EYFP (attP40)*
Figure 33B	*NP225-Gal4/UAS-ChR2AR-ts-EYFP (attP40)*
Figures 34A-D	*UAS-GCaMP6s (attP40); VT43924-Gal4 (attP2), UAS-GCaMP6s (VK00005)*
Figures 35A-C	*UAS-GCaMP6s (attP40); VT43924-Gal4 (attP2), UAS-GCaMP6s (VK00005)*

References

[1] Akalal, D.B., Yu, D., and Davis, R.L. (2010). A late-phase, long-term memory trace forms in the γ neurons of *Drosophila* mushroom bodies after olfactory classical conditioning. Journal of Neuroscience 30, 16699-16708.

[2] Akalal, D.B., Yu, D., and Davis, R.L. (2011). The long-term memory trace formed in the *Drosophila* α/β mushroom body neurons is abolished in long-term memory mutants. Journal of Neuroscience 31, 5643-5647.

[3] Akerboom, J., Chen, T.W., Wardill, T.J., Tian, L., Marvin, J.S., Mutlu, S., Calderon, N.C., Esposti, F., Borghuis, B.G., Sun, X.R., Gordus, A. Orger, M.B., Portugues, R., Engert, F., Macklin, J.J., Filosa, A., Aggarwal, A., Kerr, R.A., Takagi, R., Kracun, S., Shigetomi, E., Khakh, B.S., Baier, H., Lagnado, L., Wang, S.S.-H., Bargmann, C.L., Kimmel, B.E., Jayaraman, V., Svoboda, K., Kim, D.S., Schreiter, E.R., and Looger, L.L. (2012). Optimization of a GCaMP calcium indicator for neural activity imaging. Journal of Neuroscience 32, 13819-13840.

[4] Andrasfalvy, B.K., Zemelman, B.V., Tang, J., and Vaziri, A. (2010). Two-photon single-cell optogenetic control of neuronal activity by sculpted light. Proc. Natl. Acad. Sci. USA 107, 11981-11986.

[5] Ascoli, G.A., Alonso-Nanclares, L., Anderson, S.A., Barrionuevo, G., Benavides-Piccione, R., Burkhalter, A., Buzsáki, G., Cauli, B., Defelipe, J., Fairén, A., Fiedmever, D., Fishell, G., Freqnac, Y., Freund, T.F, Gardner, D., Gardner, E.P., Goldberg, J.H., Helmstaedter, S., Karube, F., Kisvárday, Z.F., Lambolez, B., Lewins, D.A., Marin, O., Markram, H., Muñoz, A., Packer, A., Peterson, C.C., Rockland, K.S., Rossier, J., Rudy, B., Somogyi, P., Staiger, J.F., Tamas, G., Thomson, A.M., Toledo-Rodoriguez, M., Wang, Y., West, D.C., and Yuste, R. (2008). Petilla terminology: nomenclature of features of GABAergic interneurons of the cerebral cortex. Nature Reviews Neuroscience 9, 557-568.

[6] Aso, Y., Grubel, K., Busch, S., Friedrich, A.B., Siwanowicz, I., and Tanimoto, H. (2009). The mushroom body of adult *Drosophila* characterized by GAL4 drivers. Journal of Neurogenetics 23, 156-172.

[7] Aso, Y., Herb, A., Ogueta, M., Siwanowicz, I., Templier, T., Friedrich, A.B., Ito, K., Scholz, H., and Tanimoto, H. (2012). Three dopamine pathways induce aversive odor memories with different stability. PLoS Genetics 8, e1002768.

[8] Aso, Y., Hattori, D., Yu, Y., Johnston, R.M., Iyer, N.A., Ngo, T.T., Dionne, H., Abbott, L.F., Axel, R., Tanimoto, H., and Rubin, G.M. (2014a). The neuronal architecture of the mushroom body provides a logic for associative learning. Elife 3, e04577.

[9] Aso, Y., Sitaraman, D., Ichinose, T., Kaun, K.R., Vogt, K., Belliart-Guerin, G., Placais, P.Y., Robie, A.A., Yamagata, N., Schnaitmann, C., Rowell, W.J., Johnson, R.M., Ngo, T.T., Chen, N., Korff, W., Nitabach, M.N., Heberlein, U., preat, T., Branson, K.M., Tanimoto, H., and Rubin, G.M. (2014b). Mushroom body output neurons encode valence and guide memory-based action selection in *Drosophila.* Elife 3, e04580.

[10] Aso, Y., and Rubin, G.M. (2016). Dopaminergic neurons write and update memories with cell-type-specific rules. Elife 5, e16135.

[11] Badel, L., Ohta, K., Tsuchimoto, Y., and Kazama, H. (2016). Decoding of context-dependent olfactory behavior in *Drosophila.* Neuron 91, 155-167.

[12] Baker, B.J., Kosmidis, E.K., Vucinic, D., Falk, C.X., Cohen, L.B., Djurisic, M., and Zecevic, D. (2005). Imaging brain activity with voltage- and calcium-sensitive dyes. Cellular and Molecular Neurobiology 25, 245-282.

[13] Berndt, A., Yizhar, O., Gunaydin, L.A., Hegemann, P., and Deisseroth, K. (2009). Bi-stable neural state switches. Nature Neuroscience 12, 229-234.

[14] Berndt, A., Lee, S.Y., Ramakrishnan, C., and Deisseroth, K. (2014). Structure-guided transformation of channelrhodopsin into a light-activated chloride channel. Science 344, 420-424.

[15] Bhandawat, V., Olsen, S.R., Gouwens, N.W., Schlief, M.L., and Wilson, R.I. (2007). Sensory processing in the *Drosophila* antennal lobe increases reliability and separability of ensemble odor representations. Nature Neuroscience 10, 1474-1482.

[16] Bischof, J., Maeda, R.K., Hediger, M., Karch, F., and Basler, K. (2007). An optimized transgenesis system for *Drosophila* using germ-line-specific ϕC31 integrases. Proc. Natl. Acad. Sci. USA 104, 3312-3317.

[17] Blum, A.L., Li, W., Cressy, M., and Dubnau, J. (2009). Short- and long-term memory in *Drosophila* require cAMP signaling in distinct neuron types. Current Biology 19, 1341-1350.

[18] Boyden, E.S. (2015). Optogenetics and the future of neuroscience. Nature Neuroscience 18, 1200-1201.

[19] Boyden, E.S., Zhang, F., Bamberg, E., Nagel, G., and Deisseroth, K. (2005). Millisecond-timescale, genetically targeted optical control of neural activity. Nature Neuroscience 8, 1263-1268.

[20] Brand, A.H., and Perrimon, N. (1993). Targeted gene expression as a means of altering cell fates and generating dominant phenotypes. Development 118, 401-415.

[21] Briggman, K.L., Abarbanel, H.D., and Kristan, W.B., Jr. (2005). Optical imaging of neuronal populations during decision-making. Science 307, 896-901.

[22] Brown, E.B., Shear, J.B., Adams, S.R., Tsien, R.Y., and Webb, W.W. (1999). Photolysis of caged calcium in femtoliter volumes using two-photon excitation. Biophysical Journal 76, 489-499.

[23] Burke, C.J., Huetteroth, W., Owald, D., Perisse, E., Krashes, M.J., Das, G., Gohl, D., Silies, M., Certel, S., and Waddell, S. (2012). Layered reward signalling through octopamine and dopamine in *Drosophila.* Nature 492, 433-437.

[24] Burrows, M., and Siegler, M.V. (1976). Transmission without spikes between locust interneurones and motoneurones. Nature 262, 222-224.

[25] Cao, G., Platisa, J., Pieribone, V.A., Raccuglia, D., Kunst, M., and Nitabach, M.N. (2013). Genetically targeted optical electrophysiology in intact neural circuits. Cell 154, 904-913.

[26] Caron, S.J., Ruta, V., Abbott, L.F., and Axel, R. (2013). Random convergence of olfactory inputs in the *Drosophila* mushroom body. Nature 497, 113-117.

[27] Cervantes-Sandoval, I., Martin-Pena, A., Berry, J.A., and Davis, R.L. (2013). System-like consolidation of olfactory memories in *Drosophila.* Journal of Neuroscience 33, 9846-9854.

[28] Chen, T.W., Wardill, T.J., Sun, Y., Pulver, S.R., Renninger, S.L., Baohan, A., Schreiter, E.R., Kerr, R.A., Orger, M.B., Jayaraman, V., Looger, L.L., Svoboda, K., and Kim, D.S. (2013). Ultrasensitive fluorescent proteins for imaging neuronal activity. Nature 499, 295-300.

[29] Chen, W.R., Xiong, W., and Shepherd, G.M. (2000). Analysis of relations between NMDA receptors and GABA release at olfactory bulb reciprocal synapses. Neuron 25, 625-633.

[30] Chow, B.Y., Han, X., Dobry, A.S., Qian, X., Chuong, A.S., Li, M., Henninger, M.A., Belfort, G.M., Lin, Y., Monahan, P.E., and Boyden, E.S. (2010). High-performance genetically targetable optical neural silencing by light-driven proton pumps. Nature 463, 98-102.

[31] Chuong, A.S., Miri, M.L., Busskamp, V., Matthews, G.A., Acker, L.C., Sorensen, A.T., Young, A., Klapoetke, N.C., Henninger, M.A., Kodandaramaiah, S.B., Ogawa, M., Ramanlal, S.B., Bandler, R.C., Allen, B.D., Forest, C.R., Chow, B.Y., Han, X., Lin, Y., Tye, K.M., Roska, B., Cardin, J.A., and Boyden, E.S. (2014). Noninvasive optical inhibition with a red-shifted microbial rhodopsin. Nature Neuroscience 17, 1123-1129.

[32] Cohn, R., Morantte, I., and Ruta, V. (2015). Coordinated and compartmentalized neuromodulation shapes sensory processing in *Drosophila.* Cell 163, 1742-1755.

[33] Connolly, J.B., Roberts, I.J., Armstrong, J.D., Kaiser, K., Forte, M., Tully, T., and O'Kane, C.J. (1996). Associative learning disrupted by impaired Gs signaling in *Drosophila* mushroom bodies. Science 274, 2104-2107.

[34] Costa, M., Manton, J.D., Ostrovsky, A.D., Prohaska, S., and Jefferis, G.S. (2016). NBLAST: Rapid, sensitive comparison of neuronal structure and construction of neuron family databases. Neuron 91, 293-311.

[35] Crittenden, J.R., Skoulakis, E.M., Han, K.A., Kalderon, D., and Davis, R.L. (1998). Tripartite mushroom body architecture revealed by antigenic markers. Learning and Memory 5, 38-51.

[36] Crocker, A., Guan, X.J., Murphy, C.T., and Murthy, M. (2016). Cell-type-specific transcriptome analysis in the *Drosophila* mushroom body reveals memory-related changes in gene expression. Cell Reports 15, 1580-1596.

[37] Curley, P.F., Ferguson, A.I., White, J.G., and Amos, W.B. (1992). Application of a femtosecond self-sustaining mode-locked Ti-sapphire laser to the field of laser scanning confocal microscopy. Optical and Quantum Electronics 24, 851-859.

[38] Daniels, R.W., Rossano, A.J., Macleod, G.T., and Ganetzky, B. (2014). Expression of multiple transgenes from a single construct using viral 2A peptides in *Drosophila.* PLoS ONE 9, e100637.

[39] DasGupta, S., Ferreira, C.H., Miesenböck, G. (2014). FoxP influences the speed and accuracy of a perceptual decision in *Drosophila.* Science 344, 901-904.

[40] Davison, I.G., and Ehlers, M.D. (2011). Neural circuit mechanisms for pattern detection and feature combination in olfactory cortex. Neuron 70, 82-94.

[41] Deisseroth, K. (2015). Optogenetics: 10 years of microbial opsins in neuroscience. Nature Neuroscience 18, 1213-1225.

[42] Deisseroth, K., Feng, G., Majewska, A.K., Miesenböck, G., Ting, A., and Schnitzer, M.J. (2006). Next-generation optical technologies for illuminating genetically targeted brain circuits. Journal of Neuroscience 26, 10380-10386.

[43] Denk, W., Strickler, J.H., and Webb, W.W. (1990). Two-photon laser scanning fluorescence microscopy. Science 248, 73-76.

[44] Denk, W., Piston, D.W., and Webb, W.W. (2006). Multi-photon mulecular excitation in laser-scanning microscopy. In: Pawley, J.B. (ed) Handbook of biological confocal microscopy. Third edition, Chapter 28.

[45] Diaspro, A., Chirico, G., and Collini, M. (2005). Two-photon fluorescence excitation and related techniques in biological microscopy. Quarterly Reviews of Biophysics 38, 97-166.

[46] Drobizhev, M., Makarov, N.S., Tillo, S.E., Hughes, T.E., and Rebane, A. (2011). Two-photon absorption properties of fluorescent proteins. Nature Methods 8, 393-399.

[47] Dubnau, J., Grady, L., Kitamoto, T., and Tully, T. (2001). Disruption of neurotransmission in *Drosophila* mushroom body blocks retrieval but not acquisition of memory. Nature 411, 476-480.

[48] Ellis-Davies, G.C. (2007). Caged compounds: photorelease technology for control of cellular chemistry and physiology. Nature Methods 4, 619-628.

[49] Ellis-Davies, G.C., and Kaplan, J.H. (1994). Nitrophenyl-EGTA, a photolabile chelator that selectively binds Ca^{2+} with high affinity and releases it rapidly upon photolysis. Proc. Natl. Acad. Sci. USA 91, 187-191.

[50] Engels, J., and Schlaeger, E.J. (1977). Synthesis, structure, and reactivity of adenosine cyclic 3′,5′-phosphate benzyl triesters. Journal of Medicinal Chemistry 20, 907-911.

[51] Farris, S.M., Robinson, G.E., Davis, R.L., and Fahrbach, S.E. (1999). Larval and pupal development of the mushroom bodies in the honey bee, *Apis mellifera*. Journal of Comparative Neurology 414, 97-113.

[52] Filevich, O., Salierno, M., and Etchenique, R. (2010). A caged nicotine with nanosecond range kinetics and visible light sensitivity. Journal of Inorganic Biochemistry 104, 1248-1251.

[53] Fino, E., Araya, R., Peterka, D.S., Salierno, M., Etchenique, R., and Yuste, R. (2009). RuBi-glutamate: Two-photon and visible-light photoactivation of neurons and dendritic spines. Frontiers in Neural Circuits 3, 2.

[54] Goodman, M.B., and Lockery, S.R. (2000). Pressure polishing: a method for re-shaping patch pipettes during fire polishing. Journal of Neuroscience Methods 100, 13-15.

[55] Göppert-Mayer, M. (1931). Über elementarakte mit zwei quantensprüngen. Annalen der Physik 9, 273-294. English translation: Koepke, D.C. (2009). Elementary processes with two quantum transitions. Annals of Physics 18, 466-479.

[56] Gouwens, N.W., and Wilson, R.I. (2009). Signal propagation in *Drosophila* central neurons. Journal of Neuroscience 29, 6239-6249.

[57] Govorunova, E.G., Sineshchekov, O.A., Janz, R., Liu, X., and Spudich, J.L. (2015). Natural light-gated anion channels: A family of microbial rhodopsins for advanced optogenetics. Science 349, 647-650.

[58] Graubard, K. (1978). Synaptic transmission without action potentials: input-output properties of a nonspiking presynaptic neuron. Journal of Neurophysiology 41, 1014-1025.

[59] Greenspan, R.J. (1997). Fly pushing. The theory and practice of *Drosophila* genetics. Cold Spring Harbor Laboratory Press.

[60] Gruntman, E., and Turner, G.C. (2013). Integration of the olfactory code across dendritic claws of single mushroom body neurons. Nature Neuroscience 16, 1821-1829.

[61] Gunaydin, L.A., Yizhar, O., Berndt, A., Sohal, V.S., Deisseroth, K., and Hegemann, P. (2010). Ultrafast optogenetic control. Nature Neuroscience 13, 387-392.

[62] Hayashi, S., Ito, K., Sado, Y., Taniguchi, M., Akimoto, A., Takeuchi, H., Aigaki, T., Matsuzaki, F., Nakagoshi, H., Tanimura, T., Ueda, R., Uemura, T., Yoshihara, M., and Goto, S. (2002). GETDB, a database compiling expression patterns and molecular locations of a collection of Gal4 enhancer traps. Genesis 34, 58-61.

[63] Hegemann, P., Ehlenbeck, S., and Gradmann, D. (2005). Multiple photocycles of channelrhodopsin. Biophysical Journal 89, 3911-3918.

[64] Heisenberg, M. (2003). Mushroom body memoir: from maps to models. Nature Reviews Neuroscience 4, 266-275.

[65] Helmchen, F., and Denk, W. (2005). Deep tissue two-photon microscopy. Nature Methods 2, 932-940.

[66] Hige, T., Aso, Y., Modi, M.N., Rubin, G.M., and Turner, G.C. (2015). Heterosynaptic plasticity underlies aversive olfactory learning in *Drosophila.* Neuron 88, 985-998.

[67] Hirase, H., Nikolenko, V., Goldberg, J.H., and Yuste, R. (2002). Multiphoton stimulation of neurons. Journal of Neurobiology 51, 237-247.

[68] Hockberger, P.E., Skimina, T.A., Centonze, V.E., Lavin, C., Chu, S., Dadras, S., Reddy, J.K., and White, J.G. (1999). Activation of flavin-containing oxidases underlies light-induced production of H_2O_2 in mammalian cells. Proc. Natl. Acad. Sci. USA 96, 6255-6260.

[69] Honegger, K.S., Campbell, R.A., and Turner, G.C. (2011). Cellular-resolution population imaging reveals robust sparse coding in the *Drosophila* mushroom body. Journal of Neuroscience 31, 11772-11785.

[70] Huggett, G.R. (1968). Mode-locking of CW lasers by regenerative RF feedback. Applied Physics Letters 13, 186.

[71] Hwang, R.Y., Zhong, L., Xu, Y., Johnson, T., Zhang, F., Deisseroth, K., and Tracey, W.D. (2007). Nociceptive neurons protect *Drosophila* larvae from parasitoid wasps. Current Biology 17, 2105-2116.

[72] Ichinose, T., Aso, Y., Yamagata, N., Abe, A., Rubin, G.M., and Tanimoto, H. (2015). Reward signal in a recurrent circuit drives appetitive long-term memory formation. Elife 4, e10719.

[73] Inagaki, H.K., Jung, Y., Hoopfer, E.D., Wong, A.M., Mishra, N., Lin, J.Y., Tsien, R.Y., and Anderson, D.J. (2014). Optogenetic control of *Drosophila* using a red-shifted channelrhodopsin reveals experience-dependent influences on courtship. Nature Methods 11, 325-332.

[74] Isaacson, J.S., and Strowbridge, B.W. (1998). Olfactory reciprocal synapses: dendritic signaling in the CNS. Neuron 20, 749-761.

[75] Ito, K., Suzuki, K., Estes, P., Ramaswami, M., Yamamoto, D., and Strausfeld, N.J. (1998). The organization of extrinsic neurons and their implications in the functional roles of the mushroom bodies in *Drosophila melanogaster Meigen.* Learning and Memory 5, 52-77.

[76] Jefferis, G.S., Marin, E.C., Stocker, R.F., and Luo, L. (2001). Target neuron prespecification in the olfactory map of *Drosophila.* Nature 414, 204-208.

[77] Jefferis, G.S., Vyas, R.M., Berdnik, D., Ramaekers, A., Stocker, R.F., Tanaka, N.K., Ito, K., and Luo, L. (2004). Developmental origin of wiring specificity in the olfactory system of *Drosophila.* Development 131, 117-130.

[78] Jenett, A., Rubin, G.M., Ngo, T.T., Shepherd, D., Murphy, C., Dionne, H., Pfeiffer, B.D., Cavallaro, A., Hall, D., Jeter, J., Iyer, N., Fetter, D., Hausenfluck, J.H., Peng, H., Trautman, E.T., Svirskas, R.R., Myers, E.W., Iwinski, Z.R., Aso, Y., DePasguale, G.M., Enos, A., Hulamm, P., Lam, S.C., Laverty, T.R., Long, F., Qu, L., Murphy, S.D., Rokicki, K., Safford, T., Shaw, K., Simpson, J.H., Sowell, A., Tae, S., Yu, Y., and Zugates, C.T. (2012). A GAL4-driver line resource for *Drosophila* neurobiology. Cell Reports 2, 991-1001.

[79] Johnson, B.E., Brown, A.L., and Goodman, M.B. (2008). Pressure-polishing pipettes for improved patch-clamp recording. Journal of Visualized Experiments 20, 964.

[80] Kaiser, W., and Garrett, C.G.B. (1961). 2-photon excitation in CaF_2-Eu^{2+}. Physical Review Letters 7, 229.

[81] Kaplan, J.H., Forbush, B., 3rd, and Hoffman, J.F. (1978). Rapid photolytic release of adenosine 5′-triphosphate from a protected analogue: utilization by the Na:K pump of human red blood cell ghosts. Biochemistry 17, 1929-1935.

[82] Kato, H.E., Zhang, F., Yizhar, O., Ramakrishnan, C., Nishizawa, T., Hirata, K., Ito, J., Aita, Y., Tsukazaki, T., Hayashi, S., Hegemann, P., Maturana, A.D., Ishitani, R., Deisseroth, K., and Nureki, O. (2012). Crystal structure of the channelrhodopsin light-gated cation channel. Nature 482, 369-374.

[83] Kazama, H., and Wilson, R.I. (2009). Origins of correlated activity in an olfactory circuit. Nature Neuroscience 12, 1136-1144.

[84] Khakh, B.S., and North, R.A. (2012). Neuromodulation by extracellular ATP and P2X receptors in the CNS. Neuron 76, 51-69.

[85] Klapoetke, N.C., Murata, Y., Kim, S.S., Pulver, S.R., Birdsey-Benson, A., Cho, Y.K., Morimoto, T.K., Chuong, A.S., Carpenter, E.J., Tian, Z., Wang, J., Xie, Y., Yan, Z., Zhang, Y., Chow, B.Y., Surek, B., Melkonian, M., Jayaraman, V., Constantine-Paton, M., Wong, G.K., and Boyden, E.S. (2014). Independent optical excitation of distinct neural populations. Nature Methods 11, 338-346.

[86] Kleinlogel, S., Feldbauer, K., Dempski, R.E., Fotis, H., Wood, P.G., Bamann, C., and Bamberg, E. (2011). Ultra light-sensitive and fast neuronal activation with the Ca^{2+}-permeable channelrhodopsin CatCh. Nature Neuroscience 14, 513-518.

[87] Krashes, M.J., Keene, A.C., Leung, B., Armstrong, J.D., and Waddell, S. (2007). Sequential use of mushroom body neuron subsets during *Drosophila* odor memory processing. Neuron 53, 103-115.

[88] Krashes, M.J., and Waddell, S. (2008). Rapid consolidation to a radish and protein synthesis-dependent long-term memory after single-session appetitive olfactory conditioning in *Drosophila*. Journal of Neuroscience 28, 3103-3113.

[89] Kudoh, S.N., and Taguchi, T. (2002). A simple exploratory algorithm for the accurate and fast detection of spontaneous synaptic events. Biosensors and Bioelectronics 17, 773-782.

[90] Lai, S.L., and Lee, T. (2006). Genetic mosaic with dual binary transcriptional systems in *Drosophila.* Nature Neuroscience 9, 703-709.

[91] Lee, T., Lee, A., and Luo, L. (1999). Development of the *Drosophila* mushroom bodies: sequential generation of three distinct types of neurons from a neuroblast. Development 126, 4065-4076.

[92] Lee, T., and Luo, L. (1999). Mosaic analysis with a repressible cell marker for studies of gene function in neuronal morphogenesis. Neuron 22, 451-461.

[93] Leiss, F., Groh, C., Butcher, N.J., Meinertzhagen, I.A., and Tavosanis, G. (2009). Synaptic organization in the adult *Drosophila* mushroom body calyx. Journal of Comparative Neurology 517, 808-824.

[94] Leitch, B., and Laurent, G. (1996). GABAergic synapses in the antennal lobe and mushroom body of the locust olfactory system. Journal of Comparative Neurology 372, 487-514.

[95] Lima, S.Q., and Miesenböck, G. (2005). Remote control of behavior through genetically targeted photostimulation of neurons. Cell 121, 141-152.

[96] Lin, A.C., Bygrave, A.M., de Calignon, A., Lee, T., and Miesenböck, G. (2014). Sparse, decorrelated odor coding in the mushroom body enhances learned odor discrimination. Nature Neuroscience 17, 559-568.

[97] Lin, H.H., Lai, J.S., Chin, A.L., Chen, Y.C., and Chiang, A.S. (2007). A map of olfactory representation in the *Drosophila* mushroom body. Cell 128, 1205-1217.

[98] Lin, J.Y., Lin, M.Z., Steinbach, P., and Tsien, R.Y. (2009). Characterization of engineered channelrhodopsin variants with improved properties and kinetics. Biophysical Journal 96, 1803-1814.

[99] Lin, J.Y., Knutsen, P.M., Muller, A., Kleinfeld, D., and Tsien, R.Y. (2013). ReaChR: a red-shifted variant of channelrhodopsin enables deep transcranial optogenetic excitation. Nature Neuroscience 16, 1499-1508.

[100] Litwin-Kumar, A., Harris, K.D., Axel, R., Sompolinsky, H., and Abbott, L.F. (2017). Optimal degrees of synaptic connectivity. Neuron 93, 1153-1164.e7.

[101] Liu, C., Plaçais, P.Y., Yamagata, N., Pfeiffer, B.D., Aso, Y., Friedrich, A.B., Siwanowicz, I., Rubin, G.M., Preat, T., and Tanimoto, H. (2012). A subset of dopamine neurons signals reward for odour memory in *Drosophila.* Nature 488, 512-516.

[102] Liu, W.W., and Wilson, R.I. (2013). Glutamate is an inhibitory neurotransmitter in the *Drosophila* olfactory system. Proc. Natl. Acad. Sci. USA 110, 10294-10299.

[103] Liu, X., and Davis, R.L. (2009). The GABAergic anterior paired lateral neuron suppresses and is suppressed by olfactory learning. Nature Neuroscience 12, 53-59.

[104] Lutz, C., Otis, T.S., DeSars, V., Charpak, S., DiGregorio, D.A., and Emiliani, V. (2008). Holographic photolysis of caged neurotransmitters. Nature Methods 5, 821-827.

[105] Markram, H., Muller, E., Ramaswamy, S., Reimann, M.W., Abdellah, M., Sanchez, C.A., Ailamaki, A., Alonso-Nanclares, L., Antille, N., Arsever, S., Kahou, G.A., Berger, T.K., Bilgill, A., Buncic, N., Chalimourda, A., Chindemi, G., Courcol, J.D., Delalondre, F., Delattre, V., Druckmann, S., Dumusc, R., Dynes, J., Eilemann, S., Gal, E., Gevaert, M.E., Ghobril, J.P., Gidon, A., Graham, J.W., Gupta, A., Haenel, V., hay, E., Heinis, T., Hernando, J.B., Hines, M., Kanari, L., Keller, D., Kenyon, J., Khazen, G., Kim, Y., King, J.G., Kisvarday, Z., Kumbhar, P., Lasserre, S., Le Bé, J.V., Magalhães, B.R., Merchán-Pérez, A. meystre, J., Morrice, B.R., Muller, J., Muñoz-Céspedes, A., Muralidhar, S., Muthurasa, K., Nachbaur, D., Newton, T.H., Nolte, M., Ovcharenko, A., Palacios, J., Pastor, L., Perin, R., Ranjan, R., Riachi, I., Rodríguez, J.R., Riquelme, J.L., Rössert, C., Sfyrakis, K., Shillcok, J.C., Silberberg, G., Silva, R., Tauheed, F., Talefont, M., Toledo-Tororiguez, M., Tränker, T., Van Geit, W., Díaz, J.V., Walker, R., Wang, Y., Zaninetta, S.M., DeFelipe, J., HIll, S.L., Segev, I., and Schürmann, F. (2015). Reconstruction and simulation of neocortical microcircuitry. Cell 163, 456-492.

[106] Matsuzaki, M., Honkura, N., Ellis-Davies, G.C., and Kasai, H. (2004). Structural basis of long-term potentiation in single dendritic spines. Nature 429, 761-766.

[107] Mattis, J., Tye, K.M., Ferenczi, E.A., Ramakrishnan, C., O'Shea, D.J., Prakash, R., Gunaydin, L.A., Hyun, M., Fenno, L.E., Gradinaru, V., Yizhar, O., and Deisseroth, K. (2012). Principles for applying optogenetic tools derived from direct comparative analysis of microbial opsins. Nature Methods 9, 159-172.

[108] McGuire, S.E., Le, P.T., and Davis, R.L. (2001). The role of *Drosophila* mushroom body signaling in olfactory memory. Science 293, 1330-1333.

[109] McGuire, S.E., Le, P.T., Osborn, A.J., Matsumoto, K., and Davis, R.L. (2003). Spatiotemporal rescue of memory dysfunction in *Drosophila.* Science 302, 1765-1768.

[110] Momotake, A., Lindegger, N., Niggli, E., Barsotti, R.J., and Ellis-Davies, G.C. (2006). The nitrodibenzofuran chromophore: a new caging group for ultra-efficient photolysis in living cells. Nature Methods 3, 35-40.

[111] Murthy, M., Fiete, I., and Laurent, G. (2008). Testing odor response stereotypy in the *Drosophila* mushroom body. Neuron 59, 1009-1023.

[112] Nagel, G., Szellas, T., Huhn, W., Kateriya, S., Adeishvili, N., Berthold, P., Ollig, D., Hegemann, P., and Bamberg, E. (2003). Channelrhodopsin-2, a directly light-gated cation-selective membrane channel. Proc. Natl. Acad. Sci. USA 100, 13940-13945.

[113] Nakai, J., Ohkura, M., and Imoto, K. (2001). A high signal-to-noise Ca^{2+} probe composed of a single green fluorescent protein. Nature Biotechnology 19, 137-141.

[114] Nikolic, K., Grossman, N., Grubb, M.S., Burrone, J., Toumazou, C., and Degenaar, P. (2009). Photocycles of channelrhodopsin-2. Photochemistry and Photobiology 85, 400-411.

[115] Olson, J.P., Kwon, H.B., Takasaki, K.T., Chiu, C.Q., Higley, M.J., Sabatini, B.L., and Ellis-Davies, G.C. (2013). Optically selective two-photon uncaging of glutamate at 900 nm. Journal of the American Chemical Society 135, 5954-5957.

[116] Osborn, M.J., Panoskaltsis-Mortari, A., McElmurry, R.T., Bell, S.K., Vignali, D.A., Ryan, M.D., Wilber, A.C., McIvor, R.S., Tolar, J., and Blazar, B.R. (2005). A picornaviral 2A-like sequence-based tricistronic vector allowing for high-level therapeutic gene expression coupled to a dual-reporter system. Molecular Therapy 12, 569-574.

[117] Owald, D., Felsenberg, J., Talbot, C.B., Das, G., Perisse, E., Huetteroth, W., and Waddell, S. (2015). Activity of defined mushroom body output neurons underlies learned olfactory behavior in *Drosophila.* Neuron 86, 417-427.

[118] Papadopoulou, M., Cassenaer, S., Nowotny, T., and Laurent, G. (2011). Normalization for sparse encoding of odors by a wide-field interneuron. Science 332, 721-725.

[119] Papagiakoumou, E., Anselmi, F., Begue, A., de Sars, V., Gluckstad, J., Isacoff, E.Y., and Emiliani, V. (2010). Scanless two-photon excitation of channelrhodopsin-2. Nature Methods 7, 848-854.

[120] Perez-Orive, J., Mazor, O., Turner, G.C., Cassenaer, S., Wilson, R.I., and Laurent, G. (2002). Oscillations and sparsening of odor representations in the mushroom body. Science 297, 359-365.

[121] Perisse, E., Yin, Y., Lin, A.C., Lin, S., Huetteroth, W., and Waddell, S. (2013). Different Kenyon cell populations drive learned approach and avoidance in *Drosophila.* Neuron 79, 945-956.

[122] Perrat, P.N., DasGupta, S., Wang, J., Theurkauf, W., Weng, Z., Rosbash, M., and Waddell, S. (2013). Transposition-driven genomic heterogeneity in the *Drosophila* brain. Science 340, 91-95.

[123] Peterka, D.S., Takahashi, H., and Yuste, R. (2011). Imaging voltage in neurons. Neuron 69, 9-21.

[124] Petersen, L.K., and Stowers, R.S., A gateway multisite recombination cloning toolkit. PLoS ONE 6(9): e24531.

[125] Pfeiffer, B.D., Ngo, T.T., Hibbard, K.L., Murphy, C., Jenett, A., Truman, J.W., and Rubin, G.M. (2010). Refinement of tools for targeted gene expression in *Drosophila.* Genetics 186, 735-755.

[126] Pitman, J.L., Huetteroth, W., Burke, C.J., Krashes, M.J., Lai, S.L., Lee, T., and Waddell, S. (2011). A pair of inhibitory neurons are required to sustain labile memory in the *Drosophila* mushroom body. Current Biology 21, 855-861.

[127] Poo, C., and Isaacson, J.S. (2009). Odor representations in olfactory cortex: “sparse” coding, global inhibition, and oscillations. Neuron 62, 850-861.

[128] Potter, C.J., Tasic, B., Russler, E.V., Liang, L., and Luo, L. (2010). The Q system: a repressible binary system for transgene expression, lineage tracing, and mosaic analysis. Cell 141, 536-548.

[129] Prakash, R., Yizhar, O., Grewe, B., Ramakrishnan, C., Wang, N., Goshen, I., Packer, A.M., Peterka, D.S., Yuste, R., Schnitzer, M.J., and Deisseroth, K. (2012). Two-photon optogenetic toolbox for fast inhibition, excitation and bistable modulation. Nature Methods 9, 1171-1179.

[130] Riabinina, O., Luginbuhl, D., Marr, E., Liu, S., Wu, M.N., Luo, L., and Potter, C.J. (2015). Improced and expanded Q-system reagents for genetic manipulations. Nature Methods 12, 219-222.

[131] Rickgauer, J.P., and Tank, D.W. (2009). Two-photon excitation of channelrhodopsin-2 at saturation. Proc. Natl. Acad. Sci. USA 106, 15025-15030.

[132] Ritter, E., Piwowarski, P., Hegemann, P., and Bartl, F.J. (2013). Light-dark adaptation of channelrhodopsin C128T mutant. Journal of Biological Chemistry 288, 10451-10458.

[133] Sacconi, L., Dombeck, D.A., and Webb, W.W. (2006). Overcoming photodamage in second-harmonic generation microscopy: real-time optical recording of neuronal action potentials. Proc. Natl. Acad. Sci. USA 103, 3124-3129.

[134] Smetters, D., Majewska, A., and Yuste, R. (1999). Detecting action potentials in neuronal populations with calcium imaging. Methods 18, 215-221.

[135] Spence, D.E., Kean, P.N., and Sibbett, W. (1991). 60-fsec pulse generation from a self-mode-locked Ti-sapphire laser. Optics Letters 16, 42-44.

[136] Stehfest, K., Ritter, E., Berndt, A., Bartl, F., and Hegemann, P. (2010). The branched photocycle of the slow-cycling channelrhodopsin-2 mutant C128T. Journal of Molecular Biology 398, 690-702.

[137] Stocker, R.F., Lienhard, M.C., Borst, A., and Fischbach, K.F. (1990). Neuronal architecture of the antennal lobe in *Drosophila melanogaster*. Cell and Tissue Research 262, 9-34.

[138] Sun, X.R., Badura, A., Pacheco, D.A., Lynch, L.A., Schneider, E.R., Taylor, M.P., Hogue, I.B., Enquist, L.W., Murthy, M., and Wang, S.S. (2013). Fast GCaMPs for improved tracking of neuronal activity. Nature Communications 4, 2170.

[139] Svoboda, K., and Yasuda, R. (2006). Principles of two-photon excitation microscopy and its applications to neuroscience. Neuron 50, 823-839.

[140] Sweeney, L.B., Couto, A., Chou, Y.-H., Berdnik, D., Dickson, B.J., Luo, L., and Komiyama, T. (2007). Temporal target restriction of olfactory receptor neurons by Semaphoring-1a/PlexinA-mediated axon-axon interactions. Neuron 53, 185-200.

[141] Tanaka, N.K., Awasaki, T., Shimada, T., and Ito, K. (2004). Integration of chemosensory pathways in the *Drosophila* second-order olfactory centers. Current Biology 14, 449-457.

[142] Tanaka, N.K., Endo, K., and Ito, K. (2012). Organization of antennal lobe-associated neurons in adult *Drosophila melanogaster* brain. Journal of Comparative Neurology 520, 4067-4130.

[143] Tanaka, N.K., Tanimoto, H., and Ito, K. (2008). Neuronal assemblies of the *Drosophila* mushroom body. Journal of Comparative Neurology 508, 711-755.

[144] Tasic, B., Menon, V., Nguyen, T.N., Kim, T.K., Jarsky, T., Yao, Z., Levi, B., Gray, L.T., Sorensen, S.A., Dolbeare, T., Bertagnolli, D., Goldy, J., Shapovalova, N., Parry, S., Lee, C., Smith, K., Bernard, A., Madisen, L., Sunkin, S.M., Hawrylycz, M., Koch, C., and Zeng, H. (2016). Adult mouse cortical cell taxonomy revealed by single cell transcriptomics. Nature Neuroscience 19, 335-346.

[145] Thorpe, H.M., Wilson, S.E., and Smith, M.C. (2000). Control of directionality in the site-specific recombination system of the streptomyces phage ϕC31. Molecular Microbiology 38, 232-241.

[146] Trannoy, S., Redt-Clouet, C., Dura, J.M., and Preat, T. (2011). Parallel processing of appetitive short- and long-term memories in *Drosophila*. Current Biology 21, 1647-1653.

[147] Tully, T., Preat, T., Boynton, S.C., and Del Vecchio, M. (1994). Genetic dissection of consolidated memory in *Drosophila*. Cell 79, 35-47.

[148] Turner, G.C., Bazhenov, M., and Laurent, G. (2008). Olfactory representations by *Drosophila* mushroom body neurons. Journal of Neurophysiology 99, 734-746.

[149] von Philipsborn, A.C., Liu, T., Yu, J.Y., Masser, C., Bidaye, S.S., and Dickson, B.J. (2011). Neuronal control of *Drosophila* courtship song. Neuron 69, 509-522.

[150] Wang, Y., Mamiya, A., Chiang, A.S., and Zhong, Y. (2008). Imaging of an early memory trace in the *Drosophila* mushroom body. Journal of Neuroscience 28, 4368-4376.

[151] Wang, K., Liu, Y., Li, Y., Guo, Y., Song, P., Zhang, X., Zeng, X., and Wang, Z. (2011). Precise spatiotemporal control of optogenetic activation using an acousto-optic device. PLoS ONE 6(12): e28468.

[152] Wieboldt, R., Ramesh, D., Carpenter, B.K., and Hess, G.P. (1994). Synthesis and photochemistry of photolabile derivatives of gamma-aminobutyric acid for chemical kinetic investigations of the gamma-aminobutyric acid receptor in the millisecond time region. Biochemistry 33, 1526-1533.

[153] Wilson, R.I., and Laurent, G. (2005). Role of GABAergic inhibition in shaping odor-evoked spatiotemporal patterns in the *Drosophila* antennal lobe. Journal of Neuroscience 25, 9069-9079.

[154] Wu, C.L., Shih, M.F., Lai, J.S., Yang, H.T., Turner, G.C., Chen, L., and Chiang, A.S. (2011). Heterotypic gap junctions between two neurons in the *Drosophila* brain are critical for memory. Current Biology 21, 848-854.

[155] Wu, C.L., Shih, M.F., Lee, P.T., and Chiang, A.S. (2013). An octopamine-mushroom body circuit modulates the formation of anesthesia-resistant memory in *Drosophila*. Current Biology 23, 2346-2354.

[156] Xie, Z., Huang, C., Ci, B., Wang, L., and Zhong, Y. (2013). Requirement of the combination of mushroom body γ lobe and α/β lobes for the retrieval of both aversive and appetitive early memories in *Drosophila*. Learning and Memory 20, 474-481.

[157] Yamagata, N., Ichinose, T., Aso, Y., Plaçais, P.Y., Friedrich, A.B., Sima, R.J., Preat, T., Rubin, G.M., and Tanimoto, H. (2015). Distinct dopamine neurons mediate reward signals for short- and long-term memories. Proc. Natl. Acad. Sci. USA 112, 578-583.

[158] Yang, H.H., St-Pierre, F., Sun, X., Ding, X., Lin, M.Z., and Clandinin, T.R. (2016). Subcellular imaging of voltage and calcium signals reveals neural processing *in vivo*. Cell 166, 245-257.

[159] Yasuyama, K., Meinertzhagen, I.A., and Schurmann, F.W. (2002). Synaptic organization of the mushroom body calyx in *Drosophila melanogaster*. Journal of Comparative Neurology 445, 211-226.

[160] Yizhar, O., Fenno, L.E., Prigge, M., Schneider, F., Davidson, T.J., O'Shea, D.J., Sohal, V.S., Goshen, I., Finkelstein, J., Paz, J.T., Stehfest, K., Fudim, R., Ramakrishnan, C., Hugurnard, J.R., Hegemann, P., and Deisseroth, K. (2011). Neocortical excitation/inhibition balance in information processing and social dysfunction. Nature 477, 171-178.

[161] Yu, D., Akalal, D.B., and Davis, R.L. (2006). *Drosophila* α/β mushroom body neurons form a branch-specific, long-term cellular memory trace after spaced olfactory conditioning. Neuron 52, 845-855.

[162] Yuste, R., and Denk, W. (1995). Dendritic spines as basic functional units of neuronal integration. Nature 375, 682-684.

[163] Zemelman, B.V., Nesnas, N., Lee, G.A., and Miesenböck, G. (2003). Photochemical gating of heterologous ion channels: remote control over genetically designated populations of neurons. Proc. Natl. Acad. Sci. USA 100, 1352-1357.

[164] Zhang, F., Wang, L.P., Brauner, M., Liewald, J.F., Kay, K., Watzke, N., Wood, P.G., Bamberg, E., Nagel, G., Gottschalk, A., and Deisseroth, K. (2007). Multimodal fast optical interrogation of neural circuitry. Nature 446, 633-639.

[165] Zhang, F., Prigge, M., Beyriere, F., Tsunoda, S.P., Mattis, J., Yizhar, O., Hegemann, P., and Deisseroth, K. (2008). Red-shifted optogenetic excitation: a tool for fast neural control derived from *Volvox carteri*. Nature Neuroscience 11, 631-633.

[166] Zhu, P., Narita, Y., Bundschuh, S.T., Fajardo, O., Scharer, Y.P., Chattopadhyaya, B., Bouldoires, E.A., Stepien, A.E., Deisseroth, K., Arber, S., Sprengel, R., Rijli, F.M., and Friedrich, R.W. (2009). Optogenetic dissection of neuronal circuits in zebrafish using viral gene transfer and the Tet system. Frontiers in Neural Circuits 3, 21.

Acknowledgments

First of all, I would like to acknowledge Hokto Kazama for his invaluable advice, constant encouragement, and academic guidance in this fascinating area of science. Indeed, during this project, we faced a lot of difficulties. All of those, however, could be defeated through the discussion with him or sometimes by conducting experiments together to the midnight. Therefore, he is my supervisor, but also, to me, a great comrade. Hokto is also an active experimenter. As an experimental neuroscientist, I thank him for provision of custom-made plate for imaging, support in denoising, and instruction of whole-cell recording from PNs.

I would like to thank Kazuo Okanoya for his kind support, guidance and for being the main thesis examiner. The University of Tokyo Komaba-RIKEN joint graduate program could not have been functional without his leadership. I also acknowledge to the referees of this dissertation: Isamu Motoyoshi, Thomas J. McHugh, and Takashi Tsuboi.

I thank all the past and the present members of the RIKEN Kazama lab: Laurent Badel for Matlab codes for olfactometer and provision of practical French lessons; Keita Endo for sharing his knowledge of morphological studies and kind advice as a senior researcher; Damien Mercier for suggestions concerning data analyses and invaluable French lessons; Hiroshi M. Shiozaki for critical comments on the logic of the project and early instructions of in vivo calcium imaging; Yoshiko Tsuchimoto for generation of transgenic fly lines as a co-author of the paper we published and early guidance of Leica SP2; Hongping Wei for valuable discussion about ribbon synapses; Kazumi Ohta and Naomi Shimada for excellent technical supports; Kayoko Kihara and Mie Akutsu for supports as a lab assistant.

This project could be progressed thanks to the advices from professional researchers all over the world: the author thanks Rainer W. Friedrich, Edward S. Boyden, Hajime Hirase, David E. Featherstone, Vivek Jayaraman, Yoshinori Aso, Toshihide Hige and Akinao Nose. Also, the project was supported by the reagents, devices, and fly strains kindly provided by following people and organization: I thank Bloomington Stock Center, Vienna Drosophila Resource Center (VDRC), Adrian W. Moore, Zuoren Wang, Ann-Shyn Chiang, Liqun Luo, Dan Tracey and Gero Miesenböck for fly strains, and Edward S Boyden for plasmid. Spin coating was instructed by Norihiko Hayazawa, and the spin coater was provided by Nanoscience Joint Laboratory (RIKEN). AFN was provided by BSI Research Resources Center (RIKEN), and the FV1000-D by BSI-Olympus Collaboration Center (BOCC, RIKEN). I appreciate the technical supports of Leica Microsystems and Spectra-Physics: I thank Tomoyuki Ichikawa, Yoshinori Murata, Daisuke Hirotaki, Takeshi Chiaki, Rie Hayashi, Yasuo Goto and Tadamoto Shigeno.

The author was financially supported by the following fellowships: Junior Research Associate (JRA) from RIKEN and Research Fellowship for Young Scientists from Japan Society for the Promotion of Science (JSPS).

I was once in the industry as a research fellow, and out. It was not an easy decision to make. But the members of Division of Cloud Computing, Central Research Laboratories, NEC.com encour-

aged me with warm words.

Finally, I express my deep acknowledgments to my parents, Tomoki and Miyoko, and my elder sisters, Maki and Risa. Words fail to express my appreciation. So, I put no words here.

The author declares that he did his best at any time in the graduate school.